Integrated Quantum Photonics

ALBERTO POLITI

Department of Electrical and Electronic Engineering

A thesis submitted to the University of Bristol in accordance with the requirements for the degree of Doctor of Philosophy in the Faculty of Engineering, Department of Electrical and Electronic Engineering.

January 2010

Abstract

Until recently, quantum photonic architecture comprised of large-scale (bulk) optical elements, leading to severe limitations in miniaturization, scalability and stability. The development of the first integrated quantum optical circuitry removes this bottleneck and allows realization of quantum optical schemes whose greatly increased capacity for circuit complexity is crucial to the progress of experimental quantum information science and the development of practical quantum technologies.

Integrated quantum photonic circuits within Silica-on-Silicon waveguide chips were simulated, designed and tested. Hundreds of devices have been fabricated with the core components found to be robust and highly repeatable. Amongst these demonstrations, all the basic components required for quantum information applications are shown. The first integrated quantum metrology experiments are demonstrated by beating the standard quantum limit with two- and four-photon entangled states while providing the first re-configurable integrated quantum circuit capable of adaptively controlling levels of non-classical interference of photons. The tested integrated devices show no limitations to obtain high quality performances. It is reported near-unity visibility of two-photon non-classical interference and a Controlled-NOT gate that could in principle work in the fault tolerant regime.

It is demonstrated the realization of a compiled version of Shors quantum factoring algorithm on an integrated waveguide chip. This demonstration serves as an illustration to the importance of using integrated optics for quantum optical experiments.

Abstract

The first integrated optical circuits fabricated in the laser direct-write technology are reported in this Thesis. The quality quantum effects, together with a rapid turnaround process and the capability of writing complex 3D structures are promising for future quantum optical networks.

The advent of integrated quantum photonics is necessary for the progression of quantum information science. The results reported in this Thesis provides fundamental building blocks from which future quantum devices will be constructed and presents high-fidelity quantum optics platforms for fundamental investigation.

The advantage of the emotions is that they lead us astray,

and the advantage of science is that it is not emotional.

- Oscar Wilde

Acknowledgements

During the last three years in Bristol I worked and spent time with people that made this period a great fun. First of all I want to thank my supervisors, Prof. Jeremy O'Brien and Prof. John Rarity. I am indebted with Jeremy first of all for the opportunity to come in this group and start a PhD in quantum information. In the past years he was a great supervisor, since he gave me the freedom to develop new ideas, encouraging me when problems seemed to block my path. His support to present our research at international conferences increased the understanding of our research field and gave me the precious opportunity to meet scientist from different part of the world.

I want to thank John for creating such a wonderful group, his mentality in managing the students and researchers has a important impact on the work that everyone can produce. Moreover, his deep understanding in the fundamentals of quantum optics has been essential to overcome the obstacle in these years.

I am particularly indebted with Prof. Akira Furusawa and his group for the great opportunity to spend two months in Tokyo as a research visitor. The wonderful chats at lunch-time with him gave me a deep insight into continuous variables and let me feel welcome in the group.

I had the luck to spend time with wonderful people, especially when I first arrived in UK and my English was still quite poor. I want to thank all the CQP group, and in particular the A-Team (Alex, Andrew, Anthony) for the help in the first year. They had to stand me when the simulations were not working and I wanted to throw the computer out of the window. I want to thank all the members of the Photonic group, Dr. Martin Cryan and Dr. Siyuan Yu in particular, for the

help to overcome the problems with the simulations, so they saved my computer. After moving in Physics building I have spent time with other guys from the group: Xiao-Qi, Alberto, Kal, Damien, Mark, Maria, Mirko and JP. It was a pleasure to shearing office and ideas.

In the last two years I was lucky to work closely with a very bright PhD student and a good friend, Jonathan Matthews, who joined the group one year after me. It was a pleasure to spend time in the lab and confronting our ideas. The outcomes from our talks have been fundamental in increasing the understanding of what we are doing.

I am grateful to my parents, Valentina and Lorenzo who supported me from the day I said I wanted to start a PhD outside Italy. Every time I come back and meet you, Silvia's family, the guys in Stradella and Pavia is hard to leave again. Finally, I want to thank Silvia, who followed me in this adventure and stayed with me all this time. Thanks for your support!

Authors' Declaration

I declare that the work in this dissertation was carried out in accordance with the requirements of the University's Regulations and Code of Practice for Research Degree Programmes and that it has not been submitted for any other academic award. Except where indicated by specific reference in the text, the work is the candidate's own work. Work done in collaboration with, or with the assistance of, others, is indicated as such. Any views expressed in the dissertation are those of the author.

SIGNED: .....

DATE: .....

Publications

1. A. Peruzzo, A. Laing, A. Politi, T. Rudolph, J.L. OBrien, Multimode quantum interference of photons in multiport integrated devices, *in preparation.*

2. R. Ukai, N. Iwata, Y. Shimokawa, S.C. Armstrong, A. Politi, J. Yoshikawa, P. van Loock, A. Furusawa, Demonstration of unconditional one-way quantum computations for continuous variables, *arXiv:1001.4860v1.*

3. A. Laing, A. Peruzzo, A. Politi, M.R. Rodas, M. Halder, M.G. Thompson, J.L. OBrien, Towards fault tolerant quantum photonics circuits, *Submitted.*

4. A. Politi, J.C.F. Matthews, M.G. Thompson, J.L. O'Brien, *IEEE Journal of Selected Topics in Quantum Electronics*, **15**, 6, 1673-1684, (2009).

5. A. Politi, J.C.F. Matthews, J.L. O'Brien, Shor's Quantum Factoring Algorithm on a Photonic Chip, *Science*, **325**, 1221 (2009).

6. G.D. Marshall, A. Politi, J.C.F. Matthews, P. Dekker, M. Ams, M.J. Withford, J.L. O'Brien, Laser written waveguide photonic quantum circuits, *Optics Express*, **17**, 15, 12546-12554, (2009).

7. J.C.F. Matthews, A. Politi, A. Stefanov, J.L. O'Brien, Manipulation of multiphoton entanglement in waveguide quantum circuits, *Nature Photonics*, **3**, 346 - 350 (2009).

8. A. Politi and J.L. O'Brien, Quantum computation with photons, *Nanotechnology Perceptions*, 4, 3 (2008).

9. A. Politi , M.J. Cryan, J.G. Rarity, S. Yu, and J.L. O'Brien, Silica-on-Silicon Waveguide Quantum Circuits, *Science* **320**, 646 (2008).

Conference talks presented

In addition to the following personal presentations, co-author of more than 30 talks at international conferences including invited and post-deadline talks.

1. A. Politi, J.C.F. Matthews, A. Laing, A. Peruzzo, P. Kalasuwan, M. Zhang, X.-Q. Zhou, M. Rodas, M.J. Cryan, J.G. Rarity, A. Stefanov, S. Yu, M.G. Thompson, and J.L. OBrien; Integrated Quantum information science with photons, ICQFT'09, Shanghai, July 17 - 22 , 2009 (Invited)

2. A. Politi and J.L. O'Brien, Quantum information science with photons on a chip, 11th ICSSUR and 4th Feynman Festival, Olomouc, June 22-26, 2009 (Invited)

3. A. Politi, J.C.F. Matthews, A. Laing, A. Peruzzo, P. Kalasuwan, M. Zhang, X.-Q. Zhou, G.D. Marshall, P. Dekker, M. Ams, M. Withford, M. Rodas, M.J. Cryan, J.G. Rarity, A. Stefanov, S. Yu, M.G. Thompson, and J.L. OBrien; Integrated Quantum information science with photons, CLEO - EuropeEQEC 2009, Munich, June 14 - 19 , 2009

4. A. Politi, J.C.F. Matthews, A. Laing, A.S. Clark, J. Fulconis, G.D. Marshall, P. Dekker, M. Ams, M. Withford, W.J. Wadsworthy, T. Rudolph, M.J. Cryan, J.G. Rarity, A. Stefanov, S. Yu, J.L. O'Brien, Quantum information science with photons on a chip, Quantum Optics IV, Florianopolis, October 13-17, 2008 (Invited)

5. A. Politi, M. Cryan, J. Rarity, J.L. O'Brien, Silica-on-Silicon waveguide quantum circuits, Photon08, Edinburgh August 26-29, 2008

6. A. Politi, M. Cryan, J. Rarity, J.L. O'Brien, Quantum Information Science with Photons on a chip, International Laser Physics Workshop, Trondheim, June 30 - July 4, 2008 (Invited)

Contents

List of Figures

LIST OF FIGURES

LIST OF FIGURES

List of Tables

Chapter 1

Introduction

The work described in this Thesis is composed by the merging of two important fields of research, Quantum information and Photonics. Both of these fields are, or promise to be, fundamental for the development of new technologies for a range of different applications, including the transmission and manipulation of information.

1.1 Photonics

Photonics is the technology of generating and harnessing light. The range of applications of photonics extends from energy generation to detection to communications and information processing. The field of photonics had a huge growth in the 1970s, when fibre-optic communication systems have been developed. The use of fibre optics revolutionized the telecommunications industry and is at the basis of the Information Age. The request of fastest and more powerful communication systems drove the improvement of complex opto-electronic devices in integrated circuits. The growth of capabilities of photonic circuits will ultimately lead to the use of all-optical devices for a broad range of applications.

Nowadays, even if the transmission of information over long distances is obtained using photonic networks, the manipulation and transport of data over short distances in computers is conducted using micro-electronic devices. As predicted by Moore's law [4], the number of transistors, and capabilities, that can be placed

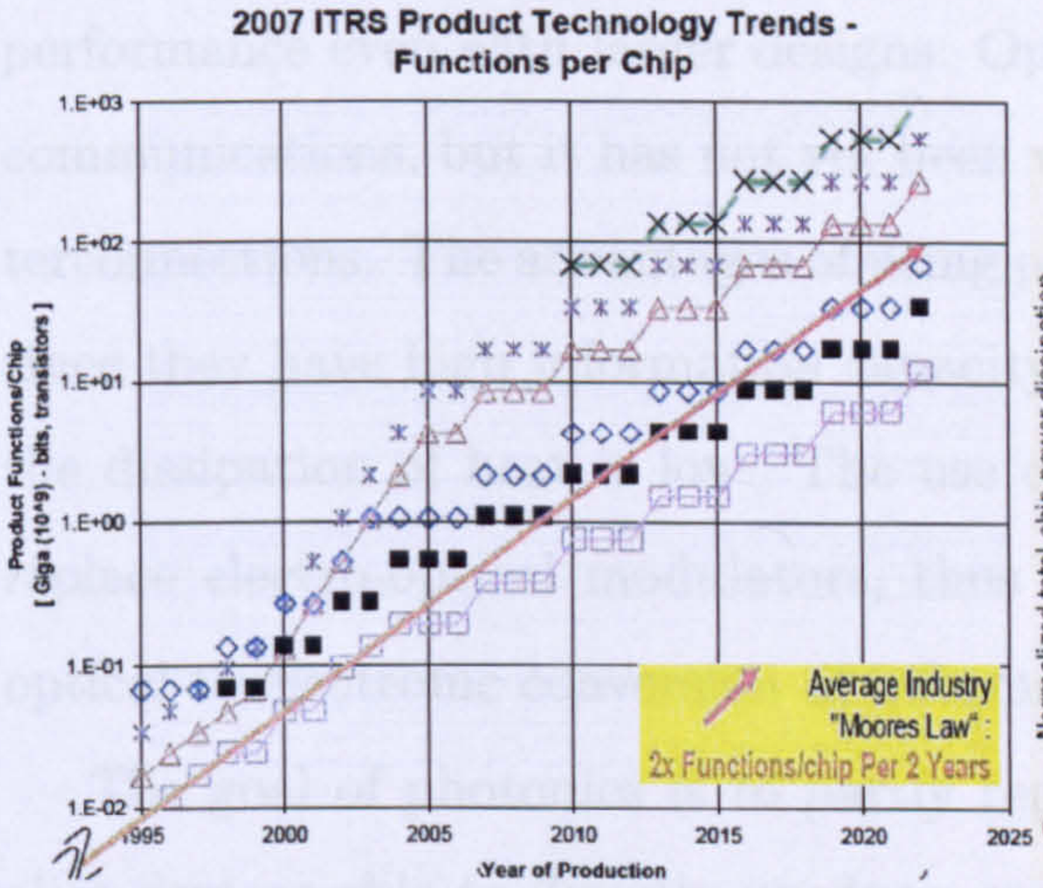

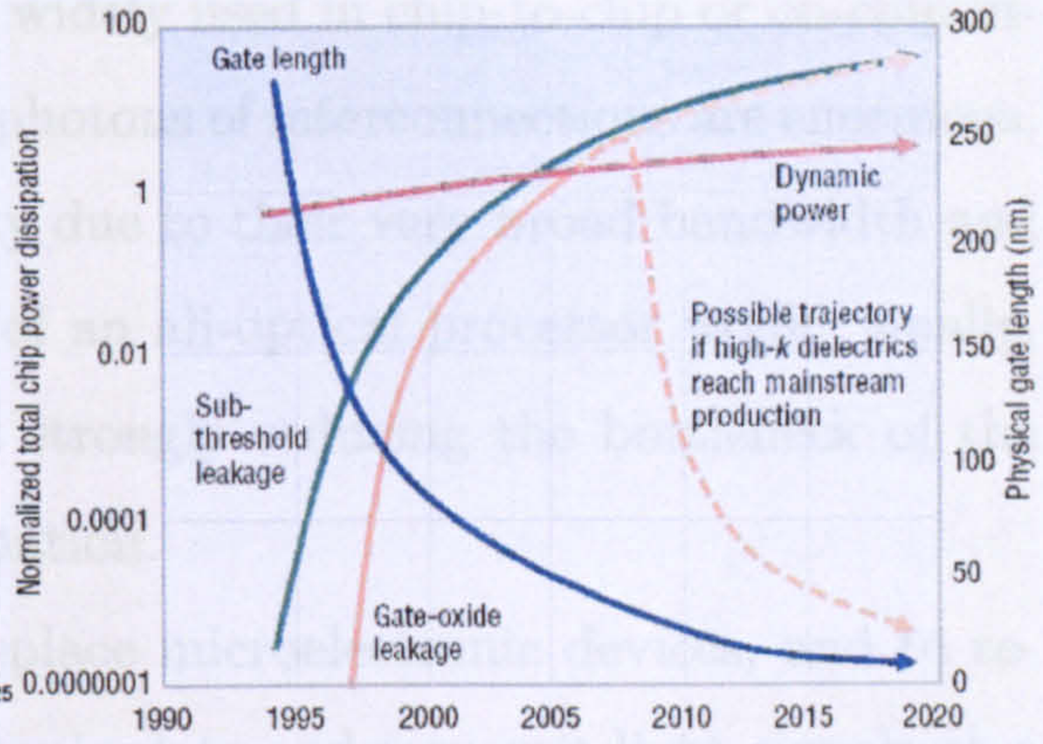

Figure 1.1: Moore's law. On the left, ITRS Product Function Size Trends [1]. On the right: Total chip dynamic and static power dissipation in integrated chips [2].

inexpensively on an integrated circuit has doubled approximately every two years (see the left graph in figure 1.1 for last years trend [1]). The improved performance of computer systems has been achieved, in large part, by miniaturizing the minimum feature size of the components in the integrated chips. This allows transistors to operate at a higher frequency, performing computations with a higher speed. However, the result in tighter packing of the wires on a microprocessor is the increase parasitic capacitance and signal propagation delay. Consequently, the delay due to the communication between the parts of a chip becomes comparable to the computation delay itself. Also, the complexity of the components and the length of the connections increase the power consumption of integrated chips (see the right hand graph of figure 1.1). Leakage currents are now one of the major technical problems facing the semiconductor industry [2]. This phenomenon, known as the "interconnect bottleneck", is becoming a major problem in high-performance computer systems.

Optical interconnects are considered a primary option to solve this problem of interconnect bottleneck, replacing the long metallic interconnects. The use of photons to transport information in different parts of the chips promises better

performance even with larger designs. Optics has widespread use in long-distance communications, but it has not yet been widely used in chip-to-chip or on-chip interconnections. The advantages of using photons of interconnections are enormous, since they have high information capacity due to their very broad bandwidth and the dissipation of heat is low. The use of an all-optical processor would, finally, replace electro-optical modulators, thus strongly reducing the bottleneck of the optical to electronic conversion of information.

The goal of photonics is to partly replace microelectronic devices, and to realize devices able to directly produce, manipulate and transmit light signals at a microscopic integration level.

1.2 Quantum Information Science

Growth in both information processing and transmission capacity in computers will ultimately come to a stop. In the case of current computers based on electrons, it is foreseen that the continued miniaturization of the components will reach a fundamental limit. The dimensions of the components will be so small that the quantum effects, as quantum tunneling between different parts of the device, can not be ignored. At the same time, the power of the signals in the interconnections is been decreased, both when using electrons or photons, to reduce delays and power dissipations. This will cause the power of the signals to decrease so much to reach the fundamental level of a single quanta of energy to be used - a single photon for light, a single electron for the current. At this level, quantum effects, as superposition and entanglement, will change the behavior of the integrated devices from the usual classical description.

It is then interesting to ask if it is possible to take advantage of intrinsic quantum mechanical effects to perform tasks in a better way than the classical counterparts. Quantum information science has emerged over the last two decades to consider whether this behavior could be useful. It addresses the question: What additional power or functionality can be achieved in encoding, transmit-

ting and processing information by using uniquely quantum mechanical behavior? Anticipated technologies include quantum key distribution, which offers perfectly secure communication; quantum metrology, which allows more precise measurements than could ever be achieved without quantum mechanics; and quantum lithography, which could enable fabrication of devices with features much smaller than the wavelength of light. Perhaps the most profound future technology is a quantum computer that promises exponentially faster operations for particular tasks.

Single particles of light are an excellent choice for quantum technologies because they are relatively noise free; information can be moved around quickly; and manipulating single photons is easy. For these reasons, photons have been widely used in quantum communication, quantum metrology, and quantum lithography settings, as well as quantum bits (or qubits) for quantum information processing.

1.3 Waveguides for Quantum Information

All the important implementations of experimental quantum information science with photons have primarily consisted of large-scale (bulk) optical elements confined to optical laboratories, making such schemes physically un-scalable, sensitive to stability and impractical for applications outside of the research lab. In addition, many have required the design of sophisticated interferometers to achieve the sub-wavelength stability required for reliable operation. Continuing mainstream activities are developing large scale quantum systems that are becoming too large and unstable to be realistically implemented under these experimental constraints.

The development of integrated circuits for quantum optics experiments will allow greater complexity and superior performance thanks to the monolithic structure of the samples. In a long term, the use of micro-photonic architectures will allow quantum optics to be moved out of the scientific labs to develop new and more powerful technologies.

1.4 Summary of the Thesis

This Thesis describes the devices and experiments conducted at the University of Bristol by me and my colleagues to develop integrated quantum photonic architectures. In Chapter 2, I introduce the fundamental notions and theories that compose the starting point for this Thesis. In particular, I describe the unique properties that are required to perform quantum information experiments with photons. I also introduce the properties of integrated optical devices, setting the notation for light propagation in waveguide structures.

Chapter 3 describes the simulation works performed to design all the integrated components measured in the rest of the Thesis. The Chapter is a summary of the notions learned and the results obtained in the first year of my PhD. The guiding properties of silica-on-silicon waveguides are studied, keeping in mind the fabrication capabilities of the Centre for Integrated Photonics (CIP), where the waveguides have been produced. All the components required to build arbitrary optical networks for quantum optic purposes are studied and designed.

Chapter 4 is based on the experimental results obtained in the analysis of the fundamental block for quantum optic networks – the integrated coupler. After introducing the non-classical interference effect between photons at a beam-splitter, the results obtained for silica-on-silicon directional couplers are presented. A section is dedicated to describe recent experimental results that prove the quality of the fabricated samples. These results represent a key step for integrated quantum optics because they prove there is no fundamental limitation in the performances of quantum effects in waveguide structures. The last section of the Chapter is dedicated to the analysis of the results obtained with a different type of integrated coupler, based on multi-mode interference (MMI).

Chapter 5 is a standalone section of the Thesis, since it contains the results obtained from samples fabricated with a different technology respect to the silica-on-silicon one. The Chapter contains the results obtained with samples fabricated with the laser direct-write technology. The samples have been designed and fab-

ricated by the group of M. J. Withford at MacQuarie University. Given that the direct-write technology to produce waveguides is quite recent, the fabrication process and the properties of the waveguides are briefly described. I then present the experimental results obtained with directional couplers fabricated in glass. These works show high performance quantum properties of the samples with both two and three photons.

In Chapter 6, I describe the experimental details of the demonstrations of reconfigurable quantum circuits for quantum photonics. The first section is dedicated to the realization of single qubit operations using integrated optics. The properties of resistive heaters to control the optical phase of single photons are studied. The use of resistive heaters to control entangled states of two and four photons is described, paying attention to the applications of such states for quantum metrology. In the last section of the Chapter I describe the implementation of reconfigurable integrated circuits for quantum optics.

Chapter 7 is dedicated to the experimental study of the integrated two-qubit gates. I introduce the scheme used to implement controlled-NOT quantum operations using photons. The analysis of the experimental results obtained from different gates is reported. I also introduce a method to prove the coherent operation and the presence of entanglement in integrated circuits. This result is fundamental given the difficulties of performing full process tomography on integrated gates. The last section is dedicated to the study of the samples regarding fault tolerant operation in quantum computation. The presented results suggests that integrated photonics CNOT gates are capable of achieving low levels of errors, within the range required to perform quantum computation.

In Chapter 8, I describe how, combining the elements described in the previous Chapters, it is possible to perform simple quantum algorithms in a photonic chip. In particular, the implementation of Shor's quantum algorithm to factorize in prime numbers is presented. After an introduction about the problem of factorization and about Shor's algorithm, I present the scheme used to implement a compiled version of the quantum algorithm to factorize the number 15. This sim-

ple proof of principle demonstration shows the capabilities of an integrated optic approach to quantum information.

Chapter 9 contains the final remarks and conclusions of the Thesis. One section is also dedicated to the analysis of future works that will be follow the results obtained during my PhD. Finally, I try to give a general overview of the possibilities that the application of photonic technologies can open for quantum information demonstrations.

Chapter 2

Background

In this Chapter I will introduce all the concepts and methods used throughout the rest of the Thesis. I will set up the formalism used for the aspects regarding quantum information and metrology in the first part of the chapter. In the remaining I will concentrate on the formalism used to describe and study the properties of integrated waveguides at optical frequencies. This section is the starting point for all the simulations performed to design the integrated circuits for quantum purposes described in Chapter 3.

2.1 Quantum Information Science

Continued growth of the global economy relies on an increasing capacity to process and communicate information. Integrated circuits based on classical physics have delivered continual speed-up in information processing over the past half century. It is through gradual miniaturisation that this technology has brought constant increases in performance. This miniaturisation has reached so far that it is now possible to count the number of atoms across the smallest feature of a semiconductor transistor. At this scale, quantum mechanical effects are beginning to perturb the operation of the transistor, and thus the demand for higher performance is approaching the limits of classical physics. It is therefore natural to reverse the problem and ask what happens if we use the laws of quantum mechanics to encode

process and transmit information. Quantum information science (QIS) is widely regarded as the most promising pathway towards disruptive information and communication technologies; it aims to harness quantum mechanical effects to develop quantum systems that will deliver significant improvements in information processing and security [5]. QIS has also provided insights into the fundamental physical workings of nature, and continues to asks fundamental questions about the control of coupled quantum systems the precursors to engineered complex quantum systems and simulators.

Perhaps one of the most enthralling applications of quantum physics is the construction of a quantum computer. Theoretical work predicts a quantum computer will be able to perform certain tasks with an unprecedented efficiency. For example, Shor's algorithm promise to factorize the product of two prime numbers exponentially faster than a classical computer [6]–a task previously thought to take an exponential number of resources for solution, and hence the basis for current classical cryptography protocols. Other problems have already expected to obtain better solution on quantum computers and extensive research is being carried out to increase the capacity of quantum information.

The underlying element on which QIS is based is the qubit: the basic element of quantum information encoded on any two level quantum system. Consider for example two energy levels of an atomic system labeled by either "0" or "1". Classical information theory considers levels equivalent to classical "bits" whose logical state are either 0 or 1. If, however, we encode a qubit onto this system by using the atomic system, then the state of the qubit could exist in either of the quantum states $|0\rangle$ or $|1\rangle$, as with the classical model, or more generally in some complex linear combination of both channels given by

$$|\psi\rangle = \cos\theta\,|0\rangle + e^{i\phi}\sin\theta\,|1\rangle\,. \tag{2.1}$$

The other key property that differentiates classical bits form quantum qubits is that the latter can be in a so called "entangled state". Quantum entanglement of two particles means that the state of either of the particles is not defined, but

only their collective state. In a more mathematical language, consider a bipartite system ($H = H^A \otimes H^B$). A pure state is separable if it can be written as a tensor product of the sub-system states, $|\psi_{sep}\rangle = |\psi^A\rangle \otimes |\psi^B\rangle$. A quantum system is entangled if it is inseparable, and does not satisfy the above relation.

The simplest examples of entangled states are the maximally entangled Bell states for two qubits - the smallest system capable of exhibiting entanglement:

$$|\Phi^{\pm}\rangle = \frac{1}{\sqrt{2}}(|00\rangle \pm |11\rangle), \tag{2.2}$$

$$|\Psi^{\pm}\rangle = \frac{1}{\sqrt{2}}(|01\rangle \pm |10\rangle). \tag{2.3}$$

Entanglement is one of the most distinctive features of quantum mechanics, Schrödinger thought this property dictates the departure of quantum mechanics from the classical descriptions, and even nowadays it is though that the power of quantum computers is somehow linked to entanglement.

The obvious big question is how to encode and perform quantum computation, and which is the best system to use for this task. This is still an open question, but a set of criteria to identify the suitable systems has been found. This set has been coded in the form of five points, called the "DiVincenzo criteria" [7]. They are stated in the following list.

1. Scalable physical system to encode qubits. A system with well known quantum states is required. In principle it is not needed that the number of states is equal to two (to form a qubit), but the ability to confine the number of states to a defined value is necessary. For example it is possible to encode quantum information on ions with a set of energy states, if it is possible to restrict the number of states of interest to the required value (for example two levels to form a qubit).

2. Ability to initialize the system of qubits. Given the system of n qubits, it is required that an initial fiducial state can be produced. The initial state can be composed by all qubits in the state $|0\rangle$, for example, in an atomic system, the initial state can be given by all the atoms in the ground state.

3. Low decoherence. The coupling between the qubits and the environment (i.e. to all the rest of the Hilbert space of the world) should be sufficiently weak that quantum operations of the qubits is not affected. This means that the timescale for an error caused by the environment has to be small compared to the effective timescale of the quantum computation. This simply means that the probability for noise to produce errors has to be sufficiently small. Error correction schemes for quantum computation already exist to reduce the problems of decoherence, and current research is expected to improve even more the levels for fault-tolerant quantum computation.

4. Universal set of gates. This point constitutes the obvious requirement that computation has to be possible on quantum systems. The computation is realized through a number of quantum gates. The set of quantum gates needed has to be big enough to be universal, so that any unitary quantum transformation can be decomposed as a sequence of gates of the set. Usually discrete one- and two-qubit operations are sufficient to compose a universal set, but more complicated gates can be used to reduce complexity. The quantum operations that compose the gates have to observe requirements on precision. In fact, imprecision of unitary operations is a form of decoherence, and has a similar effect on the fault-tolerant level.

5. Qubit-readout and quantum measurements. It is necessary to be able to readout the state of the set of qubits used for the quantum computation, to obtain the classical results. This corresponds to a usual string of bits, since the measurement returns a set of classical results. The measurement can be a projective measurement [5], or a generalized measurement allowed by quantum mechanics. It is important to note that the measurement can be performed individually on each qubit. For certain schemes, readout of a partial set of qubits has to be performed during the quantum computation, without disturbing the remaining set of qubits.

These criteria seem quite reasonable, we need qubits and the ability to initialize

the system, perform the computation, have low error probability and read the results. However the physical requirements to achieve these abilities are in contrast with one another. Low errors, or decoherence, means the qubits do not talk much with the environment or between themselves. At the same time, initialization and read-out require that it is possible to obtain some kind of interaction between the qubits and the environment (as classical instruments) to perform the required operation. Also, the capability of performing an universal set of gates means that two- or multi-qubit interaction is necessary, so that qubits must be able to see each other.

It is easy to realize that having all the above physical properties at the same time on a single system is really challenging. To find the most suitable candidate upon which to implement a quantum computer, two different kinds of system can be considered. The first category is composed by those materials in which the interaction of qubits (with other qubits or with classical instruments) is seen as easy and scalable, and research has to focus on obtaining low noise and decoherence. Examples of this kind of system to encode qubits are spins in quantum dots, hyperfine levels in ions, superconducting circuits. The second category of systems to obtain quantum information is composed by materials in which interactions are really weak, so that noise and decoherence is not a problem. However, work has to be done to solve the problem of obtaining controlled operations for measurements and application of quantum gates. The most notable example of this category is photons. The next section is dedicated to the properties of qubits encoded on photons.

2.2 Quantum Information with Photons

Using photons to encode the qubits is seen as one of the most promising ways to achieve quantum information processing [8, 9]. The main advantage of photons, with respect to other candidates, is that they are almost free from noise, or decoherence, at the optical frequencies. It is known even from classical optics that

independent electromagnetic waves (or a collection of photons in the quantum mechanical description) see no interaction between them in the vacuum. Even with the help of other materials, non-linear interactions are small. A useful property of photons is that the interaction with a medium is different depending on the optical properties of the material. In this way some of the properties of the photons can be manipulated using the right material. From the quantum information point of view, it is interesting to note that photons are bosons with spin 1. Also, it is possible to encode qubits using different degree of freedom of the photon. For example, it is possible to use the polarization of photons [10] or arrival time [11], optical mode position, angular momentum [12]. It is interesting to note that, apart from the polarization, the other degrees of freedom are not limited to two levels. In fact, they are not quantized and their spectrum is composed from a continuum of possible values. For this reason it is possible to encode qubits, restricting the number of states under consideration, or extend the dimension of the Hilbert space to an higher value. The restriction to qubits is possible because there is no interaction between the different values that compose the spectrum.

Figure 2.1 shows the scheme for encoding information in the polarization of light. In this case, the $|0\rangle$ state is encoded as a photon with polarization in the Horizontal direction ($|0\rangle = |H\rangle$) and the $|1\rangle$ state with Vertical polarization ($|1\rangle = |V\rangle$). All the other states of the qubit can be obtained as a superposition, with different amplitudes and phases, of these two states. The advantage of the polarization encoding with photons is that it is straightforward to obtain one qubit logic gates. In fact, using waveplates, it is possible to rotate the polarization state of light to any chosen direction. A birefringent wave-plate is made by a crystal that retards one polarization by a fraction of a wavelength λ relative to an orthogonal polarization, causing a rotation of the state on the Poincaré sphere, with the axis of rotation determined by the orientation of the wave plate. For example, using a half waveplate with the optical axis set at 22.5 degrees, it is possible to implement a Hadamard gate H, that brings the state $|H\rangle$ to the state $(|0\rangle + |1\rangle)/\sqrt{2}$. Also, with a combination of a quarter, half, quarter, waveplates it is possible to perform

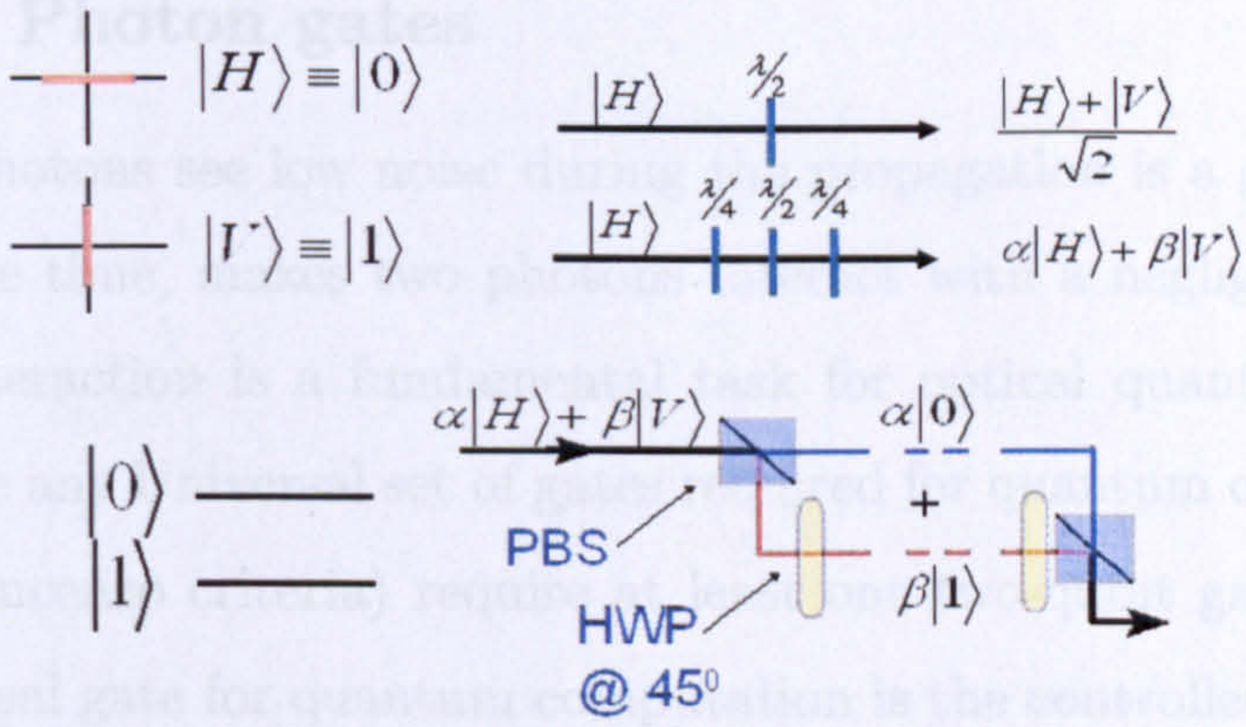

Figure 2.1: A qubit can be encoded in the polarization of a single photon (top) with horizontal polarization state (H) encoding the state $|0\rangle$, and vertical polarization (V) the state $|1\rangle$. Single qubit logic gates, such as the Hadamard, are straightforward since they correspond to polarization rotations of classical light, which can be realized with birefringent waveplates (left). Converting between polarization encoding $a|H\rangle + b|V\rangle$ and spatial encoding $a|0\rangle + b|1\rangle$ (right), where $|0\rangle$ and $|1\rangle$ correspond to a photon in the upper and lower paths, respectively, can be achieved using a polarizing beamsplitter.

an arbitrary rotation gate, that could bring one state to any other state. It is interesting to note that the waveplates, and in general all the one qubit gates with photons, can be characterized using classical light. This is again caused by the fact that photons do not interact much between them, so that the behavior of a component can be tested with one photon alone, or with a collection of photons (as a classical source) without appreciable difference.

Another common way to encode information with photons is to use the path encoding. In this case the presence of the photon in the "0" channel encodes the $|0\rangle$ state, and the presence of the photon in the "1" channel encodes the $|1\rangle$ state. It is possible to change from the polarization to the path encoding just by using a polarizing beam splitter (PBS), an optical element that divides the two orthogonal components of the polarization of light, and a waveplate. The scheme is shown in figure 2.1.

2.2.1 Two Photon gates

The fact that photons see low noise during the propagation is a great advantage, but, at the same time, makes two photons interact with a negligible probability. Two photon interaction is a fundamental task for optical quantum information processing, since any Universal set of gates required for quantum computation (see the fourth DiVincenzo criteria) require at least one two-qubit gate. An example of such a universal gate for quantum computation is the controlled-NOT (CNOT) gate. This is the quantum analogue of the XOR gate, which flips the state of the target qubit only if the control qubit is in the "1" state. In contrast to the XOR, the CNOT can have input and output states that are a quantum mechanical superposition. So the transformation can be described as:

$$a\,|00\rangle + b\,|01\rangle + c\,|10\rangle + d\,|11\rangle \rightarrow a\,|00\rangle + b\,|01\rangle + c\,|11\rangle + d\,|10\rangle \tag{2.4}$$

and the unitary operation can be written as

$$U_{CNOT} = \begin{pmatrix} 1 & 0 & 0 & 0 \\ 0 & 1 & 0 & 0 \\ 0 & 0 & 0 & 1 \\ 0 & 0 & 1 & 0 \end{pmatrix}. \tag{2.5}$$

Figure 2.2 shows why this operation is difficult. The two paths used to encode the target qubit are mixed at a 50% reflecting beam splitter (BS) (or half-silvered mirror), which performs the Hadamard operation in spatial encoding. If the control qubit is in the state "0", the second Hadamard (BS) undoes the first, returning the target qubit to exactly the same state it started in. From the optical point of view the target qubit enters a conventional Mach-Zender interferometer such that the photon goes into a superposition inside the interferometer, but always exits in the same logical state that it entered. If, however, a π phase shift is applied to the interferometer, the target qubit undergoes a bit-flip (or NOT operation). A CNOT must implement this phase shift only if the control photon is in the "1" path. One could imagine doing this with a nonlinear optical material, such

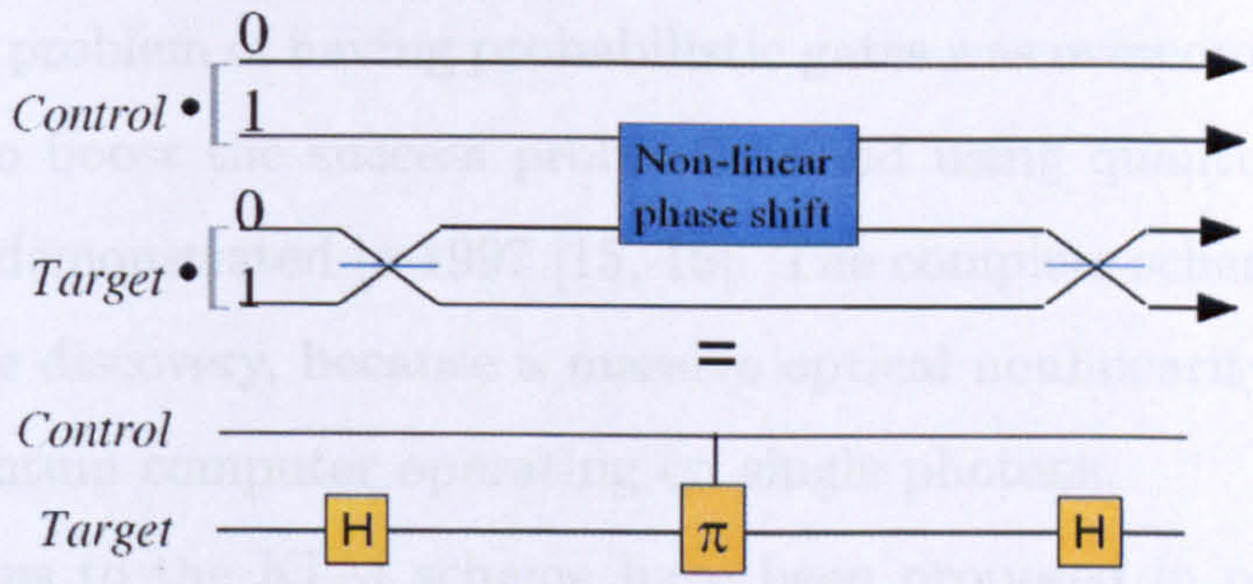

Figure 2.2: In a CNOT gate for path-encoded single-photon qubits, the target photon is input into a Mach-Zender interferometer consisting of two 50% reflective beamsplitters (top). Each beamsplitter implements a Hadamard "H" gate on a path-encoded qubit (bottom). The gate implement a π phase shift only if the control photon is in the '1' path.

as a cross-Kerr medium. However, it quickly becomes apparent that the strength of such a nonlinearity would need to be massive-far beyond the most advanced materials we have yet to conceive.

The requirement for a massive optical nonlinearity was a seemingly impassable roadblock to optical quantum computing until 2001, when Knill, Laflamme, and Milburn (KLM) proposed a radical solution based on inducing such a nonlinearity via single-photon detection [13]. In this scheme we need to introduce additional photons to act much like a catalyst in the gate. For the CNOT gate the control and target qubits, together with two auxiliary photons enter an optical network of BSs, where the paths are combined together in a linear optical network. At the output of this network, the control and target photons emerge, having had the CNOT logic operation applied to their state, conditional on two single photons being detected at particular outputs. Unfortunately the probability of success was not 1, but when successful, the gate would implement the CNOT operation. The rest of the time, another detection pattern is recorded (none, only one, two photons at one detector, and so on) and the CNOT logic is not applied. This type of nondeterministic CNOT gate is of little use for quantum computing because the probability that a computation succeeds decreases exponentially with the number

of CNOTs. The problem of having probabilistic gates was overcome by introducing more photons to boost the success probability and using quantum teleportation [14], which was demonstrated in 1997 [15, 16]. The complete scheme represented a truly remarkable discovery, because a massive optical nonlinearity is not required to realize a quantum computer operating on single photons.

Simplifications to the KLM scheme have been proposed in recent years, and experimental demonstrations have been performed, showing that the implementation of two-qubit gates, as the CNOT, are possible with photons[17–21]. All the demonstrations rely on interactions at the quantum level between photons inside the gate. This kind of interaction (explained in Chapter 3) is the basis for all the linear gates required for the KLM scheme and requires that the photons entering the optical network have exactly the same properties. This "indistinguishability" requirement is very stringent and plays an important role in determining the quality of the quantum computation with photons.

Despite the great progress offered by the KLM sheme, optical quantum computing was still widely regarded as impractical owing to the large resource overhead required to realize a near-deterministic CNOT: more than 10,000 pairs of entangled photons to achieve a success probability of $> 95\%$. The reason that all-optical quantum computing is today a promising route to practical quantum computing is due to new schemes that dramatically reduce this worrying resource overhead [22]. For example, new schemes relying on highly entangled "cluster states" and measurements alone, promise to reduce the requirements needed for quantum computation [23, 24] with photons [25, 26].

2.2.2 Generation of single photons

In this thesis I start from the assumption that single photons at optical frequencies are well characterized physical element with well known properties. I am not entering into the details of what a single photon is, but start from the rather more utilitarian position of saying that we have a single photon every time a single

photon detector "clicks". In this section I will explain briefly how single photons can be produced for quantum information applications.

There are different ways by which it is possible to create single photons. The most common are: atoms, ions, semiconductor sources and non-linear processes (second or third order non-linearities). In this section we will limit ourselves to the process relevant to the experiments performed for this thesis, namely the non-linear process of Spontaneous Parametric Down-conversion (SPDC). This process is a $\chi^{(2)}$ non-linear process, in which one pump photon splits into two daughter photons. SPDC can be described by the following Hamiltonian:

$$H = \hbar g(a_1^\dagger a_2^\dagger a_p + a_1 a_2 a_p^\dagger) \tag{2.6}$$

where $a_i^\dagger$ and a_i are the creation and annihilation operators on the i mode, and g is the coupling constant, with $g \propto \chi^{(2)}$ [27]. The conditions to obtain efficient down-conversion are energy conservation (the sum of the energies of the two daughter photons must be equal to the energy of the pump photon), and a phase matching condition (all the components generated at every point into the crystal are in phase):

$$\omega_p = \omega_1 + \omega_2 \tag{2.7}$$

$$\mathbf{k}_p = \mathbf{k}_1 + \mathbf{k}_2 \tag{2.8}$$

where ω_i and $\mathbf{k}_i$ are the frequencies and wavevector of the photons. These conditions are hidden in the properties of g.

It is possible to distinguish between two types of down-conversion interactions, depending of the properties of the crystal used. They differ in the the relation of the polarization of the created photons. In type-I phase matching, the pump photon is an extraordinarily polarized photon, that splits into two ordinarily polarized daughter photons. Since we are interested in pairs of photons with the same energy, the equations of energy and momentum conservation state that the created photons lie on the cone drawn in figure 2.3.

If we take the case of vacuum input for the quantum fields 1 and 2, and a bright classical field for the pump (as in the case of a laser beam impinging on the

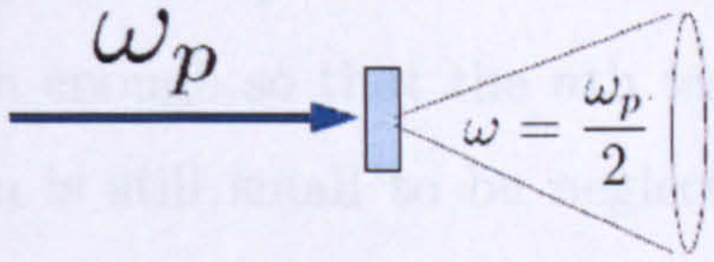

Figure 2.3: Schematic picture of the spontaneous parametric down-conversion process.

non-linear crystal) we obtain

$$|\psi(t)\rangle = e^{-\frac{i}{\hbar}Ht} |\psi(0)\rangle = e^{-\frac{i}{\hbar}Ht} |0\rangle_1 |0\rangle_2 |\alpha\rangle_p \tag{2.9}$$

$$= e^{-\frac{i}{\hbar}(za_1^\dagger a_2^\dagger + z^* a_1 a_2)t} |0\rangle_1 |0\rangle_2 \tag{2.10}$$

$$= e^{f(g,t)a_1^\dagger a_2^\dagger} e^{h(g,t)a_1^\dagger a_1 + a_2^\dagger a_2} e^{-f(g,t)a_1 a_2} |0\rangle_1 |0\rangle_2 \tag{2.11}$$

$$\sim e^{\xi a_1^\dagger a_2^\dagger} |0\rangle_1 |0\rangle_2 = \sum_{n=0}^{\infty} \frac{\xi^n}{n!} a_1^{\dagger n} a_2^{\dagger n} |0\rangle_1 |0\rangle_2 \tag{2.12}$$

$$= \sum_{n=0}^{\infty} \xi^n |n\rangle_1 |n\rangle_2 \tag{2.13}$$

where ξ depends on the crystal parameters (non-linear coefficient, transversal dimensions) and the pump power. If we look at the state obtained we see that

$$|\psi(t)\rangle \sim |00\rangle + \xi |11\rangle + \xi^2 |22\rangle + ... \tag{2.14}$$

where the state $|nn\rangle$ refers to the state with n photons in the two down-conversion modes. This state is the initial state used in the majority of the experiments of quantum information conducted with photons. It is clear, then, that the state is not really composed of single photons in well defined modes. The desired state can be obtained with the combination of detectors. When, for example, we register the click of two single photon detectors we rule out the $|00\rangle$ component and, with a good approximation, the state is projected on the $|11\rangle$ component. This projection is not perfect because usually the single photon detectors are not number-resolving, so higher terms are not distinguished. This problem can be solved adjusting the pump power, so that the terms ξ^n with $n > 1$ are negligible.

With the same technique, multi-photon states can be created. When the power of the pump beam is high enough so that the nth term is high enough to collect data, but the $n+1$ term is still small to be neglected, the n-photon state can be created by the detectors action. In this way, 4 and 6-photon experiments are possible with current technology.

2.3 Quantum Metrology

The continued development of modern science and engineering relies on the precision with which measurements can be performed. To determine the properties of any kind of object, a probe has to interact with the object in such a way that the probe is altered depending on the parameters that have to be determined. Since, in general, the interaction is not efficient enough to obtain the desired accuracy, it is possible to use a repetition of N identical, independent probes, and average the results. From the central limit theorem, for large N the error on the average decreases as $\Delta/\sqrt{N}$, where Δ^2 is the variance of the measurement results associated with each probe.

It is however, interesting to ask if the error on the estimation can be lowered, or if this dependance between the number of probes N and the variance is a fundamental limit. Since in quantum mechanics fundamental relations exist that limit the accuracy of general measurements, the obvious hint is to describe the probe with a quantum mechanical treatment. In particular, it can be shown that, when taking advantage of intrinsic quantum mechanical properties (as entanglement or squeezing) a limit for sensitivity exists [28, 29].

In this Thesis, I focus on the use of photons to perform metrology. A variety of different measurements can be conducted using light as the probe, and measuring optical phase differences caused by the property to be tested. As an example, it is possible to consider the scheme composed by a MachZehnder interferometer to sense an unknown phase ϕ. In this case, the number of photo-detections measured at the output of the device depends on the phase difference between the two

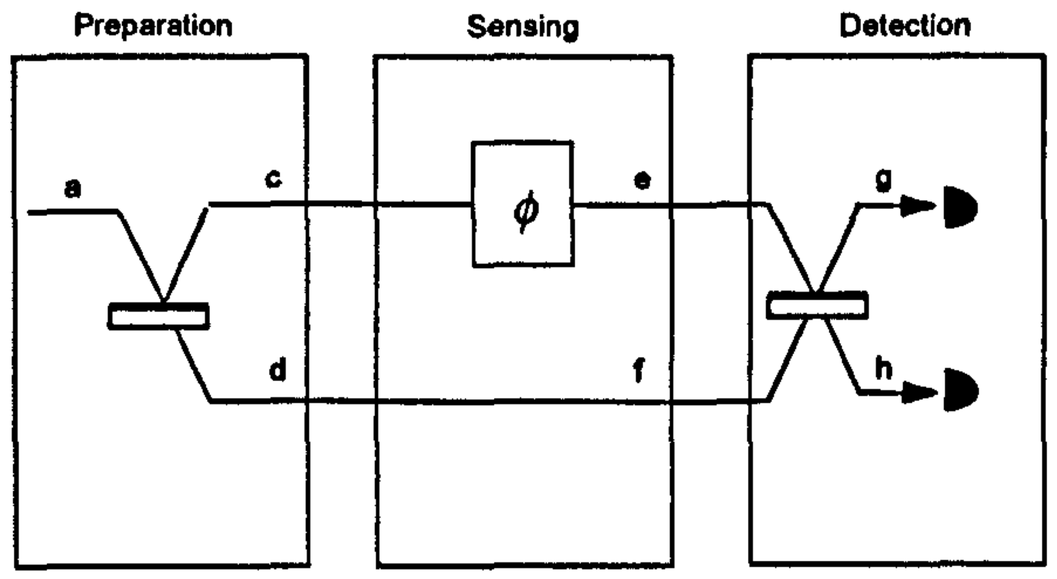

Figure 2.4: Schematic representation of a MachZehnder interferometer used to sense an unknown phase ϕ.

arms of the interferometer. When using classical states of light (or a repetition of independent single photons) to determine the phase shift, the minimum achievable measurement uncertainty scales as $1/\sqrt{N}$, where N is the average total number of photo-detections. This corresponds to the well-known "shot noise limit".

This model, however, corresponds to a classical description of the probe. When a quantum mechanical treatment is used, the evolution of the light can be described in the following way. The single photons entering the first splitter are transformed into a superposition across modes c and d (see figure 2.4):

$$|1\rangle_a \rightarrow |1\rangle_c|0\rangle_d + i|0\rangle_c|1\rangle_d. \tag{2.15}$$

The relative optical phase difference ϕ transform the state as

$$|1\rangle_c|0\rangle_d + i|0\rangle_c|1\rangle_d \rightarrow |1\rangle_e|0\rangle_f + e^{i\phi}i|0\rangle_e|1\rangle_f = |\Psi(\phi)\rangle \tag{2.16}$$

before the two modes are recombined at the second coupler.

For different phase shifts these states are generally non-orthogonal and therefore cannot be distinguished perfectly. When N identically prepared photons are used, the overlap between two states differing by a small phase shift ϕ scales as

[30]:

$$|\langle\Psi(0)|\,\Psi(\phi)\rangle|^{2N} \sim 1 - 1/4(N\phi^2), \tag{2.17}$$

so the precision of the measurement scales as the shot noise limit.

It is possible to look at the MachZehnder interferometer in a different way, in which the first beam-splitter works as the preparation stage and the second splitter is used to detect the phase shift. The question is whether there exists a quantum state that offers better sensitivity in testing ϕ. It can be shown that the maximally entangled N00N states of the form $|N0\rangle + |0N\rangle$ provides better precision than any classical state [31].

In this case, the state after the phase evolves as

$$|N\rangle_c\,|0\rangle_d + |0\rangle_c\,|N\rangle_d \rightarrow |N\rangle_e\,|0\rangle_f + e^{iN\phi}\,|0\rangle_e\,|N\rangle_f = \Phi(\phi) \tag{2.18}$$

where the acquired phase is proportional to the number of photons that pass through the object to sense. The overlap between two states differing by a small phase shift ϕ scales as:

$$|\langle\Phi(0)|\,\Phi(\phi)\rangle|^2 \sim 1 - 1/4(N\phi)^2, \tag{2.19}$$

which corresponds to the ultimate bound defined by quantum mechanics – the Heisenberg limit. This fundamental limit scales as $1/N$, thus showing a great enhancement for the precision of measurements. The challenge of quantum metrology consists in producing states of light, as the N00N states, to exploit quantum entanglement for sensing applications.

2.4 Integrated photonics

In this section I give an overview about how waveguides at optical frequencies work and can be described. This comprises the background for all the simulations I performed to design integrated photonics circuits for quantum information applications.

2.4.1 Waveguides modes

Integrated photonics is based on the confinement of light in optical waveguides by total internal reflection. In order for this to happen, the structure of a waveguide has to be composed by two materials: a lower refractive index material (cladding) has to surround a higher index medium (core). In this way the electromagnetic energy is mostly confined in the internal material, and the light propagation is confined. In a simple ray optics picture, light is confined if it is traveling at an angle to the boundary of the two material that is higher than the critical angle for total internal reflection. If the indices of the core and cladding are n_1 and n_2 respectively, the condition is:

$$\theta_c = \sin^{-1}(n_2/n_1). \tag{2.20}$$

So, if a ray of light is launched into the waveguide with an angle $\theta > \theta_c$ the light cannot escape from the waveguide. If, on the other hand, $\theta < \theta_c$, the ray is not confined into the structure and can escape from the waveguide. This corresponds to a radiation mode.

Total internal reflection is not the only condition that has to be satisfied to have light propagating in a waveguide. To obtain the properties of guided modes it is convenient to imagine a ray entering a semi-infinite waveguide with an angle $\theta \neq 0$. In this case, as displayed in figure 2.5, the ray is traveling on a zig-zag path that forms a round trip. So constructive interference is needed to establish

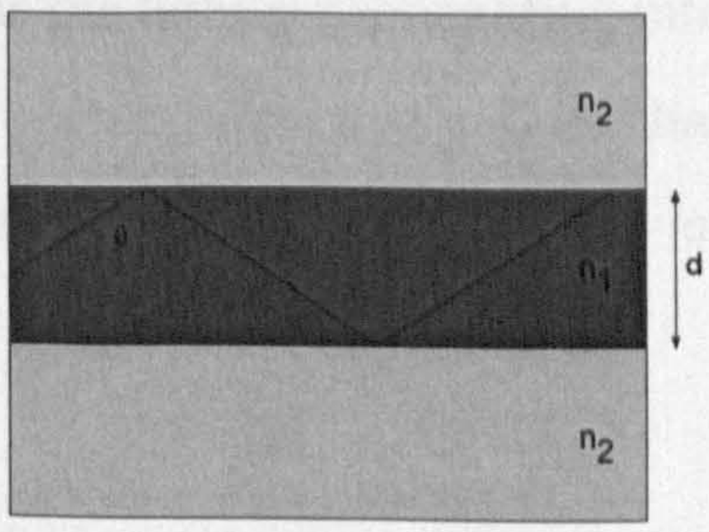

Figure 2.5: Schematic representation of a waveguide.

an allowed propagation mode. Constructive interference is obtained when the transversal phase shift in a round trip is a multiple of 2ϕ. The discrete set of values that satisfy this condition is composed by the angles that correspond to guided modes.

The phase accumulated by the ray depicted in the figure over a round trip in the waveguide is

$$\phi = 2k_x d = 2k_0 n_1 d \cos\theta - \phi_1 - \phi_2. \tag{2.21}$$

where k_x is the wavevector component along the x axis, being $k_0 = 2\pi/\lambda$ the wavevector, and ϕ_r is the phase accumulated by the light in the total internal reflection process [32]. To have constructive interference, the phase accumulated has to satisfy the relation

$$\phi = 2m\pi = 2k_0 n_1 d \cos\theta - 2\phi_r. \tag{2.22}$$

where m is an integer number and is called the mode number. By solving this transcendental equation it is possible to calculate the relation between the modal angle θ_m and the parameters of the waveguide at a given wavelength. However, to obtain the complete information about the light propagating in a waveguide structure, a full electromagnetic approach is needed, since this ray optics model is not a complete representation of the problem. The ray optics approach is useful to obtain a simple picture of what is happening inside the structure, and to obtain approximate solutions.

Under the conditions that the light is propagating into a dielectric, non-magnetic isotropic and linear medium, with refractive indices that vary slowly compared to the fields, the equations that describe the propagation are the Helmholtz equations [33]:

$$\nabla\mathbf{E} + k_0 n^2(\mathbf{r})\mathbf{E} = 0 \tag{2.23}$$

$$\nabla\mathbf{H} + k_0 n^2(\mathbf{r})\mathbf{H} = 0. \tag{2.24}$$

If we take the situation in figure 2.5, then $n(\mathbf{r}) = n(x)$. If we chose z as the

direction of propagation, the solutions of the equations 2.24 are of the form

$$\mathbf{E}(\mathbf{r}) = \mathbf{E}(x)e^{i\beta z} \tag{2.25}$$

$$\mathbf{H}(\mathbf{r}) = \mathbf{H}(x)e^{i\beta z}. \tag{2.26}$$

with β the propagation constant of the electromagnetic wave.

The solutions of the Helmholtz equations can be found of the form TE, where the electromagnetic wave has the only E_y component of the field different from zero, and TM, where the only component of the field different from zero is H_y. For the TE modes, we can write:

$$\frac{d^2E_y}{d^2x} + (k_0^2 n^2(x) - \beta^2) = 0 \tag{2.27}$$

$$H_x = \frac{-\beta}{\omega\mu_0}E_y \qquad H_y = 0 \qquad H_z = \frac{i}{\omega\mu_0}\frac{dE_y}{dx}. \tag{2.28}$$

The first differential equation gives the amplitude profile of E_x for the TE propagation modes in the guiding structure. The solutions are eigenvector solutions that also satisfy the boundary conditions with a discrete set of eigenvalues of β. The nth eigenvalue, ordered as β increases, is called the nth mode of the guided structure TE_n. It is possible to show that the order n is equal to the number of nodes in the field along the y direction. We define a quantity N that satisfies $\beta = k_0 N$ and is called the effective refractive index. The effective index represents the refractive index experienced by the electromagnetic wave traveling in the guiding structure. The confined modes satisfy the relation

$$n_2 < N < n_1 \tag{2.29}$$

since, outside this range, the solutions of the Helmholtz equation are exponential functions, that are not limited in the guiding region and correspond to radiative modes.

In the case of a planar waveguide as in figure 2.5, it is possible to solve independent equations for the three regions of core, upper and lower cladding independently, with the addition of the boundary conditions. The Helmholtz equation for

the three regions can be combined in a single equation [34]:

$$\tan(v\sqrt{1-b}) = \frac{2\sqrt{\frac{b}{1-b}}}{1-\frac{b}{1-b}} \tag{2.30}$$

where the normalized parameters b and V are defined as

$$b = \frac{N^2 - n_2^2}{n_1^2 - n_2^2} \tag{2.31}$$

$$V = k_0 d\sqrt{n_1^2 - n_2^2}. \tag{2.32}$$

Since the effective index N is bounded by $n_2 < N < n_1$, b lies in the range $0 < b < 1$. The normalized film thickness V is proportional to the dimension of the waveguide $V \sim d/\lambda$ and is directly related to the number of guided modes. For a fixed value of V, the equation 2.30 has a given number of solutions of TE and TM fields. If the equation has just one solution, then the waveguide is said to be *single mode*, otherwise the waveguide is *multimode*. For the mode n with $n > 1$, a minimum value of V exists such that for lower values the mode is not guided; this is referred as cut-off. At cut-off it is $N \simeq n_2$, since the mode is weakly concentrated in the core with higher localizations in the cladding regions. Hence $b \simeq 0$. For values of V smaller than the cut-off value the mode is no longer guided, but is rather a leaky mode that radiates into the cladding region.

For waveguides with shapes more complex than the planar waveguide above, numerical solutions must be obtained for the Helmholtz equation. In the next chapter commercial software is described to obtain the properties of the guided modes in the waveguides under study.

Chapter 3

Modeling of waveguides for Quantum Information

In this Chapter I will describe the properties of the material and structures used for quantum information experiments with integrated optics. In particular I will introduce the properties of silica-on-silicon waveguides, and then study all the fundamental components required in this technology to build any linear optical network for quantum optics. I will not describe in detail the properties of silica waveguides, nor the fabrication methods, since these are well known and the fabrication was not conducted at Bristol. For the same reason, I will describe in detail the simulations and properties of waveguides that I calculated, since these are the basis for all the experiments conducted in Bristol with silica-on-silicon circuits.

3.1 Choice of material: silica on silicon

The silica material system is a natural choice for the development of quantum integrated photonic circuits since it exhibits low waveguide losses (< 0.1 dB/cm), couples efficiently to single mode optical fiber and is transparent at wavelengths that match the current state-of-the-art in single photon generation and detection [35]. As in conventional (or classical) integrated optics devices, the light is guided in waveguide structures consisting of a "core" that is surrounded by a slightly lower

refractive index "cladding" (analogous to an optical fiber). These waveguide can be designed to support only a single transverse mode for a given wavelength range, and also to match closely the mode profile of an optical fiber (allowing efficient coupling of photons to fiber-coupled single photon sources and detectors).

The operating wavelength of choice is $\lambda \sim 800$ nm, where commercial silicon avalanche photodiode single photon counting modules (SPCMs) are near their peak efficiency of ~70%. Low waveguide loss and single mode operation for waveguide dimensions comparable to the core size of conventional single mode optical fibers at ~800 nm (4-5 μm) are achieved using standard photo lithography fabrication techniques and low level doping to control the refractive index of silica.

The silica waveguide technology, or planar lightwave circuit (PLC) technology, offers the possibility of integrating a number of passive functions on a single silicon chip [36]. An important example of such functions is optical modulation using the thermo-optic effect. Being able to control optical phases on a chip is crucial for a number of classical and quantum applications. The stability with which the thermo optic effect allows control of optical phase, in combination with polarization-insensitive operation, is the reason why the PLC technology is already being used for quantum communication experiments [37, 38]. In these experiments, unbalanced integrated Mach-Zehnder interferometers were used to analyze time-bin encoded photons to implement quantum key distribution protocols. While these beautiful demonstrations are fundamental for quantum communication operations, they do not prove the capability of PLC in other quantum optics applications, where multiphoton non-classical interference is required.

3.1.1 Properties of Silica waveguides

To realize the first optical devices for Quantum Photonics, silica on silicon waveguides produced by CIP Photonics were chosen. In this section, the reason for this choice and the properties of these waveguides will be explained in details.

CIP is one of the few companies in the world that has the know-how to fabricate

excellent silica on silicon waveguides. The reason is that, even if silica and silicon technologies are mature and well studied, silica waveguides require a particular etching technique to be produced. In particular, the relatively big dimensions of the core region require deep etching in the vertical direction. Controlling the this parameter for long etching time, while preserving the verticality of the side of the waveguides, is extremely challenging.

CIP grows optical devices on a buffer layer made through atmospheric pressure oxidation and then core and cladding layers are made through Flame Hydrolysis Deposition (FHD). The refractive index of the core is controlled by changing the concentration of dopant present in the core layer. The refractive index of the core is often expressed using the Refractive contrast Δ, expressed as:

$$\Delta = \frac{n_1^2 - n_2^2}{2n_1^2}, \tag{3.1}$$

where n_1 and n_2 are the refractive indices of core and cladding respectively. Standard core indices used by CIP are 0.5%, 0.75% and 2%, but other choice are possible, with custom indices in the range $0\% - 3.5\%$. It is important to note that CIP has a excellent know-how in producing waveguides at telecommunication wavelengths, while for Quantum Information applications the wavelength of choice is $800nm$. For this reason, an extensive work of theoretical modeling was necessary to study the optical properties and the dimensions of the waveguides. The starting point for this work is to analyze the properties at telecom wavelength. In table 3.1 it is possible to find the properties of the refractive indices of the materials used for the silica waveguides for three values of the index contrast. An estimate for the optimum radius on curvature of the bends at telecom waveguides is provided. These parameters are the starting point for all the simulations described in this Chapter.

Other important information to keep in mind when choosing the parameters and dimensions of the waveguides are the fabrication tolerances in the fabrication process. CIP quotes process tolerances in the refractive index of ± 0.0002 and in the thickness of the waveguide components as $\pm 0.1\mu m$ for the core and gap width

Table 3.1: Values of the indices and bend radius of silica waveguides at telecommunication wavelengths.

Absolute index @ 1550nm			Minimum Bend Radius
Δ	Core	Clad	R/mm
0.5%	1.4520	1.4450	15
0.75%	1.4560	1.4450	5
2%	1.4740	1.4450	1.5

and $\pm 0.2\mu m$ for the cladding.

It is important to note that the tolerances on the refractive index and the tolerance on thickness imply different strategies to minimize the impact of imperfect fabrication on the performance of the final integrated device. A difference in the indices between the models and samples implies that an optimal choice would be to chose a high index contrast, so that the value of the fabrication tolerance translates to a smaller relative error. The same argument holds for the dimensions of the waveguides, the bigger the core, the smaller the relative error is for the thickness tolerance. From this very simple argument it seems that the optimal choice to minimize the impact of fabrication errors is to have relatively big waveguides (and separations between them) with high index contrasts. However, other requirements exist for the production of integrated circuits. The first constraint is that the waveguides have to support a single guided mode. As explained in the previous chapter, the rule of thumb is that with the increase of the core size, at fixed indices, the number of supported guided modes increases accordingly (through the cut-off value of V). This translates to the result that to obtain single mode operation, structures with small dimension and high contrast, or big dimension and low contrast, should be chosen.

A second constraint to consider for the design is to minimize the total dimensions of the devices (in the propagation direction). The total dimension is mainly limited by the size of two components: bends and couplers. Details of operation for these two components will be presented later in this chapter. The dimension of

bends is just given by the index contrast, since higher indices translate to smaller bends; no design constraint exists in this case. However, a constraint exists for couplers, if the directional coupler geometry is chosen. In these structure the coupling between waveguides is the result of the overlap between the modes of the two waveguides. To obtain small couplers, an appreciable overlap is required. This translates to having cores close together, and/or modes that extend substantially outside the core region. So the optimum choice to obtain small directional couplers is to use low contrasts (that translate to big modes) or small separation between cores.

Extensive preliminary simulations of guided modes and directional couplers were performed on structures with different index contrast and dimensions. These simulations lead to the conclusion that a low index contrast was preferable, given the values of the fabrication tolerances. This choice was dictated by the maximum dimensions possible for the devices and the complexity of the devices that had to be fabricated. Another important factor was that, since CIP had no experience of waveguides for $800nm$ operation, a conservative approach seemed the reasonable one for the very first fabrication run.

The choice of designing waveguides with a index contrast $\Delta = 0.5\%$ relaxes the requirements on the dimension precision, but requires that care is taken to minimize uncertainty in values of the indices. In the remaining of this section it is explained how I minimized the uncertainty for the modeling work.

The values of the refractive indices of the material that compose the waveguides reported in 3.1 are not enough to design the structures, since the values are reported at a wavelength of $1550nm$. The optimum solution to minimize the differences between models and samples would be to use parameters as close as possible to the real ones. Unfortunately CIP was not able to measure refractive indices at the wavelength of interest of $800nm$, given the nature of the apparatus used to perform the refractive index measurements (a prism-based Metricon Corporation apparatus). The first simulations to decide which index contrast was more appropriate were performed using the following approximation. The cladding was

approximated to be fused silica, since the index of this material is in good agreement with the index quoted by CIP at $1550nm$. For the refractive index of the core, a value was chosen in such a way that the index at $800nm$ satisfied the required Δ. Note that this is an approximation because in principle $\Delta = \Delta(\lambda)$, since the core and cladding materials are different and can have different dispersion relations.

To increase accuracy of the simulations, and after the contrast $\Delta = 0.5\%$ was chosen, more information about optical properties of the materials was requested from CIP. The company was able to measure the refractive index of the waveguide components of devices similar to the ones that would have been fabricated on the design provided for Bristol. In particular, measurements at $633nm$ and $1550nm$ were performed. The results are reported in table 3.2.

Table 3.2: Values of the refractive indices of the components used to fabricate the silica-on-silicon waveguides.

Material	633nm	1550nm
Core	1.4638	1.4515
Thermal oxide	1.4578	1.4449
Cladding	1.4564	1.4429

To determine with the best accuracy the refractive indices of the materials at $800nm$, Sellmeier fits were used. The Sellmeier equation gives a relation between the index of a transparent material and the wavelength through coefficients that have to be found experimentally. The equation has the form

$$n^2(\lambda) = \frac{B_1\lambda^2}{\lambda^2 - C_1} + \frac{B_1\lambda^2}{\lambda^2 - C_1} + \frac{B_1\lambda^2}{\lambda^2 - C_1} \tag{3.2}$$

where λ is the vacuum wavelength, and B_i and C_j are the Sellmeier coefficients. Since the Sellmeier equation contains six free parameters, and the points to perform the best fit on were just two, a good initialization of the parameters is extremely important. For this reason I chose to initialize all the parameters as the ones of fused silica, given its similarity with the waveguides materials. The Sellmeier coefficients for fused silica are reported in table 3.3 and the value of the index for

a broad range of wavelength is plotted in figure 3.1 as a black line.

Table 3.3: Values of the Sellmeier coefficients for fused silica.

B_1	B_2	B_3
0.696166300	0.407942600	0.897479400
$C_1(\mu m^2)$	$C_2(\mu m^2)$	$C_3(\mu m^2)$
4.67914826 10^{-3}	1.3512063110^{-2}	97.9340025

The results of best-fits for the values of the refractive indices are plotted in figure 3.1 and the values of the Sellmeier coefficient are reported in table 3.4. Through this best-fits, the values of the refractive indices at $800nm$ were found to be $n_1 = 1.46033$ for the core, $n_t = 1.45406$ for thermal silica and $n_2 = 1.45253$ for the cladding. These are the values used for all simulation and design of waveguides for quantum information applications described in this Thesis.

Table 3.4: Values of the Sellmeier coefficients obtained form the best-fit for the core, cladding and thermal silica materials

Parameter	Core	Thermal	Cladding
B_1	0.70648	0.63685	0.63271
B_2	0.41962	0.46982	0.46964
B_3	0.89748	0.90792	0.94769
C_1	0.00411	0.00423	0.00436
C_2	0.01202	0.01272	0.01299
C_3	97.9340	99.1088	96.9030

3.2 Modeling of silica waveguides

The remainder of this chapter describes the procedure and results of the simulations and designing work of the fundamental components of all the quantum information devices fabricated by CIP, namely straight waveguides, bends, couplers (directional and MMI) and phase controllers. It is worth stressing that these

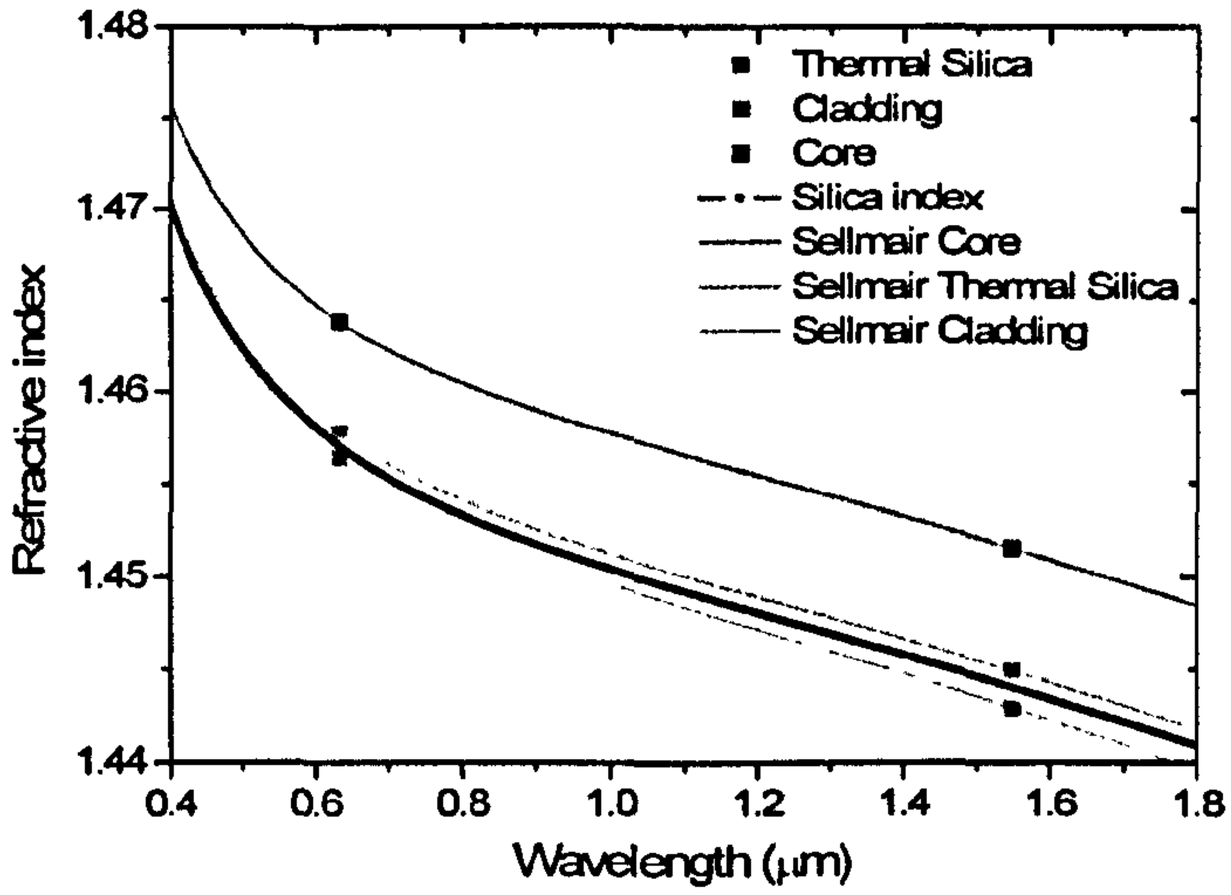

Figure 3.1: Sellmeier fit of the refractive indices of the materials used for core and cladding in the waveguides. The red curve represent the index of pure silica.

components are sufficient to build any optical network required for linear optics quantum information and, more generally, for a broad range of quantum optics experiments.

3.2.1 Guided modes of silica waveguides

The waveguide structure used is illustrated in cross-section in Fig. 3.4. A refractive index contrast of $\Delta = 0.5\%$ was chosen to give single mode operation at 804 nm for 3.5×3.5 μm waveguides [1]. This value of Δ provides moderate mode confinement (the transverse intensity profile is shown in Fig. 3.4A) thereby minimizing the effects of fabrication or modelling imperfections. The devices were fabricated on a 4" silicon wafer (material *I*), onto which a 16 μm layer of thermally grown undoped silica was deposited as a buffer (*II*) to form the lower cladding of the waveguides. The core was formed from 3.5 μm layer of silica doped with germanium and boron oxides which was deposited by flame hydrolysis. The 3.5 μm wide waveguide structures were patterned into this core layer via standard optical lithographic techniques (*III*). An upper cladding (*IV*) of 16 μm was overgrown in

[1] As determined by modeling with the vectorial mode solving package Fimmwave.

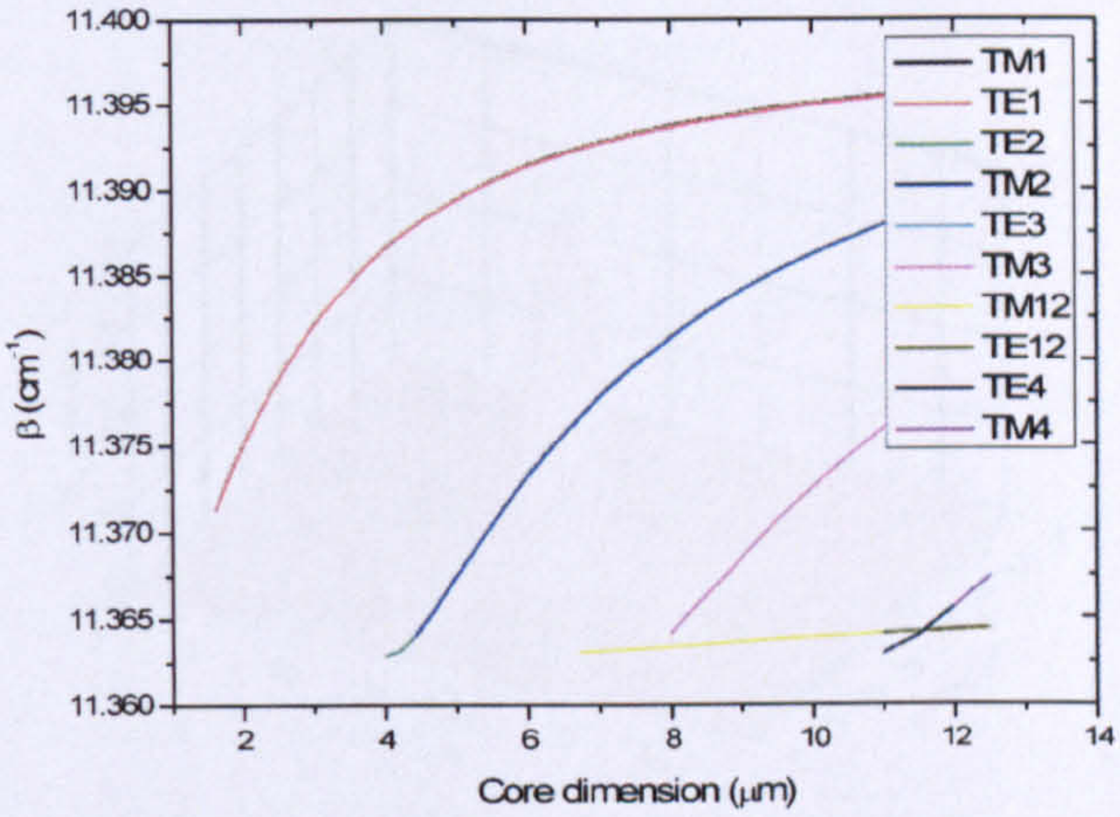

Figure 3.2: Simulation of the propagation constant β of TE and TM guided mode in a Silica on silicon waveguide for different dimensions of the core.

phosphorus and boron doped silica. This layer had a refractive index matched to the lower cladding layer. Metal patterned on the top of the devices provided resistive heaters, metal connections and contact pads that can be used to control locally the temperature of part of the chip. The wafer was diced into individual chips, each containing typically several devices. The facets of some chips were polished to enhance coupling of photons from fibers to the input and output waveguides[2].

A number of devices were designed and fabricated, including directional couplers with various coupling ratios, Mach-Zehnder interferometers (consisting of two directional couplers), and more sophisticated devices built up from several directional couplers with different reflectivities [3].

The fundamental property that has to be satisfied to design the optical network required for quantum information purposes is single mode operation of the waveguides. figure 3.2 shows the values of the propagation constant β of different modes as the dimensions of the core are varied (with a square waveguide shape). It is possible to note that the modes TE and TM of the same order have the same behavior, since there is no birefringence, and that all the modes of order greater

[2]All devices were fabricated at the Centre for Integrated Photonics

[3]We used Rsoft's beam propagation method (BPM) package.

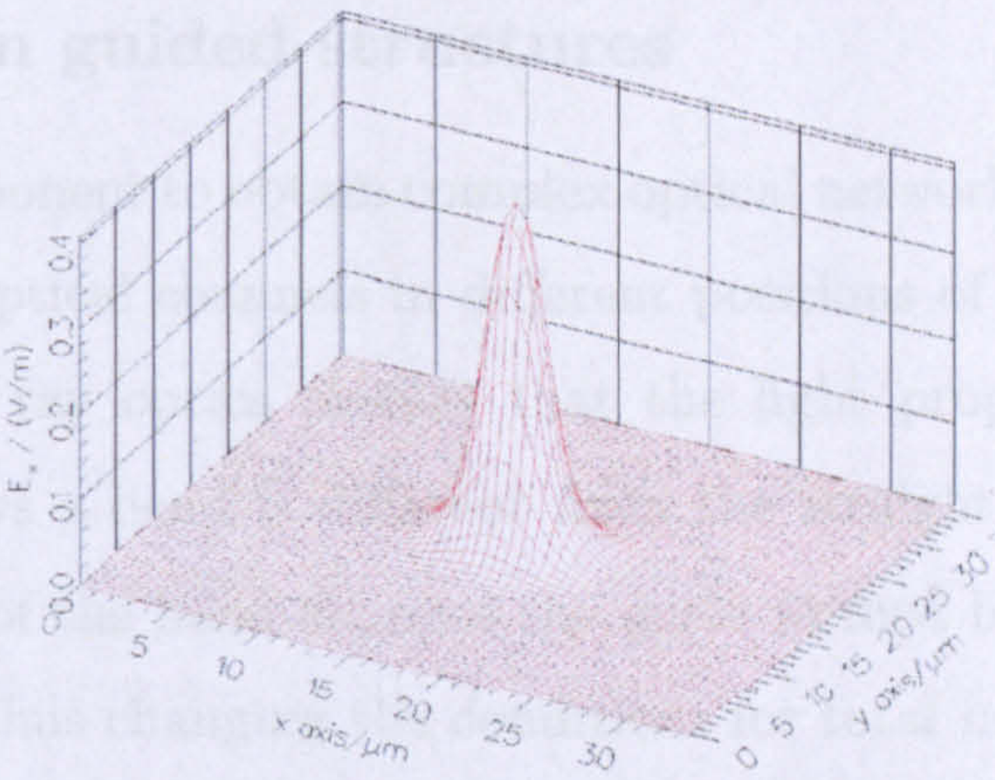

Figure 3.3: Simulation of the TE guided mode in a Silica on silicon waveguide

than 1 approach the same value of β as the dimension decrease. This is the condition for the cut-off value. It is possible to note that for dimensions smaller than around $4\mu m$ the waveguide is essentially single mode. A more precise analysis, combined with a tolerance consideration, lead to the decision to adopt dimensions for the core region of $3.5\mu m \times 3.5\mu m$.

For these values of the core size, and and the refractive index of $\Delta = 0.5\%$ it was possible to obtain all the parameters needed to design the optical networks. Figure 3.3 shows the the mode profile of the guided TE mode in a 3D graph. In figure 3.4 the profile of the mode, and the final layout of the waveguide structure is reported.

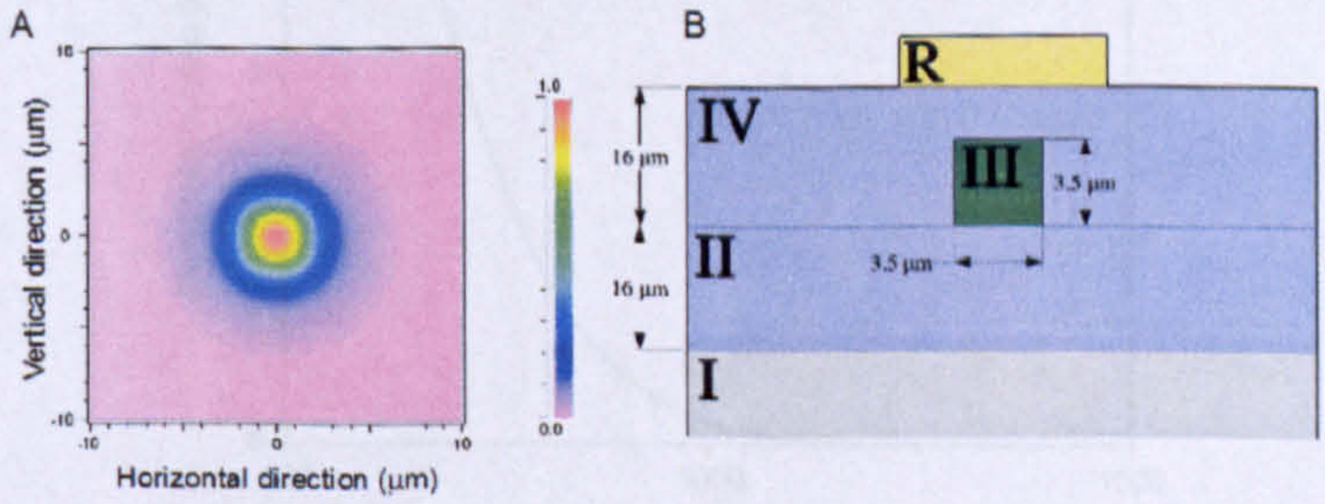

Figure 3.4: Silica on silicon waveguide for quantum photonic circuits. A) Simulation of the transverse profile of the guided mode in the waveguide. B) Schematic figure of the structure of the chip.

3.2.2 Bends in guided structures

A fundamental component to obtain complex optical networks is a bent waveguide, necessary to bring optical channels in different positions of the device. It is clear from a very simple ray optics picture that the light propagating in a guiding structure that follows a bend is different from the straight case. Essentially the radius of curvature of the bend changes the angle formed by the ray of light and the core boundary, thus changing the conditions for total internal reflection. The discrete set of angles for which the light is guided will be changed with respect to the straight case, and losses are expected.

In the case of a single mode structure, a full electromagnetic approach has to be followed to obtain the propagation characteristics of the waveguide. The calculation of the properties of a dielectric optical waveguide represents a complex problem. Nevertheless, the most important property for our purpose, losses introduced by the bend, can be calculated [39]. The attenuation coefficient for a channel waveguide depends strongly on the radius of curvature of the bend R as [40]:

$$\alpha = \frac{q^2}{k^3 N (1 + qw/2)} \frac{h^2}{n_1^2 - n_2^2} e^{qw} e^{-\frac{2q^3}{3N^2k^2}R} \tag{3.3}$$

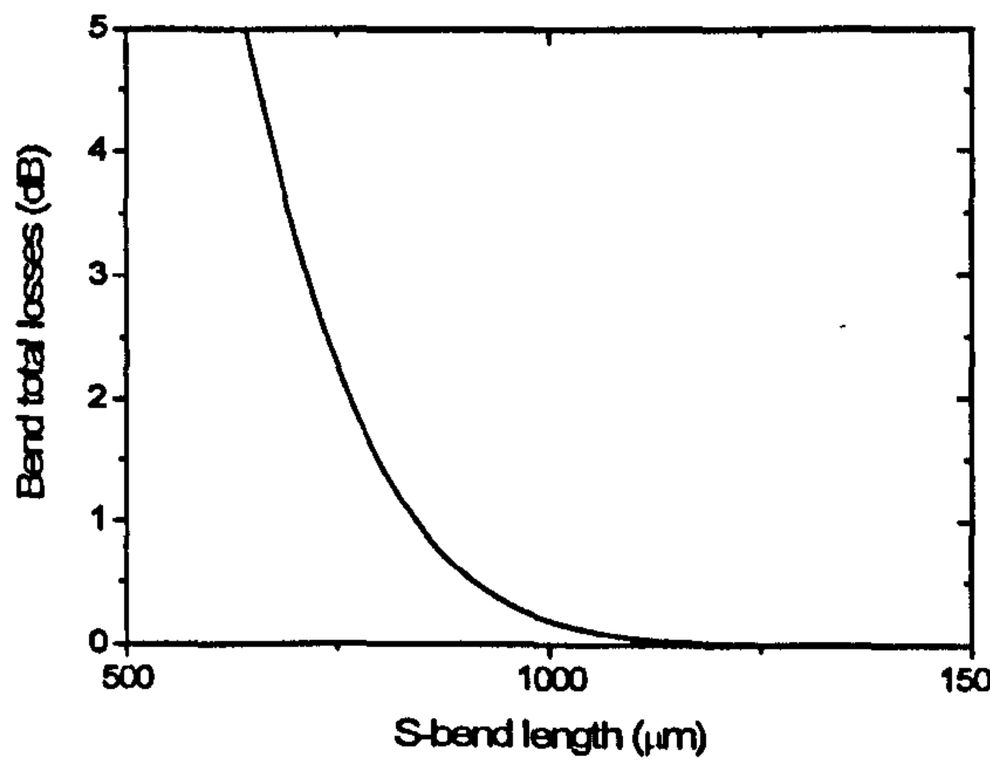

Figure 3.5: Losses in a silica waveguide caused by a bend of radius of curvature R.

where

$$q = k(N^2 - n_2^2)^{1/2} \qquad h = k(n_1^2 - N^2)^{1/2}. \tag{3.4}$$

Usually, inside an integrated device, waveguides have to be brought into proximity at a fixed separation between them, as in the case of a directional coupler structure described in the next section. For this reason a more complex curve structure has to be implemented that is formed by two bends. The structure that best suits this job is a raised-cosine shape. This S-like curve has the property of maintaining the network compact and maximizing the radius of curvature, and hence minimizing losses.

Figure 3.5 shows the behavior of the losses as the length of the raised-cosine is varied for a 3.5×3.5 μm silica-on-silicon waveguide. Additional simulations with BPM codes indicated the best value to limit the losses produced by the bends corresponds to a length of the raised-cosine of $L = 1.5mm$.

3.2.3 Directional couplers in silica waveguides

To realize operations between optical modes, as in free space beam splitters (BS), it is possible to fabricate directional couplers (DC): when two waveguides approach each other the evanescent fields of the two structures overlap and coupling between waveguide is achieved. The coupling ratio of the DC ($1 - \eta$, where η is equivalent to BS reflectivity) can be lithographically tuned by varying the separation between the waveguides and the length of the coupler region (figure 3.6).

It is possible to write the fields in the two waveguides as

$$\Phi_1(x, y, z, t) = A(z)e^{-i\beta_1 z} f_1(x, y)e^{i\omega t} \tag{3.5}$$

$$\Phi_2(x, y, z, t) = B(z)e^{-i\beta_2 z} f_2(x, y)e^{i\omega t} \tag{3.6}$$

where A and B are the amplitudes that take into account the variation of the fields during propagation and $f(x, y)$ is the field distribution in the transverse section of the waveguide. The coupling of the waveguides determine a change of

the amplitudes as [34]

$$\frac{dA(z)}{dz} = -i\kappa B(z)e^{-i(\beta_2-\beta_1)z} \tag{3.7}$$

$$\frac{dB(z)}{dz} = -i\kappa A(z)e^{+i(\beta_1-\beta_2)z} \tag{3.8}$$

where the coupling coefficient κ depends on the spatial overlap of the mode Φ_1 over the region where the properties of the waveguide 2 are changed by its field (or vice versa).

In our case the two waveguides have the same parameters, hence $\beta_1 = \beta_2 = \beta$ (phase matching condition). The propagating fields in the waveguides are then mixed together, and can not be decomposed as single solutions of just one waveguide or the other. Instead we have new modes with

$$\beta_e = \beta + \kappa \tag{3.9}$$

$$\beta_o = \beta - \kappa. \tag{3.10}$$

Since the new propagation constant depends on the coupling constant κ, when the two waveguides are well separated the coupling constant is zero and the fields correspond to the ones of two independent waveguides. When the waveguides are close together the new propagation constant changes and we have $\beta_o < \beta < \beta_e$ with higher separation in the constant as the coupling increases. The new field profiles are a linear combination of the modal fields of the non-interacting waveguides,

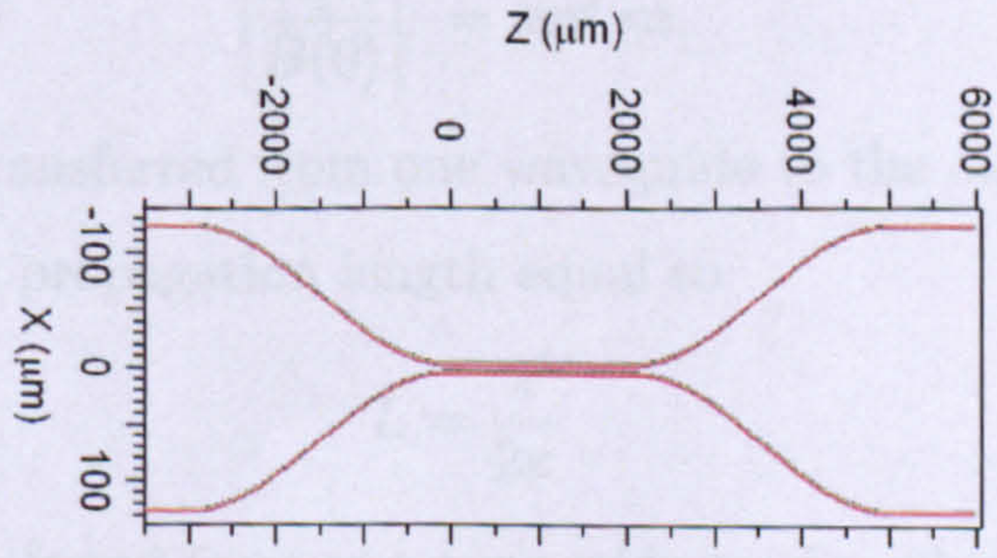

Figure 3.6: Schematic of a directional coupler.

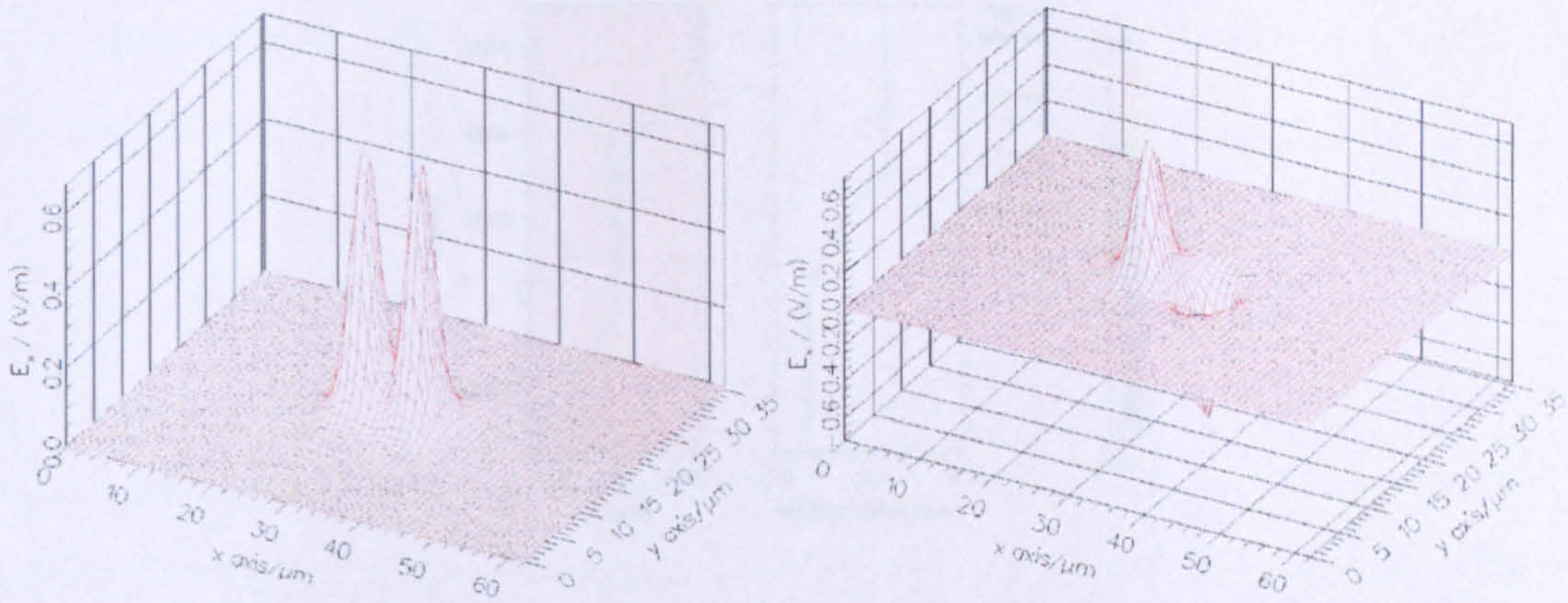

Figure 3.7: Simulation of the TE, odd and even guided modes in a directional coupler. The separation between the waveguides is $3\mu m$.

with

$$\Phi_e = \Phi_1 + \Phi_2 \tag{3.11}$$

$$\Phi_o = \Phi_1 - \Phi_2. \tag{3.12}$$

Figure 3.7 shows the two modes Φ_e and Φ_o for silica waveguides of $3.5\mu m$ at a distance of $3\mu m$.

In the case that one waveguide is excited with an input at $z = 0$, then $A(0) = 1$ and $B(0) = 0$ and during propagation the new coefficients are:

$$\left|\frac{A(z)}{A(0)}\right|^2 = \cos^2 \kappa z \tag{3.13}$$

$$\left|\frac{B(z)}{B(0)}\right|^2 = \sin^2 \kappa z. \tag{3.14}$$

The power is then transferred from one waveguide to the other during the propagation along z. At a propagation length equal to

$$L = \frac{\pi}{2\kappa} \tag{3.15}$$

all the power is transferred from one waveguide to the other. The parameter L is called the coupling length.

Since L goes inversely as the coupling constant κ, we need waveguides with a small separation to obtain good coupling and small propagation constant. This is

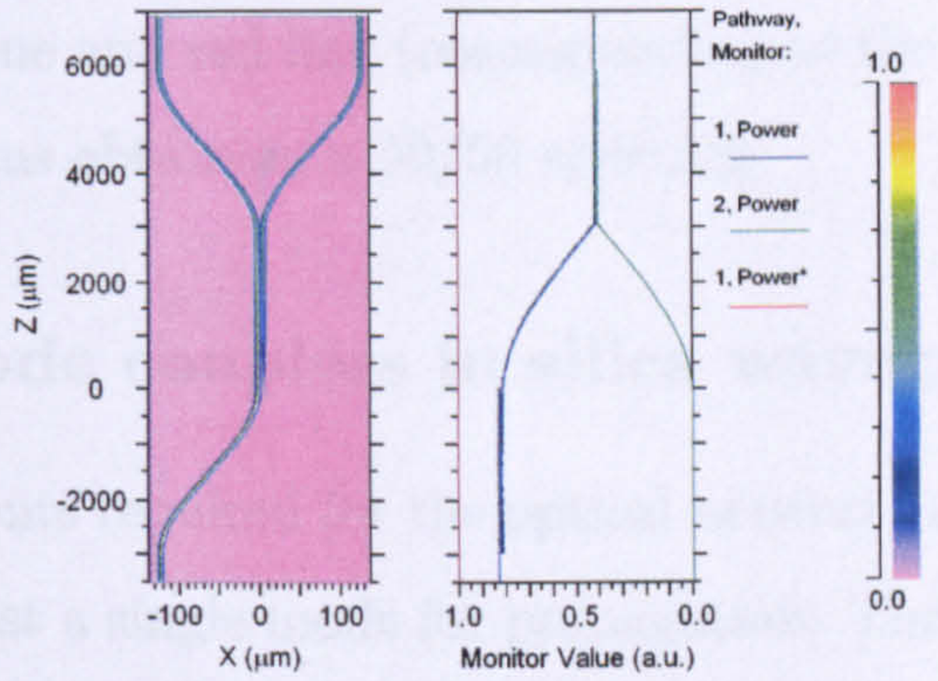

Figure 3.8: Simulation of the power intensity distribution in a directional coupler taking into account also the effects of the input and output bends. The simulation on the right shows the power distribution with the input in the left waveguide (no input in the right waveguide, so the structure in not visible in this plot). The right-hand graph shows the power distribution in the structure. The green and blue lines represent the normalized power in the core section the the right and left waveguides respectively. The red line represents the total power in the structure, and is used to monitor losses.

the reason why a lower index contrast Δ is preferable: at fixed separation between the core regions, the modal fields will be less concentrated and the coupling overlap higher. This implies smaller directional coupler structures and less stringent tolerances on the separation between the core regions.

Since the directional coupler structure is formed by the coupling section and by two bends, it is possible to ask if the presence of the bends modifies the properties of the directional coupler. It is obvious that when the waveguides in the final part of the bends are approaching, the mode overlap starts to increase, and some coupling between the waveguides is present. To take this effect into account, simulations were performed using BPM to study the whole coupler structure (raised-cosine bends plus coupling region). It was found that the effect of the bends corresponds to $250\mu m$ of straight coupling region. Figure 3.8 shows the simulation of a $\eta = 0.5$ coupler. The graph on the right side of the figure provides information on the power in the two channels that compose the splitter. As can be seen, at the end

of the structure the blue and red line (corresponding to the power in the two core sections) are equal, thus obtaining a 50/50 splitting.

3.2.4 Multi-mode couplers in silica waveguides

So far all the components required for the optical network used for quantum information can support just a single mode for propagation. This ensures perfect mode overlap between different fields in the waveguides, so as to obtain good classical and non-classical interference. However, it is possible to design multi-mode waveguides to obtain particular effects and still ensure good performance. An example of such multi-mode component is the multi-mode interference coupler (MMI). MMI devices are based on the self-imaging effect: an input field can be reproduced in single or multiple images along the propagation in a multi-mode waveguide [41].

In a multi-mode waveguide with m modes and width W, the dispersion relation can be written as:

$$\frac{(1+\nu)\pi}{W_e} + \beta_\nu = k_0^2 N^2 \tag{3.16}$$

with ν the number of the mode and W_e the effective width of the fundamental mode:

$$W_e = W + \frac{\lambda}{\pi}\frac{n_2}{n_1}^{2\sigma}(n_1^2 - n_2^2)^{-1/2} \tag{3.17}$$

and $\sigma = 0$ for TE modes and $\sigma = 1$ for TM modes. Introducing the quantity

$$L_\pi = \frac{\pi}{\beta_0 - \beta_1} \simeq \frac{4 n_1 W_e^2}{3\lambda} \tag{3.18}$$

we have that

$$\beta_\nu = \frac{\nu(\nu+2)\pi}{3L_\pi} + \beta_0. \tag{3.19}$$

If we take an input field $\Phi(y, z=0)$ it can be decomposed on the propagating modes of the waveguide ϕ_ν as [42]:

$$\Phi(y,0) = \sum_\nu c_\nu \phi_n u(y) \tag{3.20}$$

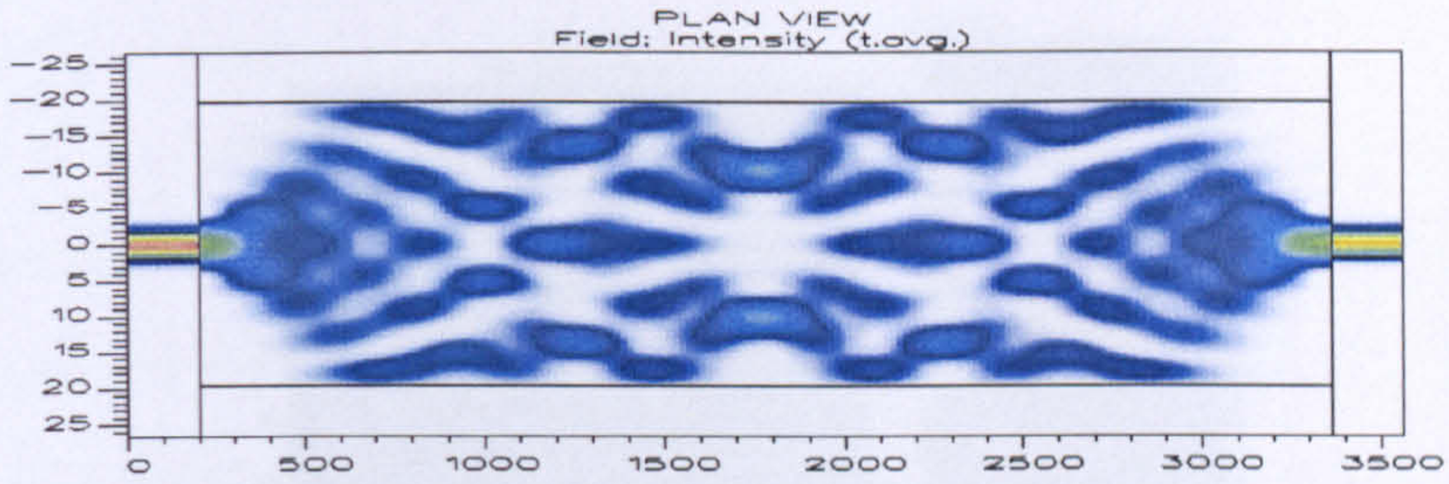

Figure 3.9: Simulation of the propagating mode in a MMI section. It is possible to note point of single and multiple self-imaging.

with c_ν the coefficient representing the overlap of the input mode with the mode ν. It is possible to calculate the field after propagation at z knowing the propagation of the guided modes

$$\Phi(y,z) = \sum_\nu c_\nu \phi_n u(y) e^{i(\beta_\nu - \beta_0)z}. \tag{3.21}$$

From this equation it is clear, then, that the field distribution at the position z depends on the interference between the components of the fields over the guided modes.

The field at $z = L$ can be rewritten as

$$\Phi(y,L) = \sum_\nu c_\nu \phi_n u(y) e^{i\frac{\nu(\nu+2)\pi}{3L_\pi}L} \tag{3.22}$$

and if the exponential is equal to 1 it is easy to note that the field $\Phi(y,L) = \Phi(y,0)$, the condition of self-imaging [43]. This happens for $L = a(3L_\pi)$ with $p \in \mathbf{N}$. This argument can be generalized for multiple copies of the input image, symmetric with respect to the axis of the multi-mode waveguide. Figure 3.9 reports the simulation of the propagation through a multi-mode waveguide. It is possible to note the points during the propagation where the field is a (multiple) image of the input field.

The condition for self imaging in the general case is [44]:

$$L = \frac{p}{M} 3L_\pi \tag{3.23}$$

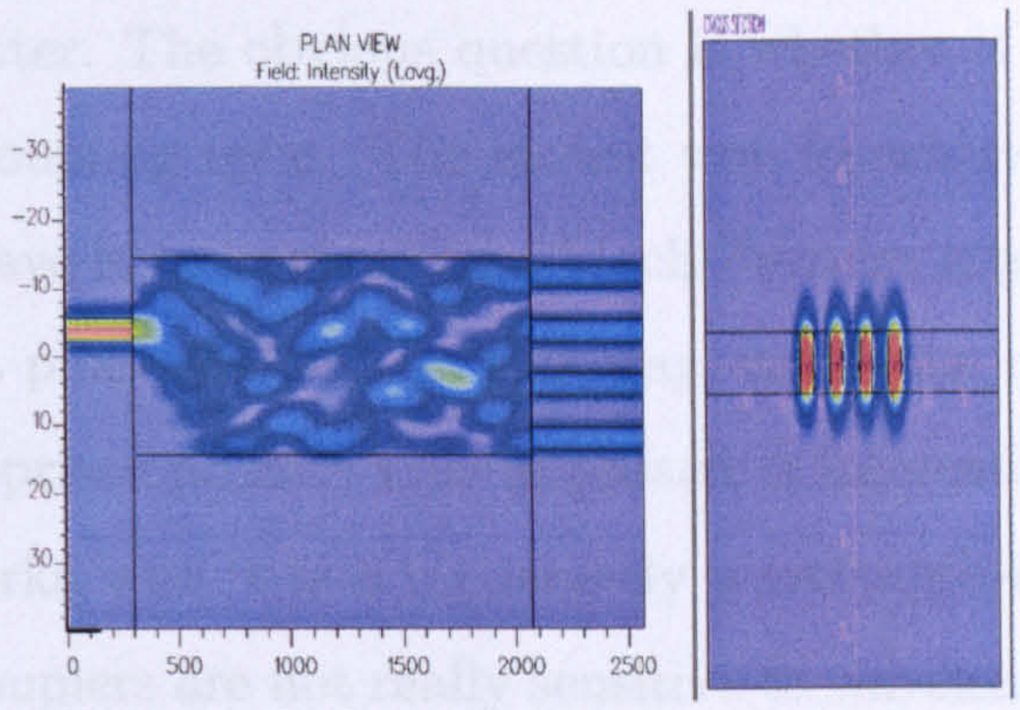

Figure 3.10: Simulation of the propagating mode in a 4x4 MMI coupler.

with $p \geq 0$ and $M \geq 1$ are integers with no common divisors and p indicates the number of self-imaging repetitions along z and M indicates the number of images, each with an amplitude $1/\sqrt{M}$. In this way, symmetric N×M splitters can be designed using a multi-mode waveguide and self-imaging.

Simulations were performed to design 2×2 and 4×4 symmetric couplers. In figure 3.10 the simulated light propagation is shown for a 4×4 MMI coupler. The values of the width and length of the multi-mode section in the couplers are shown in table 3.5. These values have been optimized (with different simulations using BPM) to take into account the residual coupling obtained in the bends before and after the multi-mode section by mode overlap.

The same structure and dimensions were used to design an MMI structure with additional tapering in the input and output single mode waveguides. Tapers to obtain a waveguide width of $4\mu m$ were designed to obtain a less abrupt transition from the single mode waveguides to the MMI section. This should reduce losses since the expansion of equation 3.20 should be composed prevalently by guided modes.

In the above discussion we presented the theory to obtain N×M MMI symmetrical couplers, but in principle it is desirable to obtain any kind of coupling ratio, as for the directional coupler presented in the previous section. For the moment we can limit the discussion to 2×2 couplers. In this case the standard MMI cou-

pler is a $\eta = 0.5$ splitter. The obvious question is whether it is possible to obtain other values of the coupling ratio. The easiest way to achieve any ratio with the devices we already have is to implement a Mach-Zehnder interferometer with two MMI couplers and a phase shifter. In this way, any value of η can be achieved by setting the appropriate phase. This approach is interesting because it allows reconfigurable networks, and it is a moderately wavelength-independent solution (because the MMI couplers are not really sensitive to wavelength variations, so for a not too broad range of frequencies the right phase can be selected to obtain the desired ratio), on the other hand it is resource intensive and uses three components to obtain an elementary element. A solution exists, fabricating multi-mode sections with different geometries. This allows for different splitting ratios to be implemented [45].

3.2.5 Integrated phase control

The control of optical phases inside the integrated chip is fundamental for a range of different tasks. The simplest one is that, if the optical phase inside a network is not precisely set to the desired value, it is possible to change the propagation properties by adjusting the phases after fabrication. In this way, adjustable phases allow the correction of non-perfect fabrication and tolerances. This is true in particular, when different paths have to interfere and the phase difference has to be set to a particular value, so that the geometrical paths do not have to be the same. However, obtaining precise optical phases by adjusting the paths difference in the fabrication process is not always simple. A tunable, internal, phase is then

Table 3.5: Values of physical dimensions of the multi-mode section to achieve 2×2 and 4×4 MMI couplers.

Coupler	Width	Length
2×2	$15\mu m$	$1090\mu m$
4×4	$29\mu m$	$1770\mu m$

more practical.

Also, tunable phases are required to obtain reconfigurable circuits. For example, interferometers can be used in conjunction with variable phases to obtain different single photon operations, as will be explained in Chapter 6. The same components can be also used to route photons in different parts of the network, so to obtain a reconfigurable architecture.

Precise control of the optical phases is needed also for quantum metrology experiments. It is obvious that proof of principle demonstrations, where a known phase is sensed to test the properties of the quantum scheme used, require the control of the circuit. But, ultimately, the majority of quantum metrology schemes require the use of an additional known phase while sensing the unknown one. The known phase is used to set the quantum circuit at the operation point where the sensitivity is maximum. For this task, absolutely precise control of the circuit is needed, otherwise errors are transferred on the reconstruction of the measure under study.

For such a big range of different tasks, different requirements are needed in terms of precision, range of tunability and speed of reconfiguration. Different systems and materials can be used to obtain the control of optical phases inside an integrated circuit. However, in the case of the material under study, silica on silicon waveguides, the simplest method to control the propagation is via thermo-optical effects.

In this case, changing the temperature of the material changes its refractive index. In this way the optical path is controlled and so the optical phases. Even though the phase can be controlled with a good accuracy, the thermo-optical effect suffers from a few limitations. The most important one is that the effect is quite slow, since it is not possible to obtain fast changes of temperatures on the chip, and a steady state has to be reached. For this reason thermo-optical manipulation of integrated phases can be used for the quantum processes that do not require ultra-fast operation. For example, reconfigurations of optical circuits or the setting of the correct phases in the networks are not required to be fast. For the same reason,

the majority of quantum metrology schemes do not require fast manipulations of the known phase in short timescales. Conversely, thermo-optical processes can not be used for feed-forward processes such as the ones required in cluster state computation [23, 46], otherwise long integrated optical delays are required. For these kind of tasks, ultra-fast effects, as the electro-optic effect in lithium niobate waveguides, are better suited.

The thermo-optical effect for silica waveguides produced by CIP works as follow. A metallic layer is deposited on the top of the silica chip to provide resistive heaters (made of a combination of Ti/Pt), metallic connections and contacts to physically control the phase inside the interferometer (made of a combination of Ti/Pt/Au), see figure 3.4. When a voltage is applied across the resistive element, heat is generated which dissipates into the device and locally raises the temperature T of the waveguide structure directly beneath the resistor. A change in the temperature of the waveguide provides a temperature change in its core and cladding. To a first approximation, the change in refractive index n of silica is given by [47] $dn/dT = 10^{-5}/\mathrm{K}$, independently of the compositional variation of core and cladding. This induces a phase difference with respect to the unperturbed waveguide. The heat generated inside the resistive elements dissipates through the depth of the structure to the silicon substrate which acts as a heat sink.

Simulations were performed to calculate the required length of the resistive element on the waveguide to obtain the desired phase change. To obtain this value it is necessary to know the maximum temperature rise allowed by the resistive element. Data from CIP showed that a temperature change of about $30 - 40^{o}$ is possible. With this value, simulations of the guided modes of the waveguides were analyzed, taking into account that both core and cladding indices vary in the same way. The perturbed structure has a new effective index N_T that depends on the temperature. Knowing the unperturbed and perturbed effective indices it is possible to calculate the required propagation length to obtain a given phase shift. The final design was based on the possibility of obtaining a 3π total phase-shift at maximum temperature change. This value was decided to consider a margin

to be able to obtain a total 2π required for quantum operation. The interaction length, and then the length of the resistive element, required to obtain this phase was calculated to be 4 mm.

3.2.6 Integrated polarization manipulation

All the elements studied in this Chapter have properties that are essentially independent of the polarization, since the birefringence of the silica waveguide is negligible. A small birefringence is present and caused by the fact that upper and lower cladding do not have exactly the same optical properties. This is beneficial if a single polarization is used inside the integrated circuit, since, if the input field is polarized in the same direction as one of the axis of birefringence, the propagation maintain the polarization properties. This is the case for the studied waveguides, since the birefringence axes are the horizontal and vertical ones, and they do not change inside the optical circuit. It is sufficient to launch a vertical or horizontal field to obtain no polarization rotations. All the quantum operations and the information encoding are then possible using the path degree of freedom, neglecting completely polarization.

It is, however, interesting to study the possibility of obtaining polarization diversity operations. This would allow for the combination of quantum operations in more degrees of freedom, as well as the direct use of all the schemes used in free space operation, where commonly the polarization degree is used to obtain quantum operations.

As said above, the silica waveguides do not present natural birefringence, essentially because the material is amorphous and so isotropic for all polarizations. The solution could be to obtain polarization diversity through a *shape birefringence*, obtained designing non-symmetric waveguides.

Various simulations were performed on silica-on-silicon waveguides with different dimensions. The result was that the key element for polarization operation, a polarizing beam-splitter (PBS) that divides the vertical and horizontal compo-

nents, is not possible in the system under study. Different schemes can be found in the literature to obtain integrated PBS operation. For example using a directional coupler with a length so that one polarization sees a propagation length that is an even multiple of the coupling length and the other a odd multiple. In this way the two polarization components of the input field are coupled in the different outputs of the directional coupler [48, 49]. Other schemes are based on the coupling of the input field with additional waveguides (usually multi-mode) to obtain PBS operation [50, 51]. However, all the schemes are based on the difference of the propagation properties of the two polarizations. The schemes based on the coupling of one mode with additional metal layers [52] are not a good choice for quantum information applications, because they involve losses, so they can not implement unitary evolutions.

Unfortunately, using a low index contrast of $\Delta = 0.5\%$ means that the birefringence that it is possible to introduce in the system by just changing the shape of the waveguide is small. Essentially, since the effective indices are close to the index of the cladding (because the field is not strongly confined), variations of the shape can not change the field profile much. Moreover big shape variations are not possible because, if the waveguide exceeds a cut-off value of the dimension, multi-mode operation is obtained. The fact that the propagation characteristics of the two polarizations are very similar means that they behave in more or less the same way, and it is then difficult to obtain different operations for different polarizations.

Although all the simulations were not useful to design silica-on-silicon circuits with polarization operations, the necessary study and the general schemes have been used to design waveguides in SiO_xN_y, where the higher index contrast allows polarization diversity operations. The results of this study, however, are not part of this thesis.

Chapter 4

Integrated couplers

This Chapter contains the experimental results obtained from the integrated devices containing integrated couplers, probably the most important building block in any linear optical network. The properties of the couplers are analyzed regarding the quantum information perspective, using single photons. In particular, I will describe in detail the results obtained from non-classical interference experiments. I will analyze the two structures described from the simulation point of view in Chapter 3, directional couplers and multi-mode interference couplers.
This Chapter is based on the results published in the following articles:

A. Politi , M. J. Cryan, J. G. Rarity, S. Yu, and J. L. O'Brien, Silica-on-Silicon Waveguide Quantum Circuits, *Science* **320**, 646 (2008);

A. Politi, J. C. F. Matthews, M. G. Thompson, J. L. O'Brien, Integrated Quantum Photonics, *Journal of Selected Topics in Quantum Electronics*, **15**, 6, 1673-1684, (2009);

A. Laing, A. Peruzzo, A. Politi, M.R. Rodas, M. Halder, T. C. Ralph, M. G. Thompson, J. L. O'Brien, Towards fault tolerant quantum photonic circuits, *Submitted*;

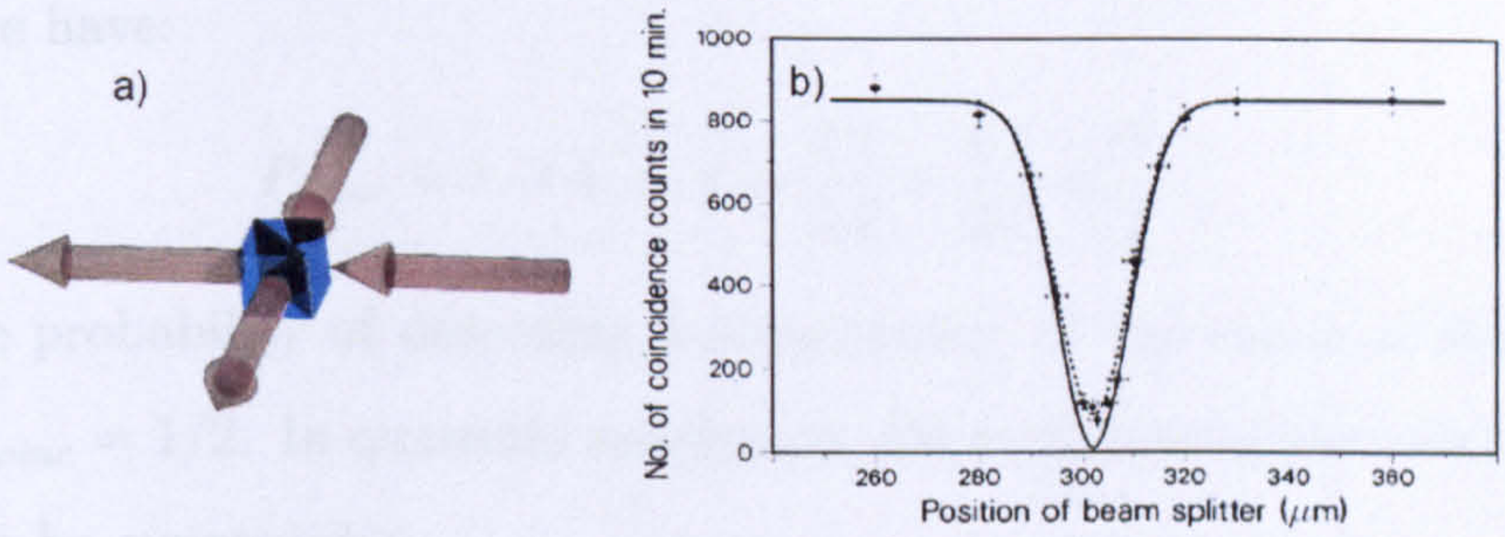

Figure 4.1: Non-classical interference expreriment.a) schematic picture of the experiment, b) Number of coincidences changing the arrival time of the two photons at the beam-splitter [3].

4.1 Non-classical interference

In quantum optical architectures, information is encoded onto single photons propagating in superposition along multiple optical paths or "modes". The heart of quantum processing is therefore a linear optical network based on classical and (quantum) non-classical interference[3] between photons to split and combine optical modes. In conventional large-scale (bulk) optical implementation of linear networks, photons propagate in free space and optical circuits are constructed using standard mirrors and "partially reflective mirrors" or beam splitters (BS). Such devices act on individual photons so that their state evolves into superposition of many paths.

Non-classical interference is an effect that can be observed when two indistinguishable photons arrive at the different inputs of a beam-splitter at the same time [3]. The scheme of the experiment is depicted in figure 4.1. Following the classical physics description, the probability of detecting one photon at each output port of the beam-splitter is given by the sum of the probabilities that allow for this event (i.e. both photons being reflected and both photons being transmitted). If the beam-splitter is half-transparent (or 50:50) reflectivity (transmissivity) is equal to

1/2, and we have:

$$P_{coinc} = t \cdot t + r \cdot r = \frac{1}{2}\frac{1}{2} + \frac{1}{2}\frac{1}{2} = \frac{1}{2} \tag{4.1}$$

so that the probability of detecting a coincidence, in the classical description, is equal to $P_{coinc} = 1/2$. In quantum mechanics, the evolution of the two input modes a and b can be expressed as

$$\begin{pmatrix} c \\ d \end{pmatrix} = \begin{pmatrix} \sqrt{\theta} & \sqrt{1-\theta} \\ \sqrt{1-\theta} & -\sqrt{\theta} \end{pmatrix} \begin{pmatrix} a \\ b \end{pmatrix}. \tag{4.2}$$

where θ is the reflectivity of the beam splitter. Then, sending two photons at the entrance of the BS we obtain the evolution

$$|\psi_{out}\rangle = \sqrt{\theta(1-\theta)}(|20\rangle_{cd} + |02\rangle_{cd}) + [(1-\theta) - \theta]\,|11\rangle_{cd}. \tag{4.3}$$

The probability of finding one photon in output c and one in d is given by

$$|\langle 11|\,\psi_{out}\rangle|^2 = (1-2\theta)^2 \tag{4.4}$$

Then, for the choice $\theta = 1/2$, that is a 50:50 beam spitter, the coincidences in the quantum case go to zero. This effect is possible because of the "interference" between the terms coming from the possibilities of having both the photons reflected or having both the photons transmitted. If, for any reason, the two processes can be distinguished, the terms do not sum, and the quantum probability of coincidences has the same value as the classical one. This translates in the conditions of having photons arriving at the beam-splitter with exactly the same properties (same frequency, same arrival time, same spatial mode, same polarization).

Figure 4.1b shows a plot of the number of coincidences as the arrival time of the photons at the beam-splitter is varied. The plot is taken from the original experiment performed by Hong, Ou and Mandel, who first measured the non-classical interference effect (for this reason, this experimental non-classical interference pattern is called HOM dip). In this graph it is possible to note the dip in the coincidence number when the arrival time of the two photons at the beam-splitter is changed. This is the transition from the classical to the quantum case, when

the photons are partially distinguishable and the non-classical interference is not complete. Note that the dip does not reach the zero line because of experimental imperfections, the two photons have some properties that are not exactly the same, leading to a non-perfect quantum interference.

4.2 Coupling ratio of an integrated splitter

Inferring the reflectivity of an integrated coupler can look like a quite difficult task, since the light measured at the outputs is a combination of the reflectivity/transmissivity, the losses and the different coupling efficiencies at the inputs/outputs. At first glance this problem is impossible to solve, since we have many more unknowns than equations. However these equations are coupled together, and it easy to demonstrate we can measure the maximum visibility of the HOM dip for a given coupler (maximum in the sense that we assume the visibility is only limited by a reflectivity $R \neq 1/2$). We assume the most general case of an integrated coupler, as represented in figure 4.2, in which $R + T \neq 0$ due to losses, and the reflectivities (and transmissivities) for the two channels are not equal ($R_1 \neq R_2$, $T_1 \neq T_2$).

If we launch light into one input at a time, we can calculate the number of photons N_c and N_d detected at the two outputs as

$$N_a^c = pM\eta_a R_1 \eta_c \tag{4.5}$$

$$N_a^d = pM\eta_a T_1 \eta_d \tag{4.6}$$

$$N_b^c = pM\eta_b R_2 \eta_c \tag{4.7}$$

$$N_b^d = pM\eta_b T_2 \eta_d \tag{4.8}$$

where N_j^i represent the number of photons detected at the output j coming from the input i, η_i is the coupling efficiency at the input/output i, p and M indicate the probability of producing a photon and the production rate respectively. We can call A_M the ratio

$$\frac{N_a^c}{N_a^d}\frac{N_b^d}{N_b^c} = \frac{R_1 R_2}{T_1 T_2} = A_M \tag{4.9}$$

that depends on the properties of the coupler and not on the coupling efficiencies.

We look now at the case when we send two photons into each arm of the coupler. The classical probability of a coincidence detection at the output c and d is given by

$$P_c = p^2\eta_a\eta_b\eta_c\eta_d(R_1R_2 + T_1T_2). \tag{4.10}$$

In the quantum case:

$$\begin{aligned} a_a^\dagger a_b^\dagger|0\rangle &\rightarrow (a_c^\dagger\sqrt{R_1} + a_d^\dagger\sqrt{T_2})(a_d^\dagger\sqrt{R_2} + a_c^\dagger\sqrt{T_1})|0\rangle \\ &\rightarrow \ldots|20\rangle + \ldots|02\rangle + p\sqrt{\eta_a\eta_b\eta_c\eta_d}(\sqrt{R_1R_2} - \sqrt{T_1T_2})|11\rangle \end{aligned} \tag{4.11}$$

and the probability of a coincidence is given by

$$P_q = p^2\eta_a\eta_b\eta_c\eta_d(R_1R_2 + T_1T_2 - 2\sqrt{R_1R_2T_1T_2}). \tag{4.12}$$

The visibility of the HOM dip is given by

$$\begin{aligned} V &= \frac{P_c - P_q}{P_c} \\ &= \frac{p^2\eta_a\eta_b\eta_c\eta_d(R_1R_2 + T_1T_2) - p^2\eta_a\eta_b\eta_c\eta_d(R_1R_2 + T_1T_2 - 2\sqrt{R_1R_2T_1T_2})}{p^2\eta_a\eta_b\eta_c\eta_d(R_1R_2 + T_1T_2)} \\ &= \frac{2\sqrt{R_1R_2T_1T_2}}{R_1R_2 + T_1T_2} \end{aligned} \tag{4.13}$$

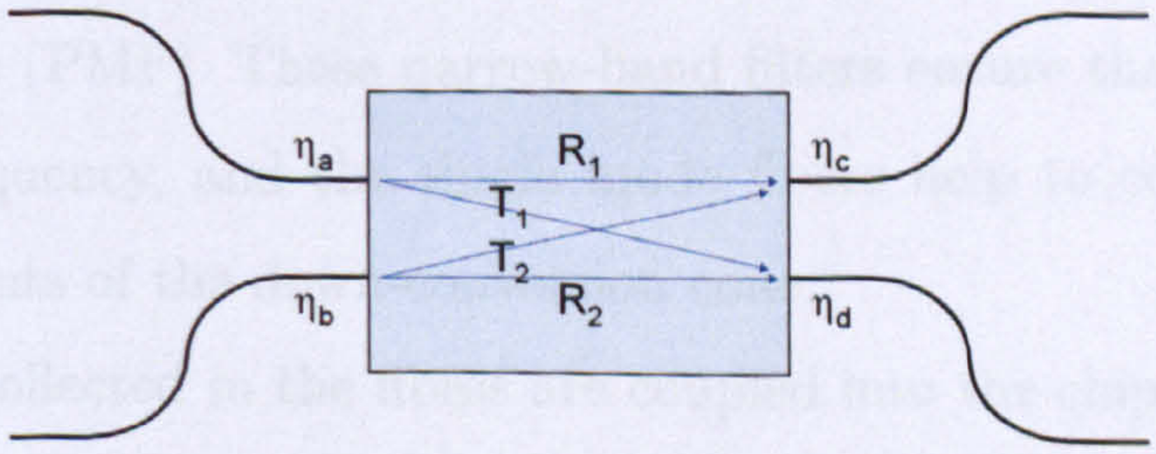

Figure 4.2: Schematic representation of a coupler.

and we can write, remembering equation 4.9

$$V = \frac{2\sqrt{\frac{R_1 R_2}{T_1 T_2}}}{1 + \frac{R_1 R_2}{T_1 T_2}} = \frac{2\sqrt{A_M}}{1 + A_M}. \tag{4.14}$$

This last equation links the measurable output photon numbers with the optimal Visibility of the quantum interference for a given coupler.

In the case of a directional coupler, the approximations $R_1 = R_2 = R$ and $T_1 = T_2 = T$ are accurate, since the structure of the coupler is symmetric by construction. In this case, it is easy to simplify all the above equations, and also the reflectivity of the couplers can be measured with the same method. If we also take $R + T = 1$ we get

$$R = \frac{\sqrt{A_M}}{1 + \sqrt{A_M}}. \tag{4.15}$$

4.3 Experimental details

The single photons utilized for all the measurements presented in this Chapter, and for all the two-photon experiments of this Thesis, were produced with the source schematically shown in figure 4.3. The source consists of a 402 nm laser diode shining onto a type I BBO SPDC crystal. The diode is a Toptica iBeam laser that provides up to 60mW of power. The photons produced from down-conversion pass through 2nm wide interference filters and are collected by single mode polarization maintaining fibers (PMF). These narrow-band filters ensure that the photons are degenerate in frequency, and the single mode fibers help to collect the photons from opposite points of the down-conversion cone.

The photons collected in the fibres are coupled into the chip using an array of 8 PMF separated by 250μm. The PANDA style PM fibres are positioned inside the V-groove array to have the polarization axis (stress rods) aligned vertical to the V-Groove. The overall tolerance in the alignment of the PM axis, taking into account the array positioning and the connectors, is of the order of 3°. The separation of the fibres coincides with the separation of the waveguides inside the integrated chip. The light is butt-coupled from the array to the chip with the

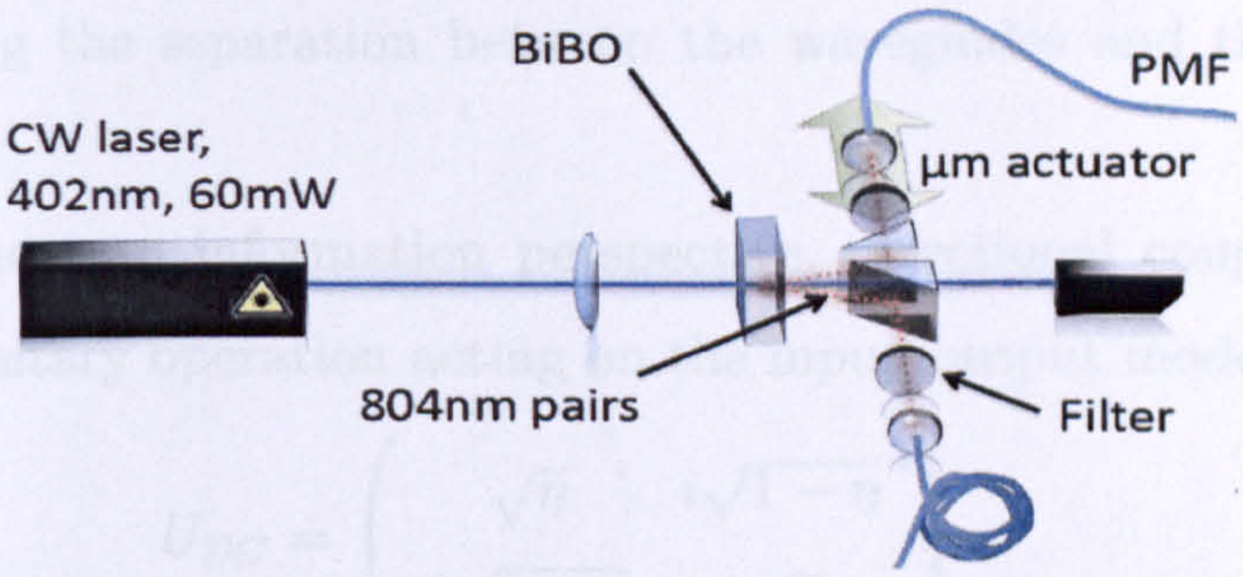

Figure 4.3: Schematic of the single photon source used to perform all the two-photon experiment presented in this Thesis.

help of a micro-positioning six-axis stage used to accurately align the array to the chip. The coupling of light is enhanced using a fluid that has the refractive index to match the one of silica. This presents back-reflection at the facets of the fibres and the chip, also decreasing the effect of non-perfect polishing of the devices. The photons, after the propagation through the chip, are coupled into an array of 8 PMF or single mode fibres, adopting the same method used for the input. The overall coupling efficiency in and out of the chip (also considering the propagation losses) can be estimated as approximately 70%. The photons are finally detected using single photon detectors SPCM-AQR from Perkin-Elmer. The TTL electronic pulses produced by the detectors are controlled by a Stanford Lab SR400 instrument, that elaborates the electronic signals to compute single counts and coincidental events between different channels.

4.4 Directional couplers

To realize operations between optical modes, as in free space beam splitters (BS), it is possible to fabricate directional couplers (DC). As explained in Section 3.2.3, when two waveguides approach each other the evanescent fields of the two structures overlap and coupling between waveguide is achieved. The coupling ratio of the DC ($1-\eta$, where η is equivalent to BS reflectivity) can be lithographically

tuned by varying the separation between the waveguides and the length of the coupler region.

From the quantum information perspective, directional couplers can be described by an unitary operation acting on the input/output modes, as

$$U_{DC} \doteq \begin{pmatrix} \sqrt{\eta} & i\sqrt{1-\eta} \\ i\sqrt{1-\eta} & \sqrt{\eta} \end{pmatrix}. \tag{4.16}$$

Note that for $\eta = 1/2$ the directional coupler is equivalent to a Hadamard gate H

$$H \doteq \frac{1}{\sqrt{2}} \begin{pmatrix} 1 & 1 \\ 1 & -1 \end{pmatrix}, \tag{4.17}$$

up to local σ_z rotations.

To demonstrate that silica on silicon technology is an excellent candidate to implement quantum circuits, it is necessary to show that it is possible to achieve quantum interference between single photons. Figure 4.5A shows the rate of coincidental detection of two photons at the output waveguides of a directional coupler as arrival time delay between the photons is changed. The expected dip near zero delay in relative photon arrival time indicates the quantum behavior of the system. The depth of such a dip indicates the degree of quantum interference, which can be quantified by the visibility $V = (N_{max} - N_{min})/N_{max}$. Ideally the visibility is a function of the reflectivity η:

$$V_{id} = \frac{2\eta(1-\eta)}{1-2\eta+2\eta^2} \tag{4.18}$$

and in experiments it can be reduced by any process that limits the indistinguishability of the single photons. The measured visibility $V = 94.8 \pm 0.5\%$ quantifies

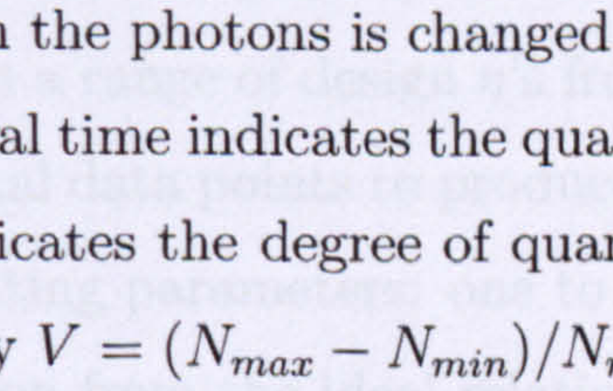

Figure 4.4: Schematic of an integrated directional coupler.

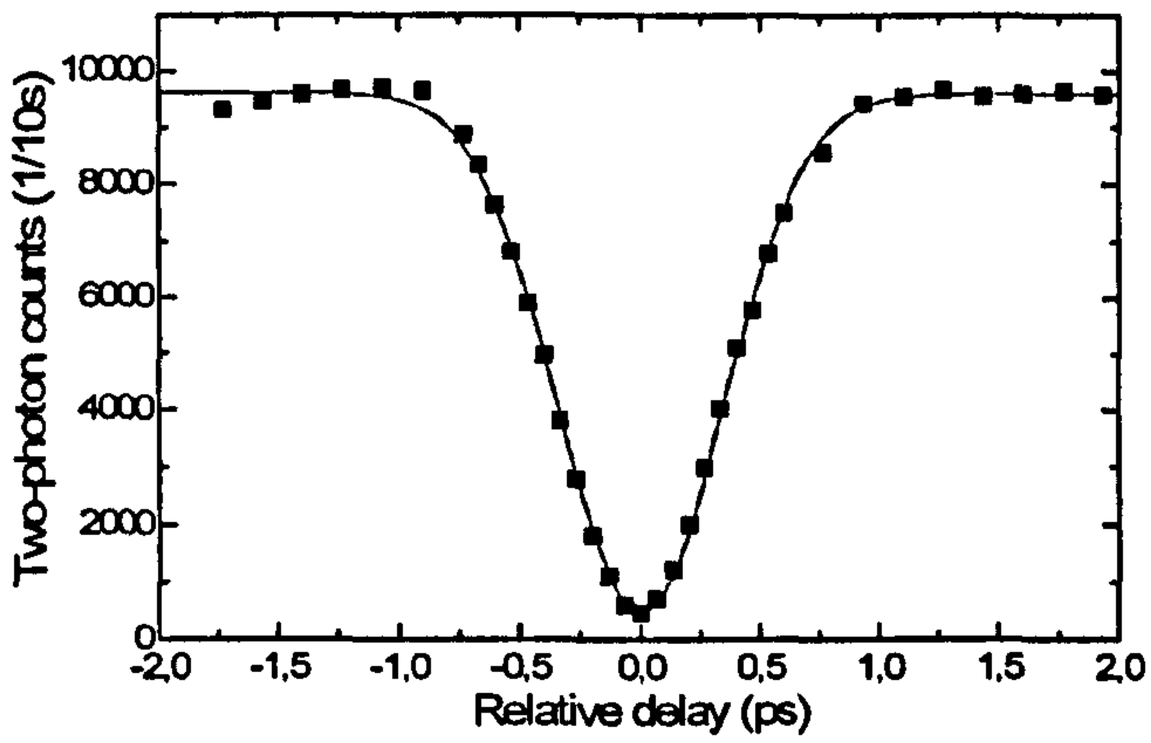

Figure 4.5: Two-photon quantum interference in integrated directional couplers. The variation of coincidental two-photon detections as function of the relative delay of the two photons launched in the coupler.

the quality of the interference and demonstrates very good quantum behavior of photons in an integrated optics architecture.

Figure 4.6B shows the measured visibility for the quantum interference for 10 couplers on a single chip with a range of design η's from 0.22 to 0.6. A best fit was performed on the experimental data points to produce the curve in the figure. The theoretical model has two fitting parameters: one to take into account mode mismatch, that provides deviation from the ideal relation of equation 4.18; the other includes the difference between the designed and real reflectivity of the coupler. The latter parameter, found to be $\delta\eta = 3.4 \pm 0.7\%$, does not introduce any limitation of the quantum interference, but gives a small translation of the curve to the right. The mode mismatch parameter is used to include the non-perfect visibility of the quantum interference. The best fit, however, does not give any information about the reason for the mode mismatch, since a mode mismatch in any degree of freedom is completely equivalent to mode mismatch in any other degree of freedom [53]. Some of the possible phenomena that can contribute to the reduced visibility are: polarization mismatch given by misalignment of PMF fibers in the array (specified to be $< 3°$); spatial mode mismatch given by weakly guided higher order modes propagating across the relatively short devices; frequency mismatch

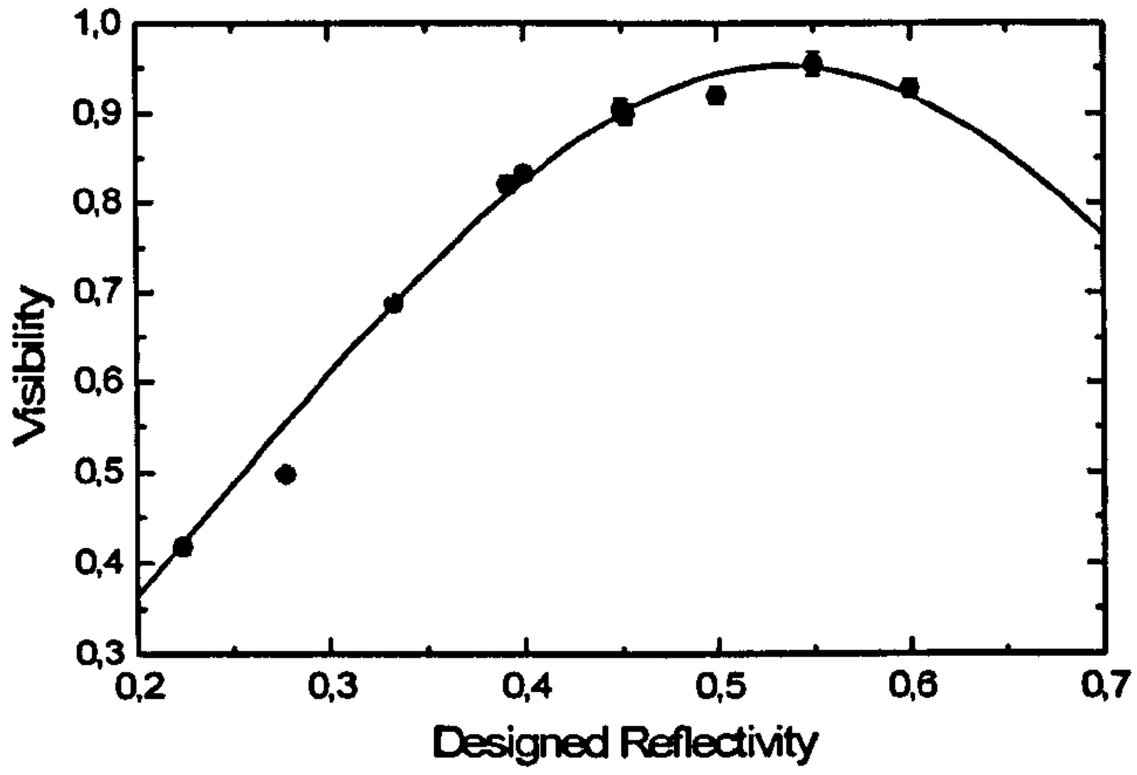

Figure 4.6: Quantum interference visibility as a function of the designed reflectivity of the coupler. Black points refer to 1/2 couplers and red dots to 1/3 coupler, as explained in the text. For both the plots error bars are smaller then data points.

given by a non-perfect filtering of the photons at the source. The reason for such a mismatch was found later in the study of the devices, and is explained in the next section. The average relative visibility $V_{av} = 1/N \sum_i^N V/V_{id}$, a measure of the global performance of the couplers, was found to be $V_{av} = 95.0 \pm 0.8\%$. These results demonstrate the high yield and excellent reproducibility of the devices for quantum optic applications.

4.4.1 Hi-visibility non-classical interference

It is key for the development of integrated quantum networks for quantum optics to understand the sources of errors in the quantum effects measured in the waveguides. A study on the phenomena that can reduce the non-classical interference visibility was conducted. As said in the previous section, polarization, mode mismatch and frequency mismatch are the most probable reasons for limited visibility. In the remainder of this section, I present the details of the analysis of the integrated device in all the above degrees of freedom.

Polarizing beam splitters were used to prove that the source was producing photons polarized along the vertical direction. I would like to point out that the

use of polarization maintaining fibres is meaningful only when the input field is polarized along one of the axis of the fibre birefringence. Otherwise the polarization inside the fibre evolves in a way difficult to predict, that can depend on the stress applied to the fibre or to the temperature. A test was performed to check that the polarizations of the photons produced from the down-conversion crystal and coupled into the fibres was preserved at the end of the fibre. A similar test was performed to check the polarization at the end of the output fibre. If there is any misalignment between the birefringence axis of the PMF, PMF arrays and chip, the photons at the output will not be polarized along the vertical direction, and probably the photons would de-cohere. The analysis results assure that this was not the case, and the limitation in the visibility of non-classical interference is not caused by polarization problems.

Mode matching problems were partially ruled out since the use of output polarization maintaining, single mode fibres performs a quantum filtering operation that ensures the indistinguishability of the photons at the detectors. If the photons are in the same spatial mode, there is no way to distinguish the previous path taken by the photons, since the information about the previous modes is washed out. If the single mode fiber is coiled with a quite tight radius, this filtering is mode efficient (even if for small radii, losses can be introduced, as shown in the previous Chapter for waveguide bends). This procedure, however, cannot solve all the limitations coming from mismatch of the modes if these come from mode mixing inside the coupler.

The limitation in non-classical visibility was solved through a deep analysis of the photon source. It was discovered from colleagues working on the same source that the photons were not degenerate regarding the spectral properties. The wavelength distribution of the down-converted photons depend on the combination of the position of the fibres in the down-conversion cone (since the wavelength of the photons is a function of the opening angle via the phase matching condition) and the spectrum of the filters used in front of each fibre. Using a spectrometer with a sensitivity good enough to detect few photons, it was possible to check the

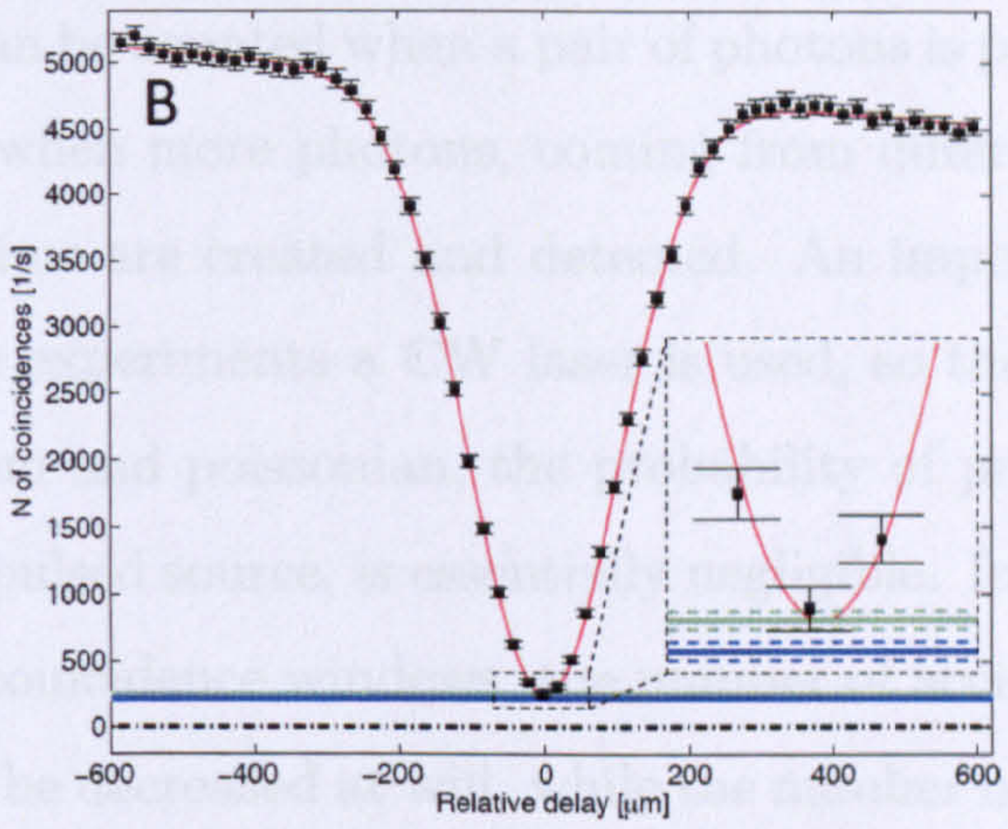

Figure 4.7: Two-photon quantum interference in integrated directional couplers. The blue line is the measured rate of accidental counts, and the green shows the count rate expected at the centre of the dip for the measured reflectivity $\eta = 0.5267 \pm 0.0004$.

final spectrum, and tweak the tilting of the filters and the position of the fibres to ensure the same spectral distribution for the down-converted photons.

The result of such an analysis is synthesized in the non-classical interference experiment shown in figure 4.7. This dip is obtained with exactly the same device studied in the previous section. The raw visibility is $V_r = 94.9 \pm 0.4$, so it does not look better than the results obtained in the previous experiments. However, a correction is necessary to obtain the true visibility that is possible to obtain with the integrated directional coupler.

At the bottom of the non-classical interference dip, the number of coincidental detections depends on the photons that exit the different outputs of the coupler as a consequence of a non-perfect interference, and the accidental counts registered by the counting electronics. The electronic circuit that counts the coincidental events of single photons is composed by a Stanford Lab SR400 instrument. When a single photon is detected at output A, the same electronic pulse opens a window of 5 ns for channel B. If an electronic pulse coming from the single photon detector is registered in this 5 ns window, a coincidental event is counted. It is obvious that

coincidental events can be counted when a pair of photons is produced and detected by the detectors, or when more photons, coming from different pairs but created closer than 5 ns in time are created and detected. An important point to notice here is that for these experiments a CW laser is used, so the time distribution of the photons is random and poissonian, the probability of producing higher order terms, contrary to a pulsed source, is essentially negligible. In principle, for perfect detectors and short coincidence windows, the number of accidental counts coming from a CW laser can be decreased at will, while the number of multi-photon events coming from a pulsed source is limited by equation 2.14. The number of accidental counts is proportional to the number of single photon counts in each channel and the length of the window time.

In reality the number of accidental counts is not easily decreased to zero because the coincidence window cannot be decreased too much. Apart from the electronic problem of having fast processing, the biggest limitation is due to the time jitter in the response of the single photon detectors. Silicon single photon detectors have time jitters of the order of hundreds of picoseconds, so the coincidental window cannot be shorter than this interval, otherwise too many counts would be lost. A solution to this problem is using faster detectors, like superconducting ones.

In figure 4.7 the blue line represents the number of accidental counts coming from the CW source. The value is measured experimentally by changing the delay between channel A and B of the electronic system, so that the window for channel B is opened when the photon belonging to the pair that is detected in channel A is not present. In this way, coincidental events come just from photons generated from different down-conversion processes. This value is exactly the number of accidental counts we want to remove from the measure of the non-classical interference experiment.

We have also to remember that the visibility of the non-classical interference cannot be unity because the reflectivity of the directional coupler is not exactly $\eta = 0.5$, as expected from equation 4.18. The reflectivity of the directional coupler was measured to be $\eta = 0.5267 \pm 0.0004$. The green line shown in figure 4.7

represents the minimum number of coincidental events at the bottom of the dip for this value of η and taking into account the accidental counts coming from the CW source. It is possible to note that the bottom of the dip is, within error, at the same level as the green line. The quantum interference visibility taking this rate into account is then $V_{meas} = 99.5 \pm 0.4\%$ which corresponds to a relative visibility of $V_{rel} = 100.1 \pm 0.4\%$. The visibility of the non-classical interference is unitary within error-bars, and we can consider the interference to be essentially perfect, regarding the integrated circuit alone.

This result is important because it demonstrate that there is no limitation, from this point of view, to implement quantum operations in an integrated optics architecture.

4.5 Multi-mode couplers

The MMI couplers with the design described in the previous chapter were measured in the same way as the directional coupler. The first measurement was performed with the same source that allowed the achievement of non-classical interference with visibilities of around $V = 95\%$. It is expected that the MMI couplers would reach the same visibility, if the multi-mode section does not introduce a process that limits the indistinguishability of the photons.

The first measurements, for different devices containing MMI couplers with and without tapering in the input/output waveguides, gave non-classical interference effects with visibility around $V = 85\%$. The reduction in visibility cannot be explained considering the values of the splitting ratio. Using the method described in Section 4.2 it was possible to calculate the maximum visibility obtainable from the splitting properties. The value was found to be close to perfect, since, with some approximation, it was reconstructed a splitting ratio of around $\eta = 0.52\%$ using equation 4.15. A typical non-classical interference experiment conducted with MMI couplers is shown in figure 4.8.

A similar analysis to the one performed to understand the limits of the direc-

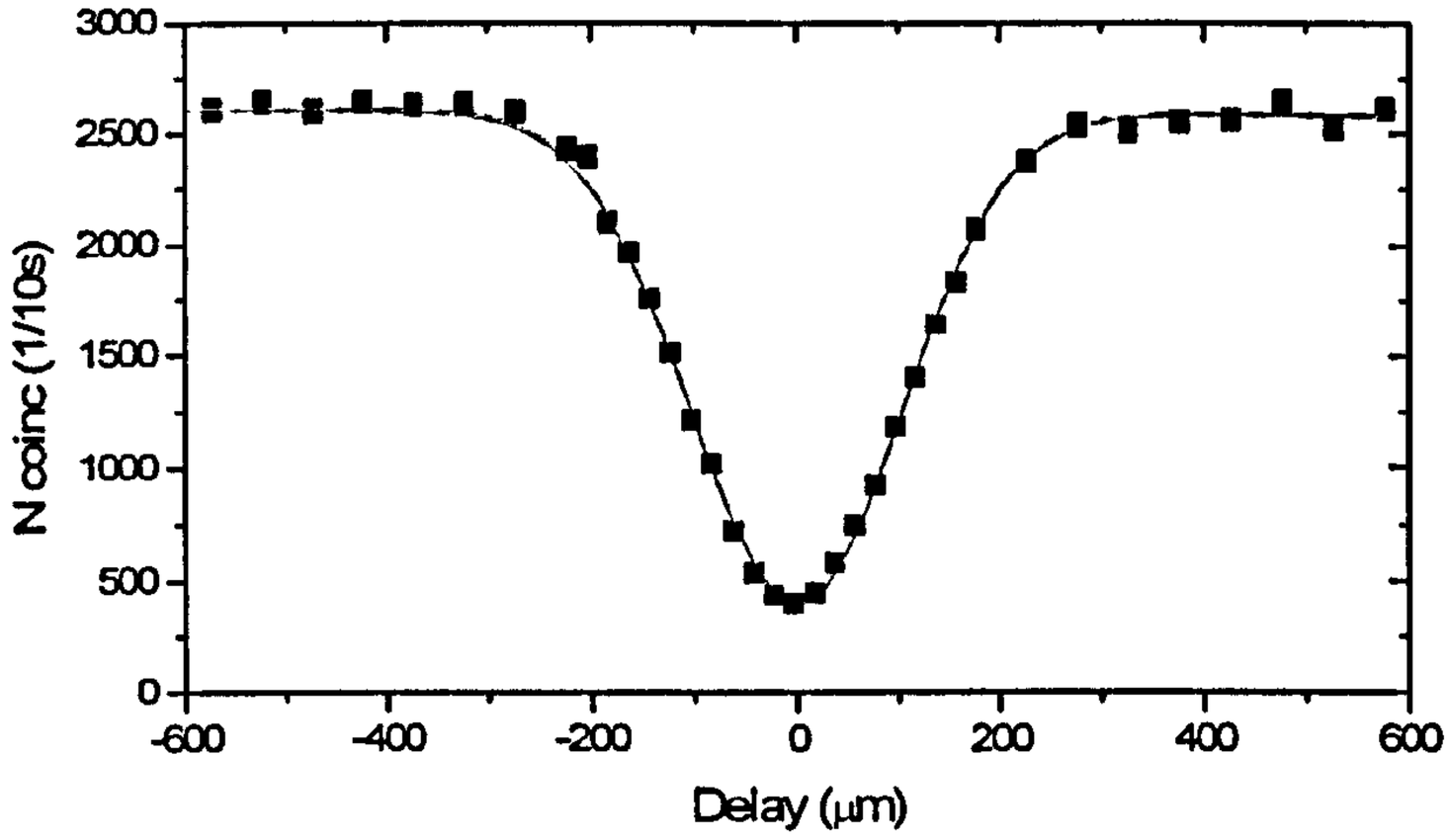

Figure 4.8: Two-photon quantum interference in integrated MMI coupler. The interference filters used in the source have a FWHM bandwidth of $2nm$.

tional couplers was performed for the MMI structure. In this case, however, the starting point for the analysis is that the source of photons is capable of producing $V = 95\%$ non-classical dips. The decrease in visibility form this value has to be caused by the properties of the chip.

The obvious consideration is that the multi-mode section could introduce some coupling process between guided modes that are orthogonal (and then distinguishable). For example, if part of the higher order modes are preserved inside the output waveguides, and the MMI section is not terminated exactly at the point of self-imaging, mode mismatch can be present. To test this hypothesis, coils of single mode fibres are added at the output of the chip to filter out potential higher order modes as much as possible. The coils would act as a projection on a single guided mode for each output fibre, since the propagation losses of higher order modes are higher than the ones for the fundamental mode. The propagation would filter out the higher order modes, and erase all the information about the mode mismatch. Experiments with coils of fibres were performed, obtaining exactly the same results as the previous case. The only difference was that a small loss was appreciated, this confirms that the single mode fibres are coiled with a radius of curvature that introduces losses also for the fundamental mode (as expected from

the analysis of losses in bend structures of Section 3.2.2).

A second hypothesis is that the multi-mode section, and the abrupt passage from the single mode section to the multi-mode one, can introduce coupling between the guided TE and TM modes, so to obtain a small polarization mixing of the light entering the sample. If this would be the case, it is expected to notice a rotation of the polarization of the photons at the end of the integrated device. Remembering that the setup is composed of polarization maintaining fibres both for the input and output, it is possible to analyze the polarization state of light at the end of the output fibre, and obtain information about the propagation into the chip. A polarization analysis was performed using a simple PBS cube, to project the light on the horizontal polarization. The analysis of the outcoming light, and a non-classical interference experiment in these conditions, confirmed that no polarization coupling is present in the multi-mode section.

The last degree of freedom that can reduce the indistinguishability between photons in the coupler is the time variable. At first it would be noted that the temporal degree of freedom is used extensively in the non-classical interference experiment, since the HOM dip is measure varying the arrival time of the photons in the coupler structure. The fine tuning of the delay between the photons is possible, and this should prevent timing problems. At the same time, an analysis of the multi-mode structure suggest a different problem that can be present in this waveguide section. Given the bulky nature of the MMI section, it would be possible that the path taken by one photon to arrive at the output of the coupler is different in the case of transmission or reflection. If this is the case, the arrival time of the photons is different for the two processes of both photons being reflected or both transmitted, so that the two cases can be distinguished, and the non-classical interference effect is destroyed.

The above explanation is just a pictorial representation of the light propagating in the device using ray optics, but can give an idea of what is happening in the device. This hypothesis can be developed in the full electromagnetical treatment of propagation. The incoming photons, arriving in the MMI section, are propagating

in a superposition of different spatial modes. Each mode has its own effective index and propagation characteristic. This means that the propagation speed for each mode is different. In some sense, the arrival time of the photons at the end of the multi-mode section suffers from a jitter caused by the decomposition of light propagation in many modes with different speed. If the MMI section is long enough, the difference in speed is sufficient to spread the photon enough to destroy the temporal overlap between the different components. The effect is to suppress the coherence of the photon. For shorter MMI sections than this extreme case, the photons partially decohere and the non-classical interference is reduced.

The experimental test to check this hypothesis is to increase the coherence time of the photons that enter the device. In this case, the same amount of time jitter would be small compared to the width of the non-classical interference dip, and good indistinguishability can be achieved. The experiment was performed placing a single interference filter with a FWHM bandwidth of $0.5nm$ after the MMI coupler. This corresponds to an increase of the coherence time of the photons of 4 times. Figure 4.9 shows the results of the experiment. In this case, the non-classical interference visibility is $V = 93 \pm 1\%$. This value confirms the idea that the multi-mode section of the coupler introduces a time difference in the possible paths taken by the photons.

Even with the increase of of the coherence time of the photons, the visibility of the non-classical interference dip is still not as high as in the case of directional coupler structures. Additional studies have to be performed to understand the sources of this phenomenon. Fabricating new structures with multi-mode section of different dimensions will help to study the effect of time jitter in the MMI structures used for quantum information applications. The study of N×N MMI couplers will also be interesting in the context of generalized non-classical interference effects [54–56].

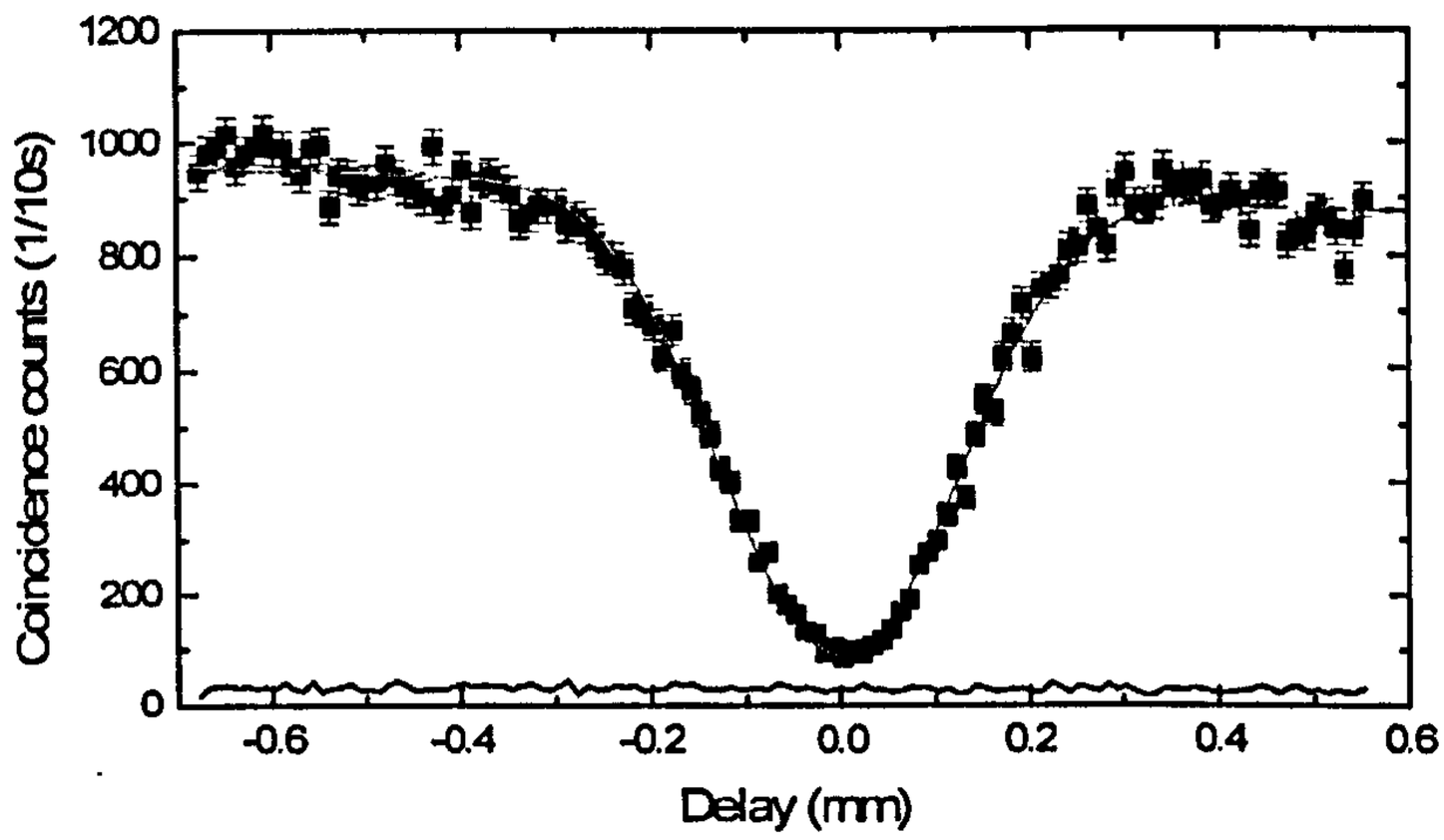

Figure 4.9: Two-photon quantum interference in integrated MMI coupler. The blue line represents the number of accidental counts. The interference filters used in the source have a FWHM bandwidth of $0.5nm$.

Chapter 5

Directly written waveguides

In this chapter I will present an alternative technology to obtain integrated optic circuits for quantum information applications. The technology is based on waveguides in glass, fabricated using the direct-write ultrafast laser technique. The waveguides were designed and fabricated by the group of M. J. Withford at MacQuarie University, Sydney, as part of a collaboration work with Bristol University. In the following, I will describe the fabrication process and the properties of direct-write waveguides, since the field is relatively young and the group of M. J. Withford is one of the few groups that can fabricate the optical networks for 800nm applications. I will then describe the results obtained from Bristol regarding the quantum optical properties of the waveguides.

This Chapter is based on the results published in the following article:

G. D. Marshall, A. Politi, J. C. F. Matthews, P. Dekker, M. Ams, M. J. Withford, J. L. O'Brien, Laser written waveguide photonic quantum circuits, *Optics Express*, **17**, 15, 12546-12554, (2009).

5.1 Properties and fabrication of Directly written waveguides

Ultrafast lasers are a powerful tool not only for machining [57], but also for optical modification of materials [58]. In particular, the direct-write femtosecond laser technique for creating optical waveguides in dielectric media [59] is an alternative waveguide manufacturing technique that allows the production of low-volume complex three-dimensional optical circuits. This process has been applied to a wide range of passive and active media to create integrated devices such as microfluidic sensors [60], waveguide-Bragg gratings [61] and miniature lasers [62]. Because there is no lithography step in this procedure, it enables a waveguide circuit to be taken rapidly from a concept to a commissioned device. However, as with all waveguide fabrication processes, the finished devices are subject to manufacturing imperfections and there has been no previous demonstration that the use of the laser-writing technique can produce waveguides that can operate on single-photons without deleterious effects on the phase, spatial mode and polarization.

In conventional lithographically fabricated integrated optical devices, light is guided in waveguides consisting of a core and a slightly lower refractive-index cladding or buffer layers. In the commonly used flame hydrolysis deposition fabrication method, these structures are lithographically described on top of a semiconductor wafer, as for the silica-on-silicon samples described in the previous chapters. However, this approach requires to work within the constrains of lithography: the devices must necessarily be 2-dimensional, created as a large assortment of devices (since the most cost efficient use of a fabrication run is to use all the available area on a wafer) and the physical parameters of the waveguide devices must be very well understood and modeled before manufacture since the turn-around time for a single manufacturing process is lengthy.

Similar waveguide conditions and directional coupler structures to the ones described in the previous Chapter can be obtained with the directly written technique, where the waveguide core is formed by local modification of the microscopic

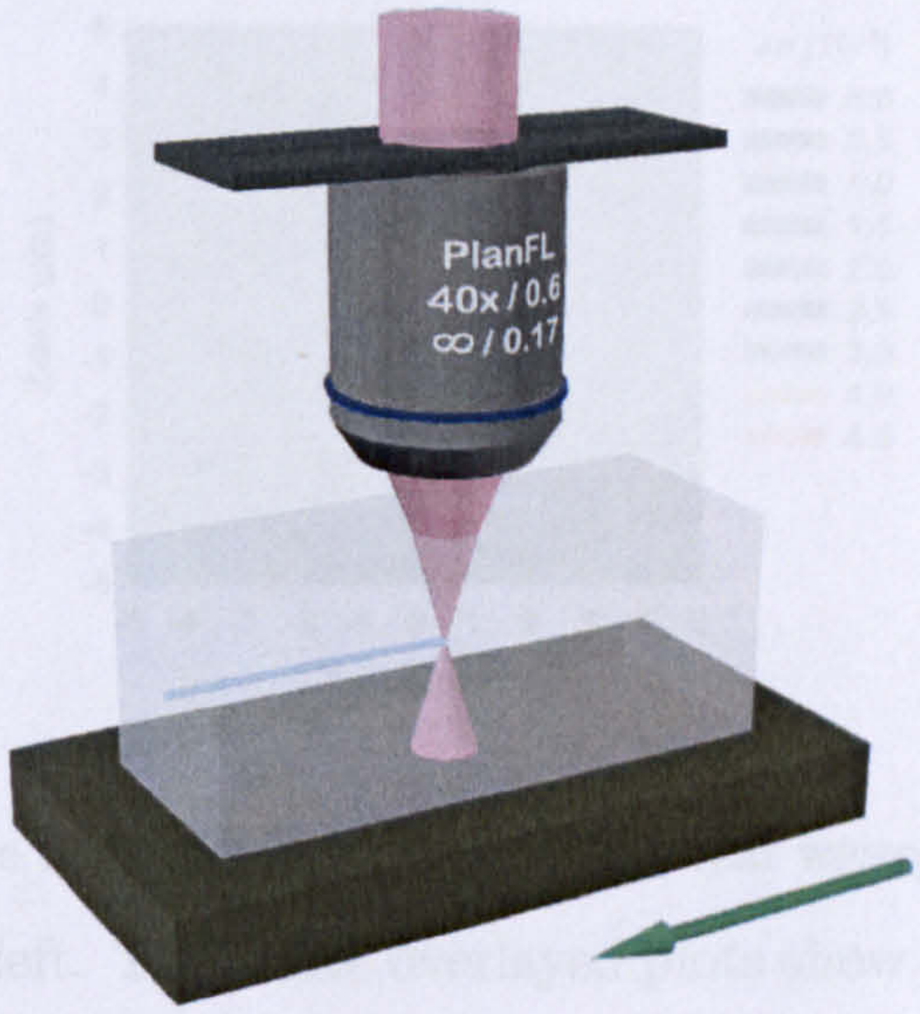

Figure 5.1: A schematic of the femtosecond-laser direct-write process.

structure of silica [63, 64] or other materials. In this case, unlike the lithographic approach, direct-write circuits can be straightforwardly written in 3D.

The group of M. J. Withford fabricated and classically characterized two chips with a number of direct-write quantum circuits (DWQCs) composed of 2×2 directional couplers (figure 5.3) and Mach-Zehnder interferometers. The circuits were written inside high purity fused silica using a tightly focused 1 kHz repetition rate, 800 nm, 120 fs laser and motion control system [65, 66]. The writing laser beam was circularly polarized and passed through a 520 μm slit before being focused 170 μm below the surface of the glass using a 40× 0.6 numerical aperture microscope objective that was corrected for spherical aberrations at this depth (figure 5.1). The writing process created approximately Gaussian profile waveguides which were characterized using a near-field refractive index profilometer (from Rinck Elektronik) and a magnifying beam profiler. The measured refractive index profile of a typical waveguide is displayed in figure 5.2 and shows a peak refractive index change of 4.55×10^{-3}, an average $1/e^2$ width of 5.5 μm and a x/z width ratio of 0.93. At their design wavelength of 806 nm these waveguides supported a single transverse mode with orthogonal (intensity) $1/e^2$ widths of 6.1 μm × 6.1 μm (the

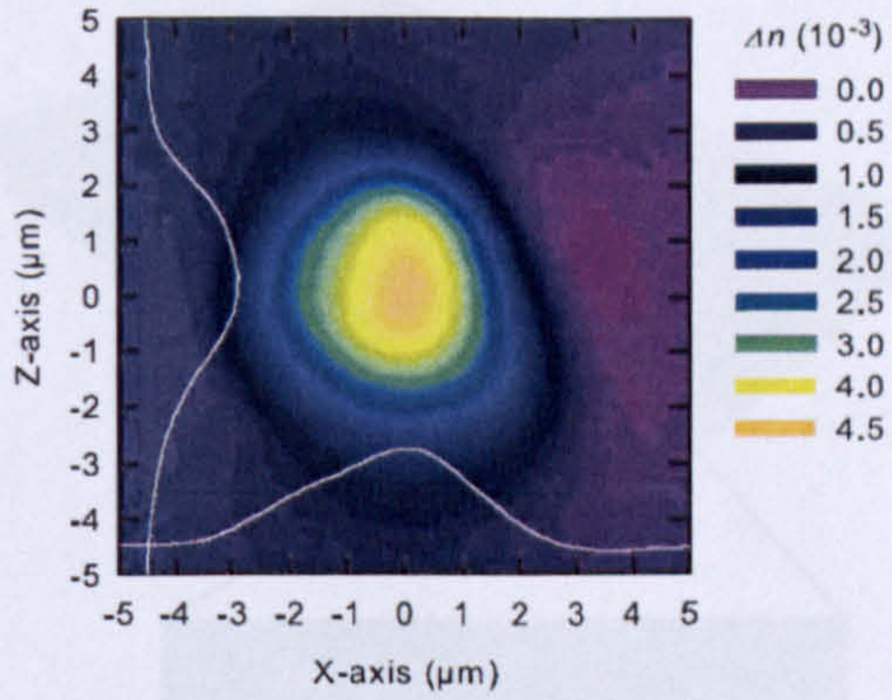

Figure 5.2: A refractive index (RI) profile of a typical waveguide, the writing laser was incident from the left. The white overlayed plots show the cross section of the RI profile at the peak. The distortion to the measured x-axis RI profile to the left of the peak is an artifact of the measurement method.

small amount of measured RI shape-asymmetry not being evident in the guided mode). The design of the directional couplers was functionally identical except for the length of the central interaction region that was varied from 400 to 2000 μm to achieve different coupling ratios. The curved regions of the waveguides were of raised-sine form and connected the input and output waveguide pitch of 250 μm down to the closely spaced evanescent coupling region of the devices. The Mach-Zehnder interferometers are composed by two 50:50 directional couplers separated by identical 1500 μm long arms. The purpose of these devices was to test the stability of both the completed waveguide circuits and the laser writing system (which was required to remain stable for several hours, corresponding to the time required for the fabrication of the designed structures).

5.2 Quantum optical properties of Directly written waveguides

The quantum circuits were studied using photons obtained from the CW spontaneous parametric down conversion source as described in the previous Chapter.

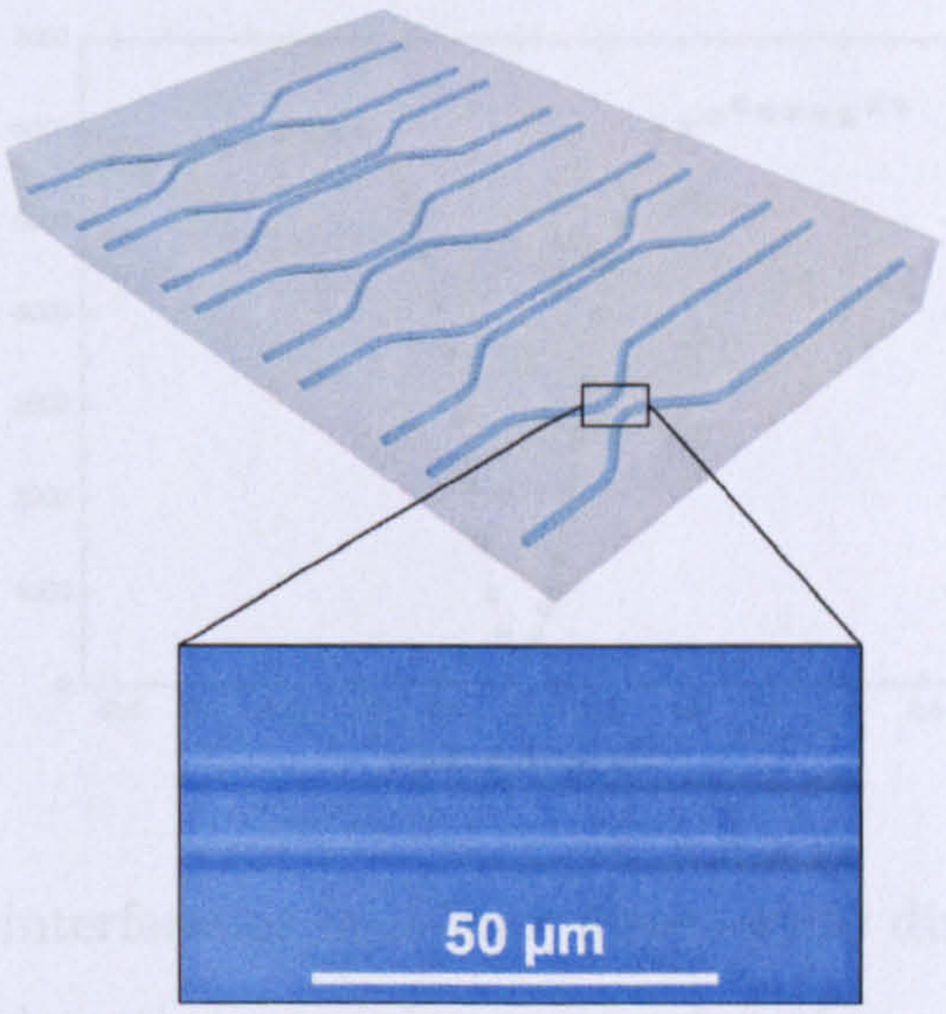

Figure 5.3: A schematic of an array of directional couplers fabricated by *fs* direct writing in a single fused silica chip and an optical micro-graph showing the central coupling region where the waveguides are separated by 10 μm.

Also for the direct-write circuits index matching oil was used between the fibres and the device under test to reduce Fresnel reflections that contribute to coupling losses. The circuit devices had typical transmission efficiencies of 50%, including coupling and propagation losses.

To demonstrate the suitability of the direct-write laser technique for creating optical quantum logic systems, devices were fabricated containing arrays of 2×2 evanescent couplers. Figure 5.3 shows the waveguide testing layout. Mach-Zehnder interferometers were included in the fabrication process, to test the stability of the optical phases in the integrated devices.

5.2.1 Two-photon non-classical interference

Figure 5.4 shows the raw data for a HOM dip in a coupler with $\eta = 0.5128 \pm 0.0007$ (maximum theoretical visibility $V_{ideal} = 0.9987 \pm 0.0001$). The measured visibility of the non-classical interference is 0.958 ± 0.005. Figure 5.5 shows the measured visibility V as a function of the equivalent reflectivity η for eight couplers on

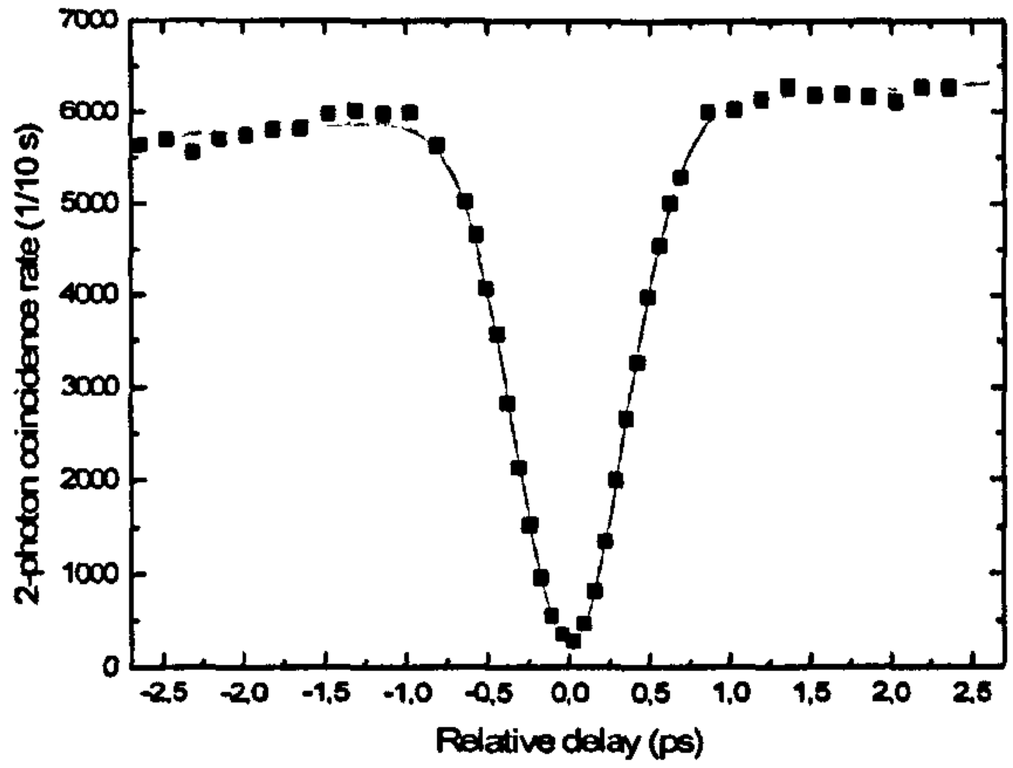

Figure 5.4: Quantum interference in a laser direct-write directional coupler. The number of coincident detections are shown as a function of the arrival delay between the two interfering photons. Error bars from Poissonian statistics are smaller than the point size and the fit is a Gaussian plus linear.

the two chips. The curve is a fit of equation 4.18, modified to include a single parameter to account for mode mismatch [53]. The average relative visibility for these eight couplers is $V_{av} = 0.952 \pm 0.005$, demonstrating high performance across all couplers on both chips.

The values above have to be compared with the non-classical interference visibility of $V = 95\%$ obtained in the silica directional coupler before the improvement of the indistinguishability of the photons. This suggests that the mode mismatch that caused the limitation in the non-classical interference is to be found in the spectral properties of the incident photons. A more accurate study of the DWQC with the source capable of obtaining near-perfect HOM dips has to be conducted in the future to confirm the expected high quality of the samples.

Using single-photons as a convenient source with which to measure the effective reflectivity of a Mach-Zehnder interferometer we found that the reflectivity of the device was $\eta_{MZ} = 0.960 \pm 0.001$ indicating that the *written* phase shift in the interferometer is very close to zero (of the order 10 nm). In studying the performance of the interferometer over an extended period of time and varying ambient

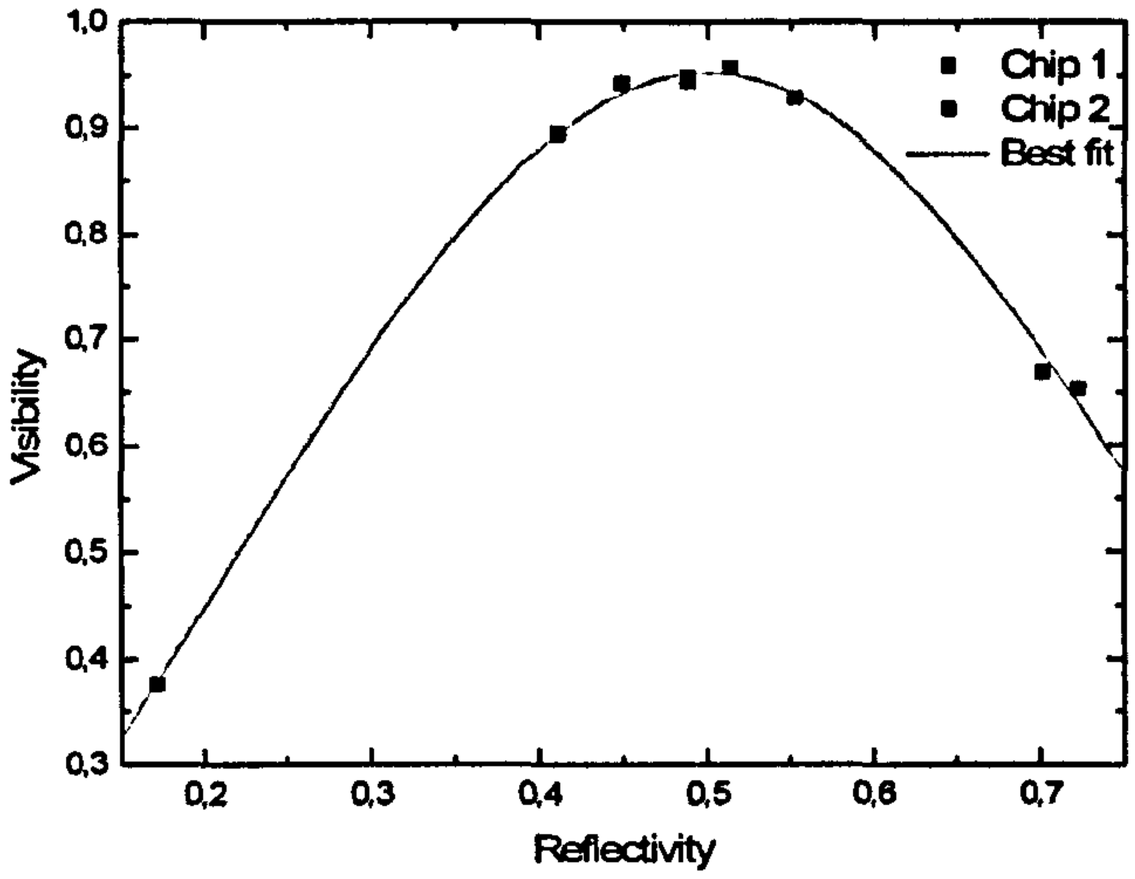

Figure 5.5: Quantum interference visibility as a function of coupling ratio η. Error bars are determined from fits such as those in figure 5.4 and are comparable to the point size.

temperature conditions (the stability of the temperature in the laboratory for this experiment can be estimated as $\pm 3°C$), no variation in η_{MZ} was observed. This indicates that the phase shift in the interferometer remained stable throughout changing environmental conditions that would detrimentally affect an equivalent bulk-optical Mach-Zehnder interferometer.

5.2.2 Multi-photon non-classical interference

Many important quantum circuits involve not just single and pair photon interference, but multi-photon quantum interference. In particular, interference of three photons at a beam-splitter has many important applications—including quantum logic gates [13, 67], quantum metrology [68], photon number filters [69, 70], entanglement filters [71, 72], and biphoton qutrit unitaries [73]—and is thus a key enabling capability. When two photons are input into A and one in B, an ideal $\eta = 2/3$ reflectivity coupler will generate the three-photon entangled state:

$$|21\rangle_{AB} \rightarrow \frac{2}{3}|30\rangle_{CD} - \frac{\sqrt{3}}{3}|12\rangle_{CD} - \frac{\sqrt{2}}{3}|03\rangle_{CD}, \tag{5.1}$$

where quantum interference results in no $|21\rangle_{CD}$ term. An analogue of the HOM dip can therefore be observed by measuring the rate of detecting two photons in C and one in D as a function of the delay time between the photon in B and the two photons in A [69].

To observe a $|21\rangle_{CD}$ HOM dip, as described by equation 5.1, a pulsed laser system was used to generate four photons in 2 modes at 780 nm, where the DWQCs are also single moded. The output of a ~150 fs, 80 MHz repetition rate 780 nm Ti:Sapphire laser was frequency doubled to 390 nm and then down converted into pairs of 780 nm photons in a type-I phase matched BiBO crystal. The photon pairs passed through 3 nm bandpass interference filters before being coupled into two polarization maintaining single mode optical fibres. By using a fused PMF splitter and single photon APD, it is possible to probabilistically prepare the $|1\rangle_B$ state at input B. Using a SMF fibre coupler, it is possible to probabilistically detect two photons at output C. The scheme to produce and detect the desired states is shown in figure 5.6. The low probability of preparing the required 4-photon state at the source and the $\frac{1}{4}$ success rate of experimental setup significantly reduced the measurement count rate from that of the 2-photon experiment. The three-

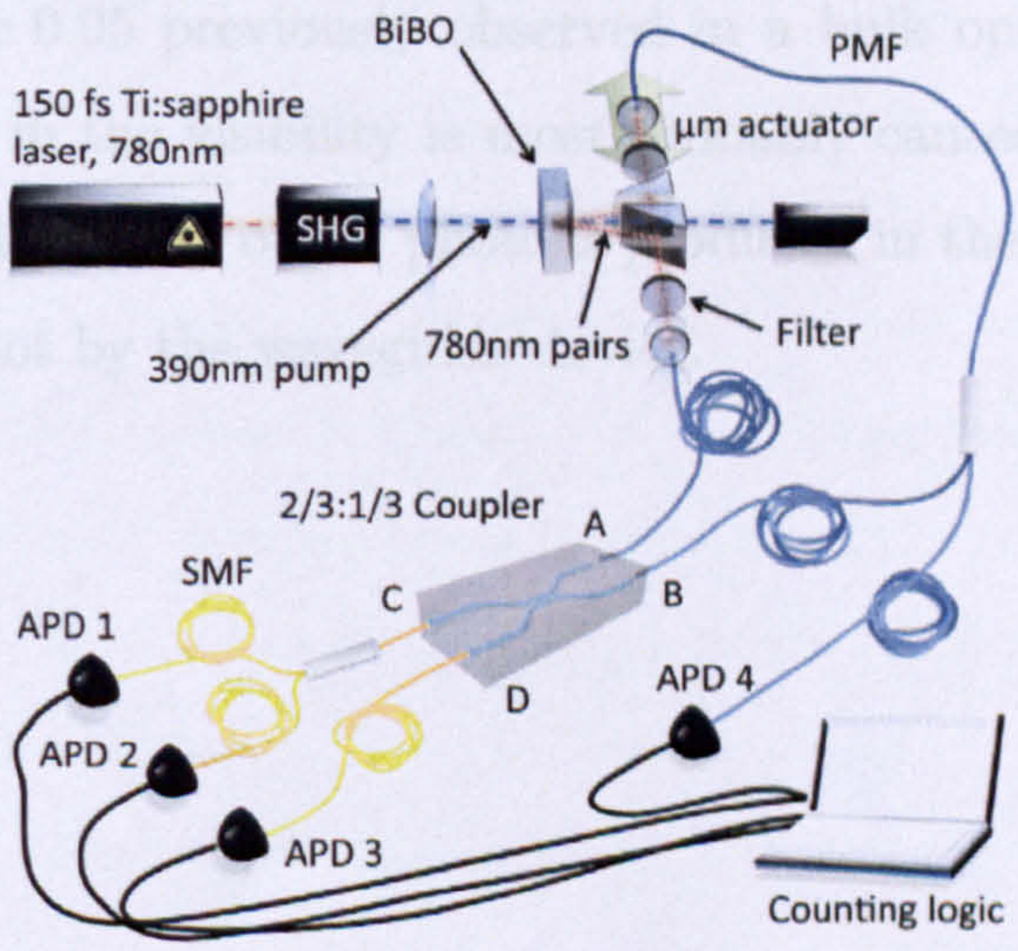

Figure 5.6: Schematic representation of the experimental setup to measure the 3-photon generalized non-classical interference dip.

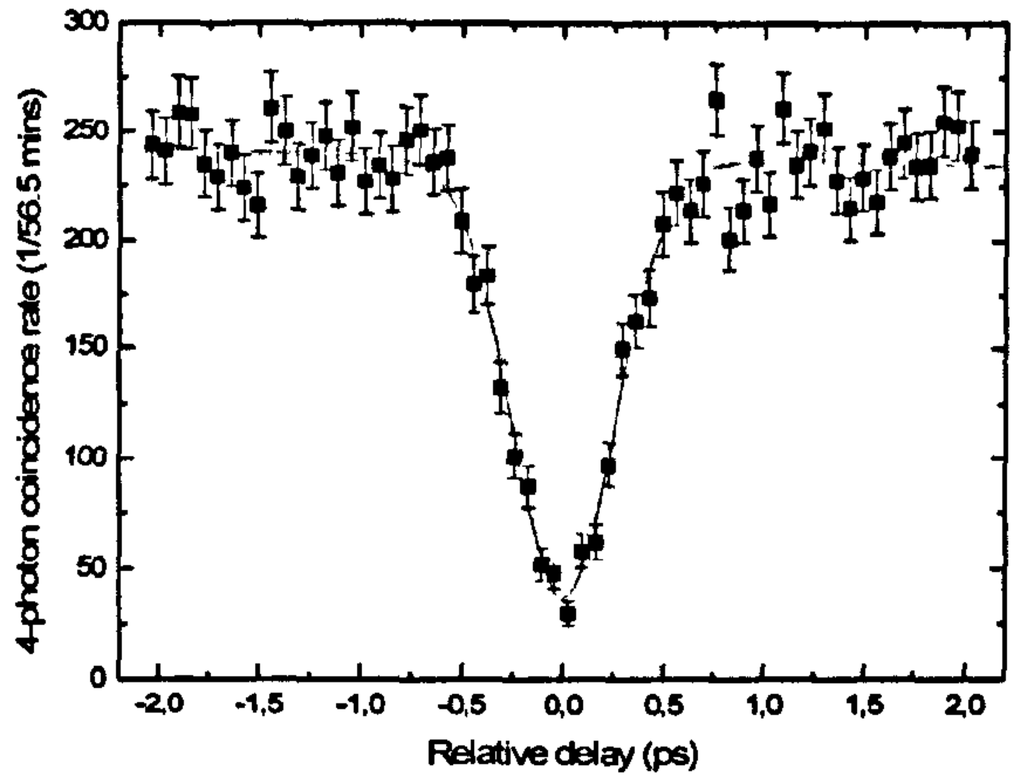

Figure 5.7: Generalized HOM dip for three photons, the number of coincident detections are shown as a function of the arrival delay between the two interfering photons.

photon interference measurements performed with this setup required ~60 hours to be completed. For this reason, they can be seen as a test of the stability of the circuit.

Figure 5.7 shows the generalized HOM dip observed in a $\eta = 0.659$ reflectivity DWQC coupler. The visibility of this dip is $V = 0.84 \pm 0.03$, which surpasses the value of $V = 0.78 \pm 0.05$ previously observed in a bulk optical implementation [69]. The limitation in the visibility is most probably caused by a small amount of temporal distinguishability of the photons produced in the source, nominally in the $|2\rangle_A$ state, and not by the waveguide device.

Chapter 6

Manipulation of Photons on a chip

In this Chapter, I will present the results obtained from samples with integrated phase shifting capabilities. After introducing the use of such devices to control the state of single qubits in the chip, and how it is possible to implement arbitrary single qubit operations, experimental results are presented for Mach-Zehender interferometers and single photons. The Chapter will continue showing how phase control and directional couplers can be used to create and manipulate entanglement in a chip. In this case, two- and four-photon experiments will be shown. These demonstrations are important not just for quantum information applications, but particularly for quantum metrology experiments. The last section is based on the use of integrated interferometers to implement reconfigurable circuits, that can be used to obtain multi-mode, multi-photon optical networks.

This Chapter is based on the results published in the following articles:

A. Politi, J. C. F. Matthews, M. G. Thompson, J. L. O'Brien, Integrated Quantum Photonics, *Journal of Selected Topics in Quantum Electronics*, **15**, 6, 1673-1684, (2009);

J. C. F. Matthews, A. Politi, A. Stefanov, J. L. O'Brien, Manipulation of multiphoton entanglement in waveguide quantum circuits, *Nature Photonics*, **3**, 346 - 350 (2009).

6.1 Experimental details

The photons used to obtain the results described in this Chapter were produced using a pulsed laser system, as shown schematically in figure 6.1. The output of a ~150 fs, 80 MHz repetition rate 780 nm Ti:Sapphire laser was frequency doubled to 390 nm using a BiBO crystal. The output of the crystal passed through four dichroic mirrors to divide the up-converted component from the 780 nm residue. The 390 nm pulses were used to create down-conversion pairs of 780 nm photons in a type-I phase matched BiBO crystal. The photon pairs passed through 3 nm bandpass interference filters before being coupled into two polarization maintaining single mode optical fibres.

Both two- and four-photon experiments were conducted with the same source. The desired state was created setting the power of the mode-locked laser at the appropriate value to minimize higher order terms emission, while obtaining good down-conversion efficiency.

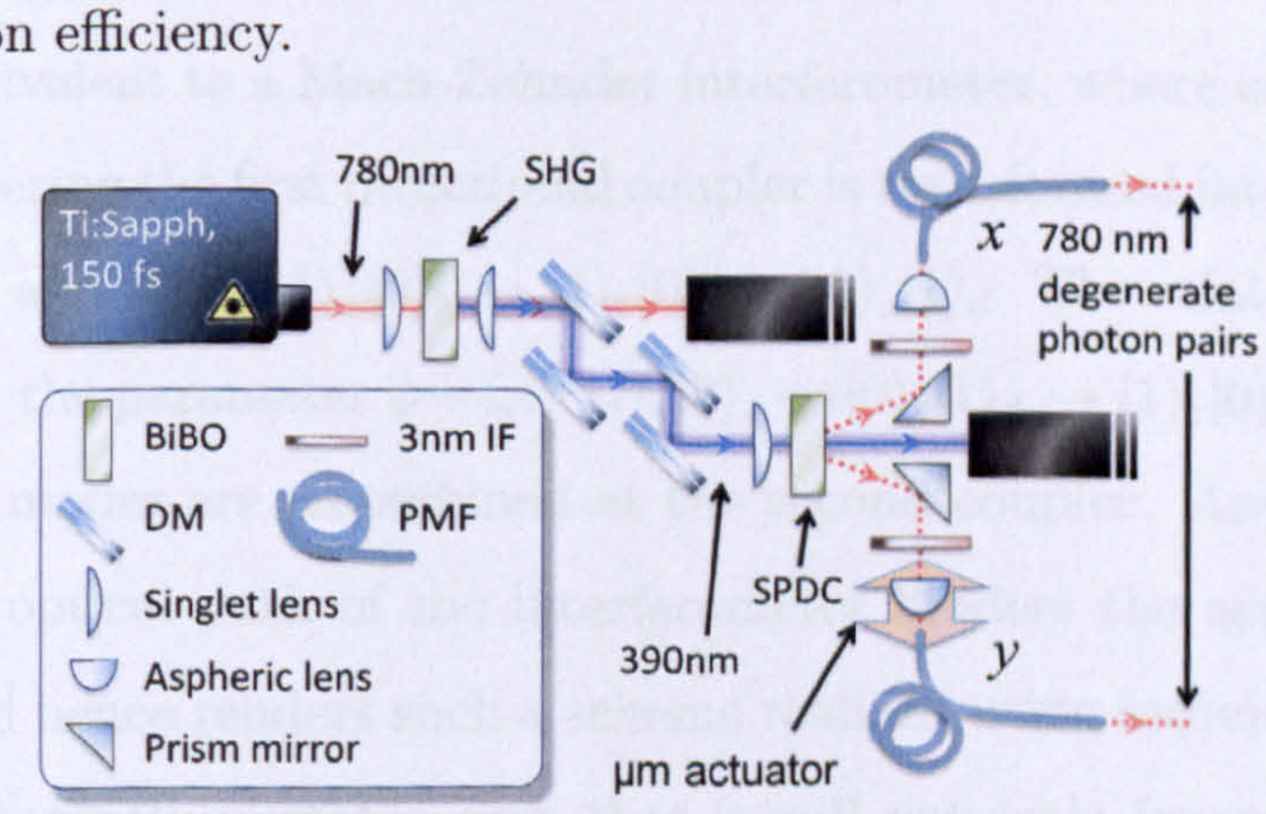

Figure 6.1: Schematic of the single photon source used to perform all the multi-photon experiments presented in this Chapter.

6.2 Single qubit operations with photons

Integrated arbitrary qubit preparation is a key capability for both the development and characterization of integrated photonic quantum devices. Mathematically,

it is possible to map arbitrarily from the logical qubit $|0\rangle$ to the general state $\cos\phi/2\,|0\rangle + e^{-i\theta}\sin\phi/2\,|1\rangle$ by applying the operation $U_{prep} = e^{i\theta\sigma z/2}He^{i\phi\sigma z/2}H$ and controlling the two real free parameters $\theta \in [0, 2\pi)$ and $\phi \in [0, \pi)$, where H is the Hadamard operation and where σ_Z is the third Pauli operator. The unitary nature of quantum mechanics therefore allows U_{prep} to map from the computational basis $\{|0\rangle, |1\rangle\}$ to any other given basis, while the inverse operation $U^{\dagger}_{prep}$ provides the reverse mechanism allowing the projective measurement of single qubit states in arbitrary bases and hence full process tomography of quantum circuits [74].

For polarization encoded photons, the operation U_{prep} is realized in bulk optics by using, for example, combinations of commercially available quarter- and half-waveplates. For dual rail-encoding, the equivalent implementation requires one 50% reflective non-polarizing beam splitter for each Hadamard operation H and accurate control over the relative optical phase between the two optical paths to realize each phase gate $e^{i\phi\sigma_z}$. The accurate realization of the $He^{i\phi\sigma z/2}H$ term is therefore locally equivalent to a Mach-Zehnder interferometer, where each optical mode of the input entering the first directional coupler is transformed into a superposition across modes c and d: *eg* $|1\rangle_a|0\rangle_b \rightarrow |1\rangle_c|0\rangle_d + i|0\rangle_c|1\rangle_d$. The relative optical phase is controlled by the parameter ϕ—*i.e.* $|1\rangle_c|0\rangle_d + i|0\rangle_c|1\rangle_d \rightarrow |1\rangle_c|0\rangle_d + e^{i\phi}i|0\rangle_c|1\rangle_d$—before the two modes are recombined at the second coupler. Any small variation in the relative optical path of the interferometer hinders the accurate control of the phase ϕ and hence renders such a scheme realized using individual bulk optical components inherently unstable such that it will not scale favorably for incorporation into larger and more complicated experiments and devices. The monolithic nature of integrated waveguide optics using 50% splitting ratio directional couplers solves the problem of constructing completely stable Mach-Zehnder interferometers (figure 6.2), and local control of the phase between the waveguides inside the interferometer enable accurate control over the output state. It is interesting to note that the mathematical description of quibit rotations can be generalized to states that live in bigger Hilbert spaces. If we use the path encoding to describe an N dimensional state over N waveguides, it is possible to use several Mach-Zehnder

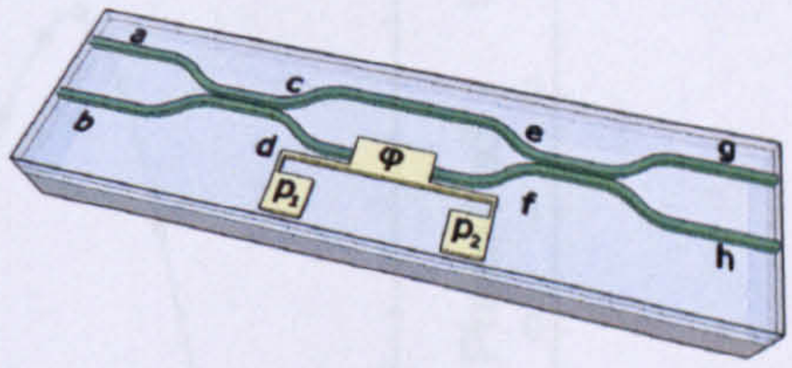

Figure 6.2: Schematic of an integrated Mach-Zehnder interferometer with a variable phase shifter realized using a resistive heater.

interferometers and additional phase shifters to realize any arbitrary N-mode unitary operator [75].

6.2.1 Integrated device and calibration

A metallic layer deposited on the top of the silica chip is used to provide resistive heaters, metallic connections and contacts to physically control the phase inside the interferometer. When a voltage is applied across the contact pads p_1 and p_2, current flows through R and generates heat which dissipates into the device and locally raises the temperature T of the waveguide structure directly beneath R. A change in the temperature of the waveguide provides a temperature change in its core and cladding. To first approximation, the change in refractive index n of silica is given by [47] $dn/dT = 10^{-5}/\mathrm{K}$, independently of the compositional variation of core and cladding. This induces a change in mode group index of the light confined in the corresponding waveguide section directly beneath R, and therefore introduces a phase difference ϕ with respect to the unperturbed waveguide. The heat generated inside the resistive elements R dissipates through the depth of the structure to the silicon substrate which acts as a heat sink. The devices were designed to enable a continuously variable phase shift and, thanks to the monolithic nature of the device, no strict global temperature control of the chip is required.

The voltage-controlled phase inside the interferometer circuit is defined by a nonlinear relation $\phi(V)$ that depends on the characteristics of each chips. For this

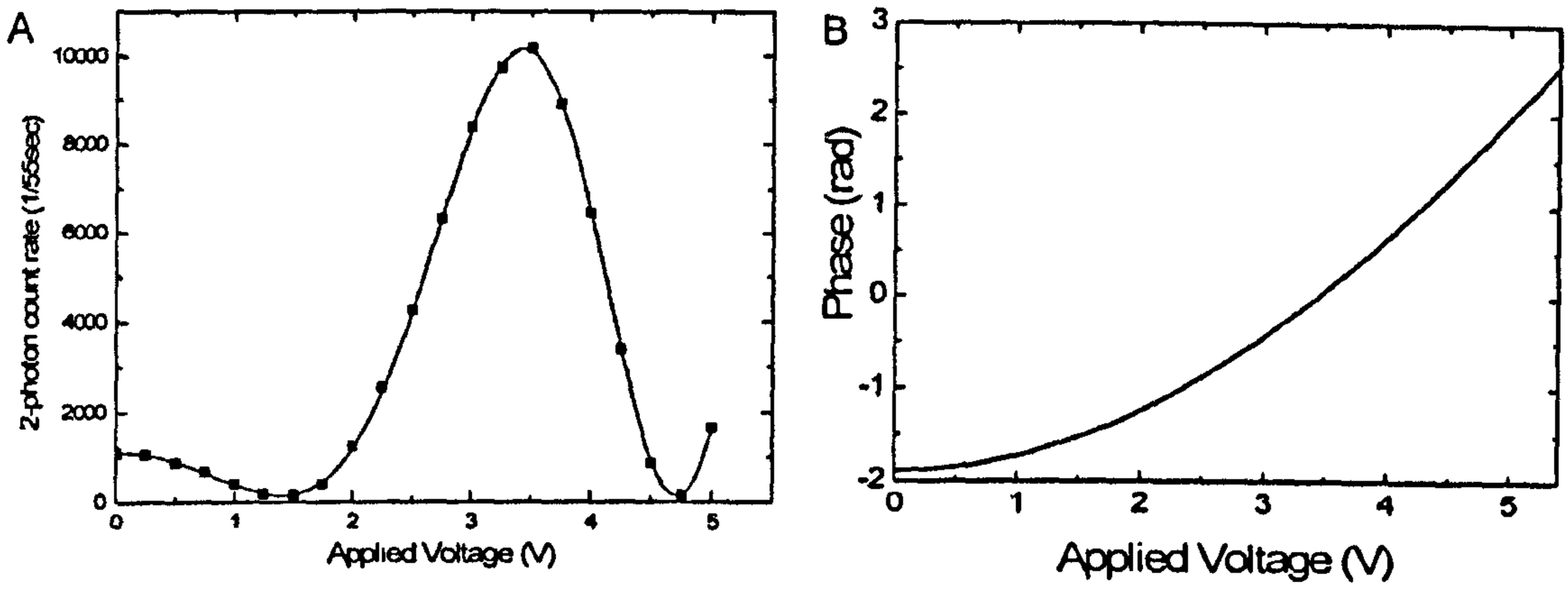

Figure 6.3: Calibration of the Mach-Zehnder interferometer: rate of two-photon coincidental detection varying the voltage applied to the resistive heater between 0 and 5V. Error bars are given by Poissonian statistics. B: Plot of the phase-voltage relationship determined from this calibration.

reason each device had to be calibrated to relate the applied voltage to the phase difference introduced in the interferometer. A two-photon experiment was used to find the $\phi(V)$ relation. One photon was launched into each of the ports a and b of the device so that the maximally entangled two photon Fock state $|2\rangle_c|0\rangle_d + |0\rangle_c|2\rangle_d$ is generated inside the chip. Controlling the phase ϕ in the device, the phase of the entangled state is altered according to $|2\rangle_e|0\rangle_f + e^{2i\phi}|0\rangle_e|2\rangle_f$. In comparison to simply using one-photon "classical" interference, this "quantum calibration" harnesses the reduced de Broglie wavelength [76–78] of two-photon interference [79–85] to reduce the error of the $\phi(V)$ relation. This is because it is possible to test a wider sample of the interference fringe, since the set of the value of the phase ϕ can assume is limited by the maximal voltage (current) that it is possible to apply to the resistive heater. Figure 6.3A shows the results of this calibration in which the rate of simultaneous detection of two photons at outputs g and h is plotted as a function of the applied voltage V across p_1 and p_2.

In first approximation, the applied phase ϕ is proportional to the power dissipated by the resistor. This translates into a quadratic relation between the applied

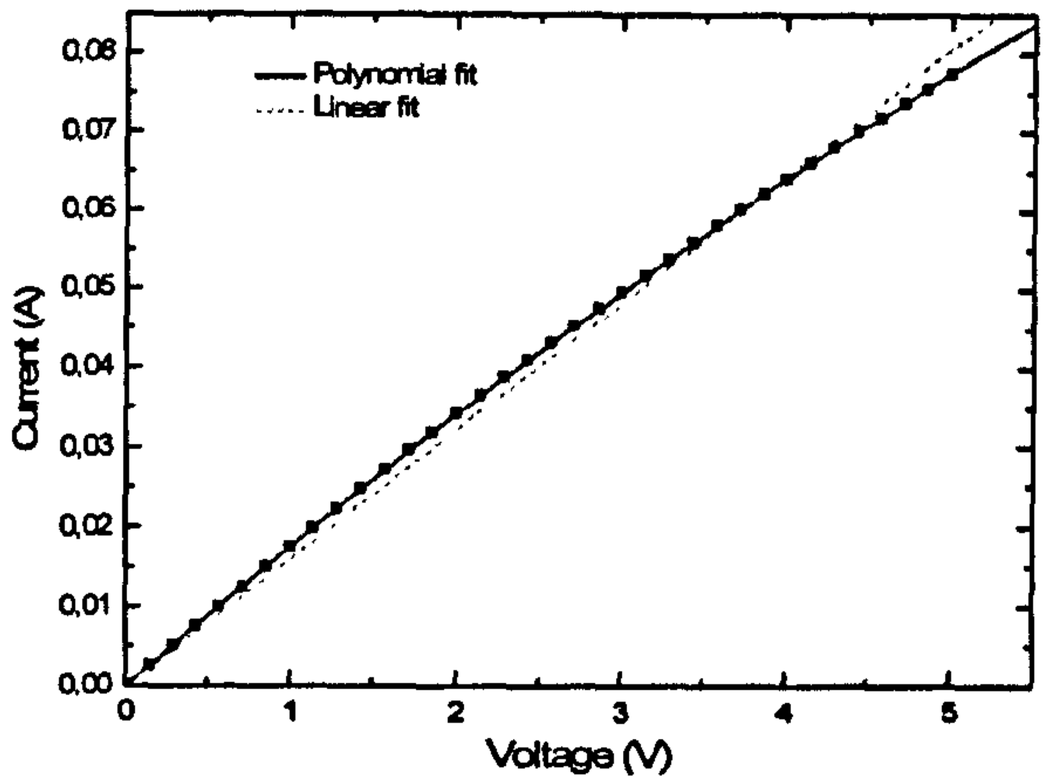

Figure 6.4: Current-Voltage relation of the resistive heater. To highlight the non-ohmic relation, the graph shows a linear and a polynomial best fit.

voltage and the phase. To take into account deviations from the ideal case, mainly due to a non-ohmic current-voltage relation as the temperature changes (as shown in figure 6.4), the form of the $\phi(V)$ relation was fixed as:

$$\phi(V) = \alpha + \beta V^2 + \gamma V^3 + \delta V^4. \tag{6.1}$$

The V^3 term is related to non-ohmic behavior of the resistor, and the V^4 term is a combination of non-ohmic relation and the expansion of $\phi(V)$ in even powers of V. A best fit analysis on the two-photon interference data was performed to calculate the parameters in the $\phi(V)$ relation. The parameters computed from the complete calibration process for $\phi(V)$ are reported in Table 6.1. In figure 6.3B it is possible to appreciate the $\phi(V)$ relationship determined from the calibration process.

6.2.2 Experimental results

After the calibration process, it was possible to measure the interference pattern of single photon detections at the two outputs of the circuit when launching single photons into one input of the integrated device and varying the phase ϕ. As the phase of one waveguide is changed by applying a voltage across the resistive heater,

Table 6.1: Values of the parameters obtained from the best fit in the calibration of $\phi(V)$.

Parameter	Value	error
α	-1.887	0.006
β	0.157	0.005
γ	0.0045	0.002
δ	-0.001	0.0002

the probability of detecting photons at the outputs g and h varies according to $P_g = \frac{1}{2}[1-\cos(\phi)]$ and $P_h = \frac{1}{2}[1+\cos(\phi)]$. The observed fringes, shown in in figure 6.5A, show a high contrast $C = (max - min)/(max + min)$ of $C = 98.2 \pm 0.3\%$. From the contrast value it is possible to calculate how well this device would perform if used to prepare path-encoded states. This is described by the average fidelity between the measured and ideal output state $U_{MZ}|0\rangle = \cos(\phi/2)|0\rangle + \sin(\phi/2)|1\rangle$. Assuming no mixture or complex phase are introduced and averaging over the range $\phi \in [-\pi/2, \pi/2]$, it is possible to calculate the average fidelity to be $F = 99.984 \pm 0.004\%$.

An experiment to check the stability of the phase applied in the Mach-Zehnder interferometer was performed using single photons. Figure 6.6 shows the probability of detecting a photon in mode h when sending single photons in input a as a function of time, a voltage of $1.4V$ was applied across resistive element. The probability remained almost constant for more than six hours. The small deviation is imputed to the different evolution of the coupling from the waveguides g and h to the fiber array that collect the photons at the output of the circuit. However, different evolution of the coupling efficiencies does not lower the quantum mechanical performance of the device.

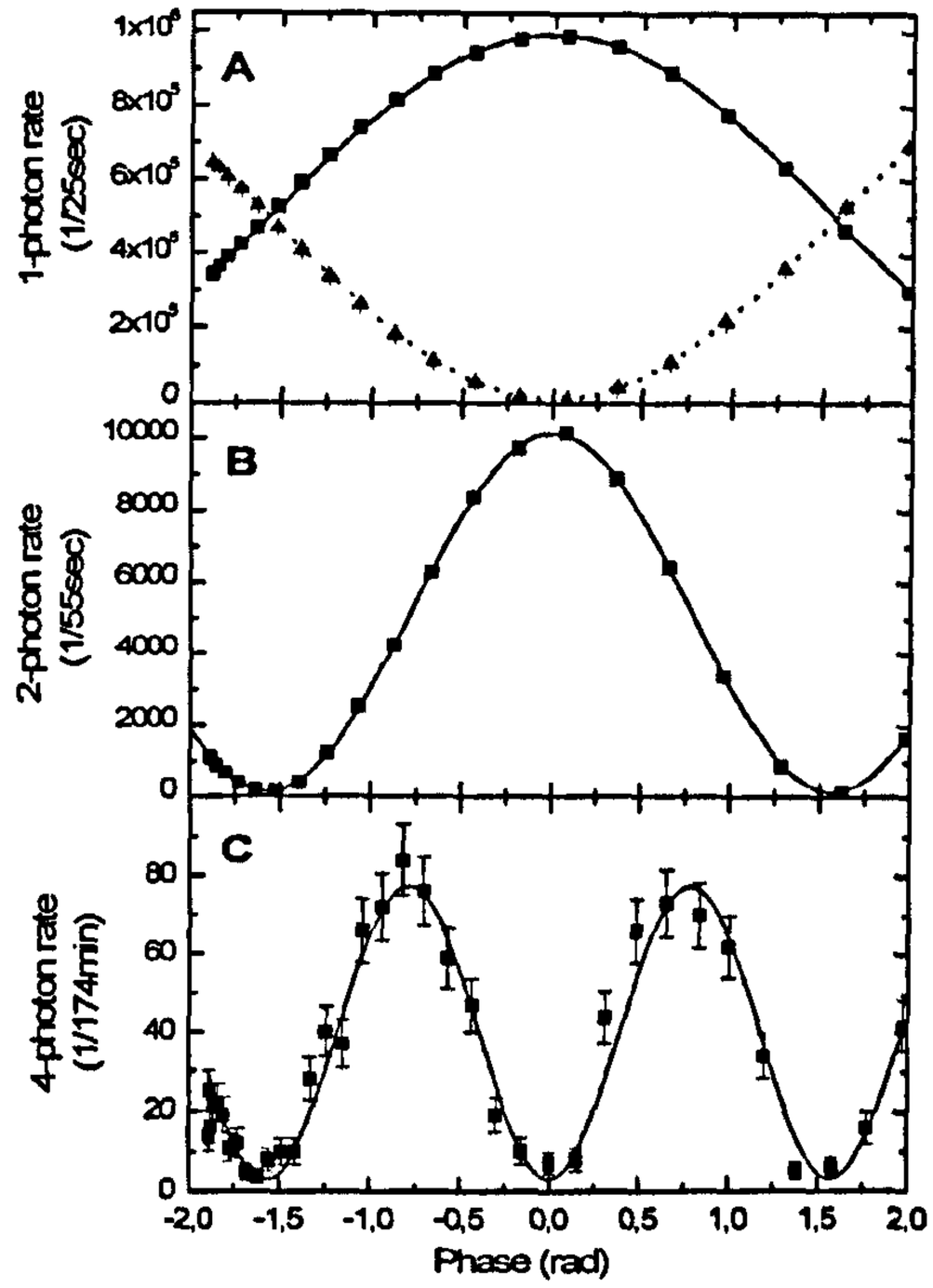

Figure 6.5: Integrated quantum metrology. A) Single photon count rates in the outputs g and h as the phase $\phi(V)$ is varied. B) Two-photon coincidental count rate between the outputs g and h when the state $|1\rangle_a |1\rangle_b$ is launched in the interferometer and varying the phase $\phi(V)$. C) Four-photon detection rate of the output state $|3\rangle_g |1\rangle_h$ when inputting the four-photon state $|2\rangle_a |2\rangle_b$.

6.3 Entanglement manipulation on a chip

Phase control capability is also important for the on-chip generation, manipulation and analysis of entangled quantum states. By inputting the indistinguishable two-photon state $|1\rangle_a |1\rangle_b$ into the first directional coupler of the Mach-Zehnder circuit, the two-photon maximally entangled state $|2\rangle_c |0\rangle_d + |0\rangle_c |2\rangle_d$ is generated inside the device. Through controlling the phase ϕ, the entangled state is altered according to $|2\rangle_e |0\rangle_f + e^{2i\phi} |0\rangle_e |2\rangle_f$. Simultaneous detection of a single photon at each output yields a two-photon interference fringe with twice the frequency of one-photon interference, according to $P_{g,h} = \frac{1}{2}(1 + \cos 2\phi)$. Such two-photon interference

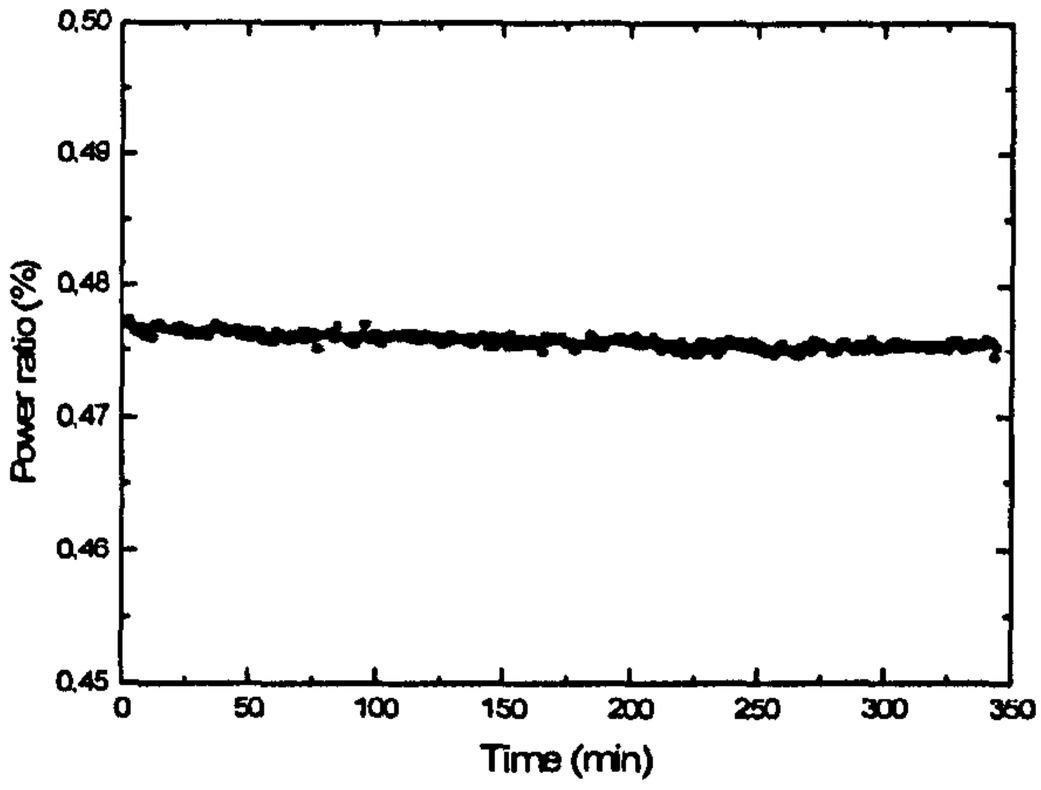

Figure 6.6: Probability of detecting a photon in mode h when sending a single photon in input a as a function of time. To see the stability of the phase, the probability axis is zoomed in on the range (0.45, 0.5).

fringes are shown in figure 6.5B which plots the measured two-photon coincidence rate as a function of the phase ϕ. The curve shows a contrast of $C = 97.2 \pm 0.4\%$, greater than the threshold of $C_{th} = 1/\sqrt{2}$ required to beat the shot noise limit for two-photons [76, 77, 85, 86].

The accuracy and stability with which the resistive heater controls the phase inside an integrated waveguide MZ interferometer, as shown by the one- and two-photon interference fringes, leads to applications in technologies such as quantum metrology. As a proof of principle, this requires demonstration using maximally entangled N00N states of the form $|N0\rangle + |0N\rangle$ (expressed as a photon number Fock state in two paths) [31]. Unfortunately, for N larger than 2, it is not currently simple to directly generate such states using photons produced with SPDC and linear optical circuits in a deterministic manner [85]. It is, however, possible to solve this problem by post-selecting the presence of the maximally entangled 4-N00N state: by inputting the state $|2\rangle_a |2\rangle_b$ into the interferometer, non-classical interference at the first directional coupler produces the state

$$\sqrt{3/4}\left(|4\rangle_c |0\rangle_d + |0\rangle_c |4\rangle_d\right)/\sqrt{2} + 1/\sqrt{4}\,|2\rangle_c |2\rangle_d . \tag{6.2}$$

At the second directional coupler, only the $|4\rangle_c |0\rangle_d + |0\rangle_c |4\rangle_d$ part of the state

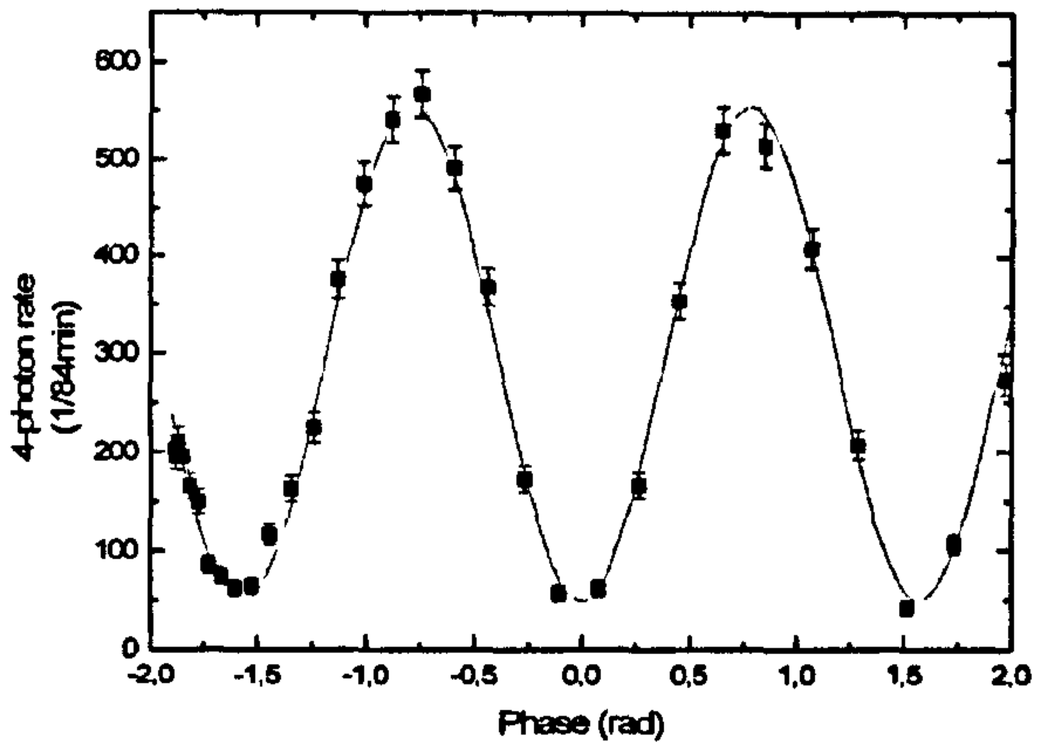

Figure 6.7: Four-photon detection rate of the output state $|3\rangle_g |1\rangle_h$. The experiment was conducted with a high pump power to obtain higher four-photon count rates.

in equation 6.2 gives rise to either of the terms $|3\rangle_e |1\rangle_f$ or $|1\rangle_e |3\rangle_f$ in the output state of the interferometer. By detecting either of the states $|3\rangle_e |1\rangle_f$ or $|1\rangle_e |3\rangle_f$ (by cascading three detectors using 1×2 fibre-beam splitters on either outputs g or h of the device) a $\lambda/4$ interference fringe can be observed [77, 87]. By varying the phase of the interferometer by ϕ, the probability to detect the 3:1 pattern has a period of $\phi/2$. The measured interference pattern is shown in figure 6.5C, which plots four fold detections corresponding to the detection of the $|3\rangle_g |1\rangle_h$ against the phase ϕ of the device. The contrast of the four-fold interference fringe is $C = 92 \pm 4\%$. Despite the post-selection scheme, this is still sufficient to beat the shot noise limit [86].

The four-photon N00N experiment was repeated using a higher pump power from the Ti:Sapphire laser. This was done to confirm with a higher accuracy the reduced de Broglie wavelength by obtaining lower error bars for the experiment. As the power of the pump is increased, the four-photon production rate increases, but by the same argument, the production of 6-photons start to be non-negligible. This reduces the contrast of the measured fringe visibility, since losses and avalanche detectors that cannot resolve photon number give rise to spurious counts of the $|3\rangle_g |1\rangle_h$ state.

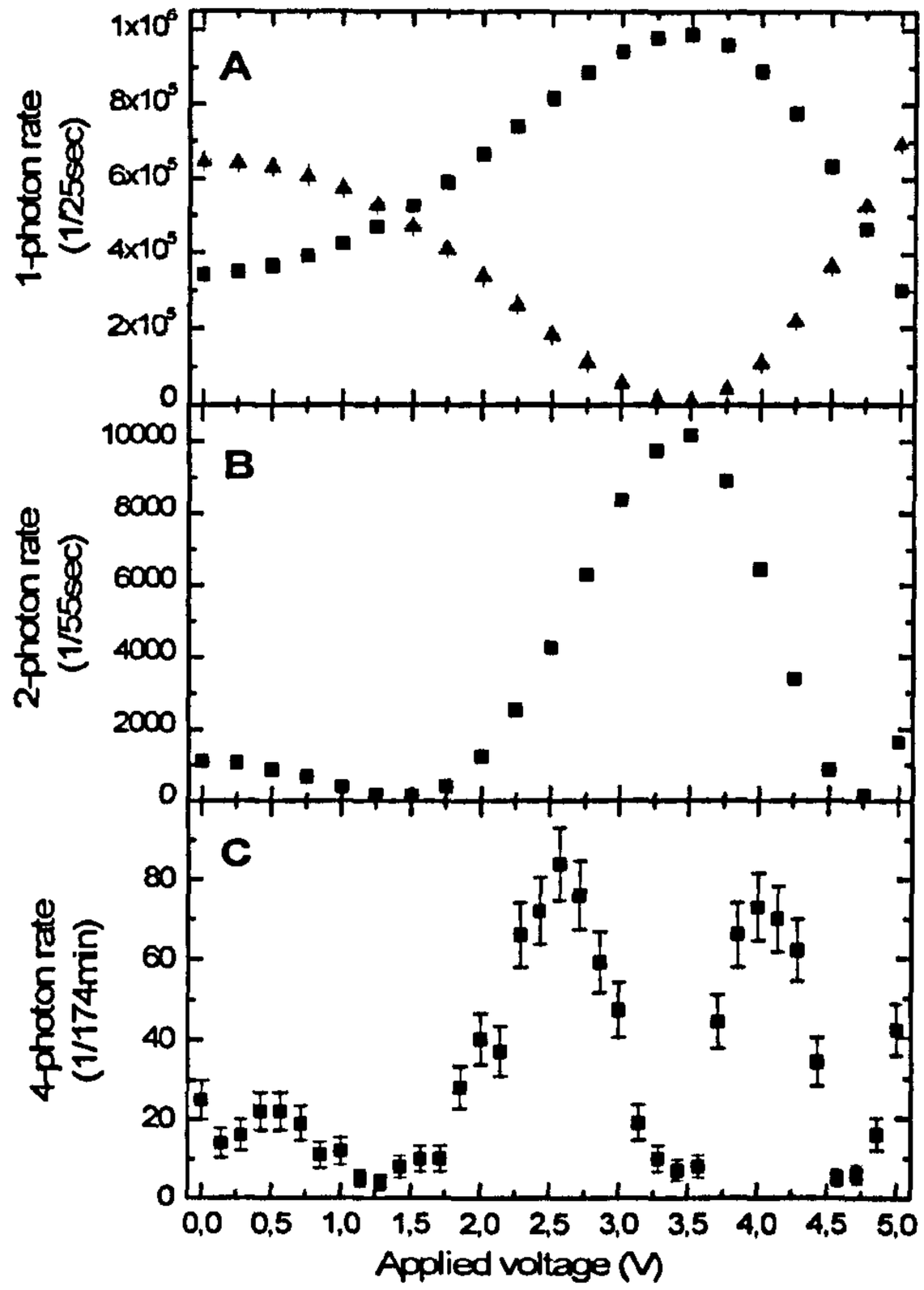

Figure 6.8: One- (A), Two- (B) and Four- (C) photon count rates (as in figure 6.5) as the voltage V is varied. The figure outlines that no calibration process of the phase-voltage relation is needed to observe super-resolution with multi-photon inputs.

Figure 6.7 shows the four-photon detection rate of the output state $|3\rangle_g |1\rangle_h$ at this higher pump power, while varying the phase ϕ of one arm of the interferometer. The contrast of the four-fold interference fringe is $C = 83.1 \pm 1.5\%$, which, despite the post-selecting detection scheme and the higher power, is still sufficient to beat the shot noise limit. Note, however, that the reduced visibility is the result of 6 photons being generated at higher pump power.

I would like to stress here that, although a two-photon interference fringe was used to calibrate the phase shift, this calibration is not required to claim a $\lambda/2$ interference fringe; this is simply confirmed by the one-, two- and four-photon

fringes, which can be done even without calibrating the phase. In figure 6.8 it is possible to note the raw data shown in figure 6.5 without the calibration for the $\phi(V)$ relationship. The super-resolution of the fringes is easily noticed.

6.4 Reconfigurable quantum circuit

In addition to single photon interference in interferometers, non-classical interference of two photons can be investigated in integrated devices in a similar manner, as described in the previous section. Directional couplers offer high performance and stable results for quantum optics operations. In these devices the reflectivity η is set in the fabrication process. However, more general photonic circuits, including adaptive schemes whose function depends on the input state, such as Fock state filters [69, 70], make use of devices equivalent to a single coupler with variable η. Reconfigurable photonic circuits, including routing of photons, can be realized by combining such variable η devices. By controlling the phase ϕ within our devices, it is possible to specify the unitary operation:

$$U_{MZ} \doteq \begin{pmatrix} \sin(\phi/2) & \cos(\phi/2) \\ \cos(\phi/2) & -\sin(\phi/2) \end{pmatrix}, \tag{6.3}$$

when acting on an arbitrary superposition of the two input paths. This operation is equivalent to a single coupler with variable reflectivity

$$\eta = \sin^2\left(\frac{\phi}{2}\right). \tag{6.4}$$

Multiple quantum interference experiments were performed in which two photons were launched into inputs a and b of the device. While scanning through the relative arrival time with an off-chip optical delay, the rate of simultaneous detection of a single photon at both outputs g and h were measured. Each experiment resulted in a quantum interference "dip" in this rate of simultaneous photon detection. The main panel in figure 6.9 plots the quantum interference visibility observed for different values of ϕ and hence η. Figure 6.9 also shows two examples

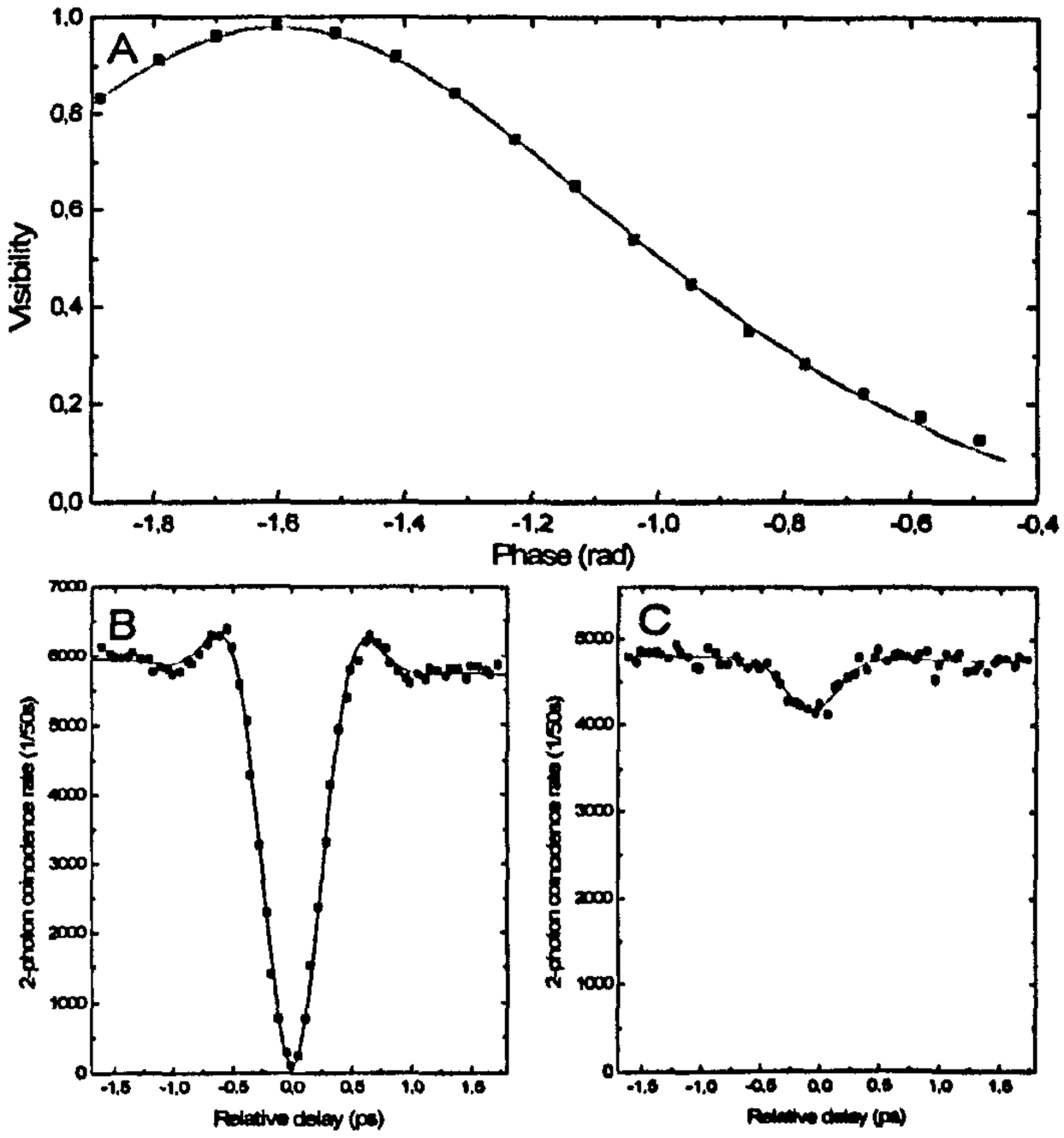

Figure 6.9: Controlling the degree of quantum interference on a single chip. A): Visibility of the quantum interference versus applied phase in the integrated Mach-Zehnder interferometer. The solid line is a theoretical fit with only a phase-offset and a single mode-mismatch as the free parameters. B): High visibility two-photon interference for $\phi = -1.602 \pm 0.01$ rad. C): Low visibility two-photon interference for $\phi = -0.49 \pm 0.01$ rad. The best fit function in both plots takes into account the non gaussian shape of the interference filter used in the experiment.

of the raw data used to generate this curve: figure 6.9C $\phi = -0.49 \pm 0.01$ rad, $V = 0.129 \pm 0.009$; figure 6.9B $\phi = -1.602 \pm 0.01$ rad, $V = 0.982 \pm 0.009$.

Chapter 7

Two qubit gates

In this Chapter I will present the implementation of two-qubit quantum gates in integrated optics architecture. In particular, the realization of probabilistic Controlled-NOT gates will be studied. After the introduction of the scheme used to construct a CNOT gate with photons, the experimental results will be presented. Even if, at this stage, process tomography can not be easily performed on the chip, I will present a method to test the coherent operation of the circuit that implements the two-qubit gate. In the last section, results and consideration about the errors present in the gate are presented to understand the potentialities of integrated optics quantum computation.

This Chapter is based on the results published in the following articles:

A. Politi , M. J. Cryan, J. G. Rarity, S. Yu, and J. L. O'Brien, Silica-on-Silicon Waveguide Quantum Circuits, *Science* **320**, 646 (2008);

A. Politi, J. C. F. Matthews, M. G. Thompson, J. L. O'Brien, Integrated Quantum Photonics, *Journal of Selected Topics in Quantum Electronics*, **15**, 6, 1673-1684, (2009);

A. Laing, A. Peruzzo, A. Politi, M.R. Rodas, M. Halder, T. C. Ralph, M. G. Thompson, J. L. O'Brien, Towards fault tolerant quantum photonic circuits, *Submitted*.

7.1 Controlled-NOT gate with photons

Entanglement is fundamental for quantum information processing as well as for quantum science in general. For this reason, any candidate technology for quantum applications needs to prove the ability of generating entangled states. An example of a quantum circuit capable of manipulating the state of two qubit in such a way that the final output can be entangled is the controlled-not (CNOT) gate. The CNOT flips the state of a target (T) qubit conditional on a control (C) qubit being in the $|0\rangle$ logical state.

The CNOT is a notable example of quantum gates since, with one qubit rotations, it is universal for quantum information and, in the photonic implementation, it relies on both quantum and classical interference. For this reason the performance of the CNOT gate is a benchmark to evaluate the capabilities of the technology under study. The implementation of the CNOT gate proposed by T.C. Ralph *et al.* [88, 89], shown in figure 7.1, has been tested. This scheme has previously been experimentally demonstrated using bulk optics [17–21], using different ingenious methods to avoid instability in the classical interference. The waveguide implementation, however, is essentially a simple direct-write onto the chip from the theoretical schematic.

The gate works as follow: control C and target T qubits are each encoded by a photon in two waveguides. Two $\frac{1}{2}$ splitters in target waveguides (T_0 and T_1) forms a balanced Mach-Zehnder Interferometer, so that, with no inputs in the

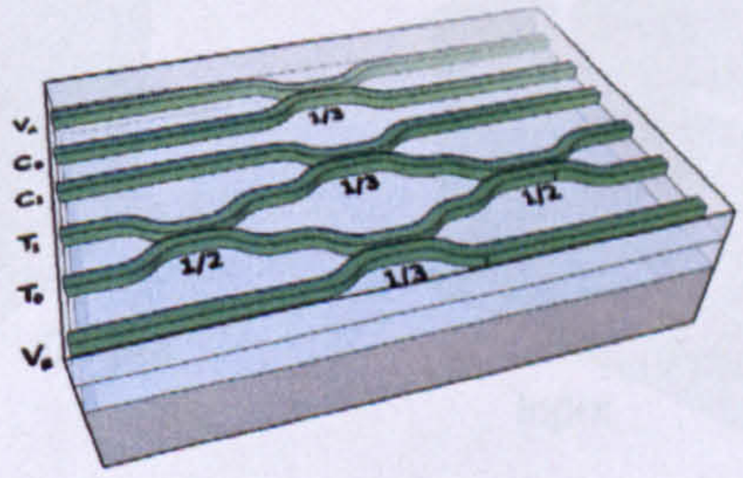

Figure 7.1: Schematic representation of an integrated CNOT gate.

control waveguides (or a photon in the control state zero C_0), the target photons exit the interferometer from the same port as the input port (Note that for the rest of this Chapter I use the convention $U_{dc} = H$, this involves just the relableling of waveguides outputs). For the control in the state one (photon in the waveguide C_1), the control and target photons interfere non-classically at the central $\frac{1}{3}$ splitter. For such a value of splitting ratio, the resulted state evolves to $|1\rangle_C |0\rangle_T \rightarrow -1/3(|1\rangle_C |0\rangle_T)$. This causes a π phase difference between the arms of the interferometer, so that the target qubit is flipped. The presented scheme does not always work, it is possible, for example, to find two photons in the control or target outputs. However the presence of only one photon in the control and one photon in the target herald the success of the gate. The probability of such an event is equal to 1/9 for all the possible combinations of inputs states.

7.1.1 Experimental results

To test the performance of the CNOT gate, the four computational basis states $|0\rangle_C|0\rangle_T$, $|0\rangle_C|1\rangle_T$, $|1\rangle_C|0\rangle_T$, and $|1\rangle_C|1\rangle_T$ were set as the input of the device. The photons were measured to obtain probability of detecting each of the computational basis states at the output (figure 7.2. The excellent agreement for the $|0\rangle_C$ inputs (peak values of 98.5%) is a measure of the classical interference in the target interferometer and demonstrates that the waveguides are stable on a subwavelength

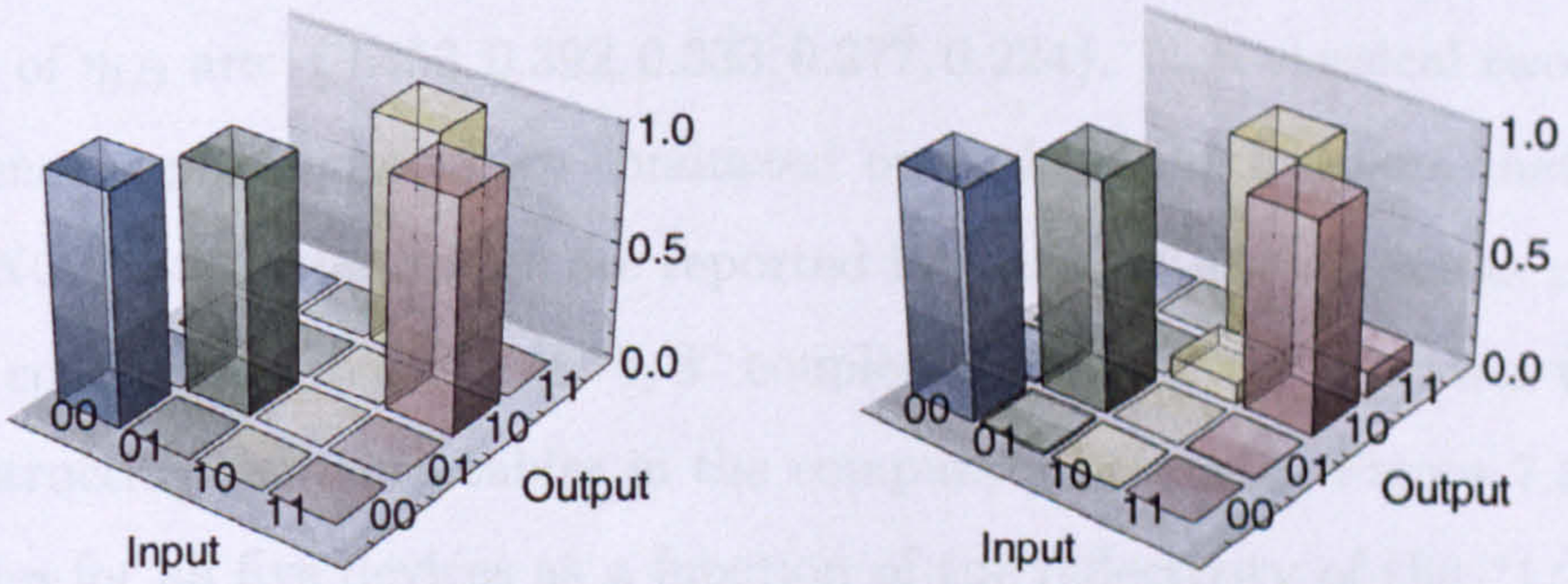

Figure 7.2: Characterization of integrated quantum photonic circuits. Ideal (left) and measured (right) truth tables for a CNOT circuit.

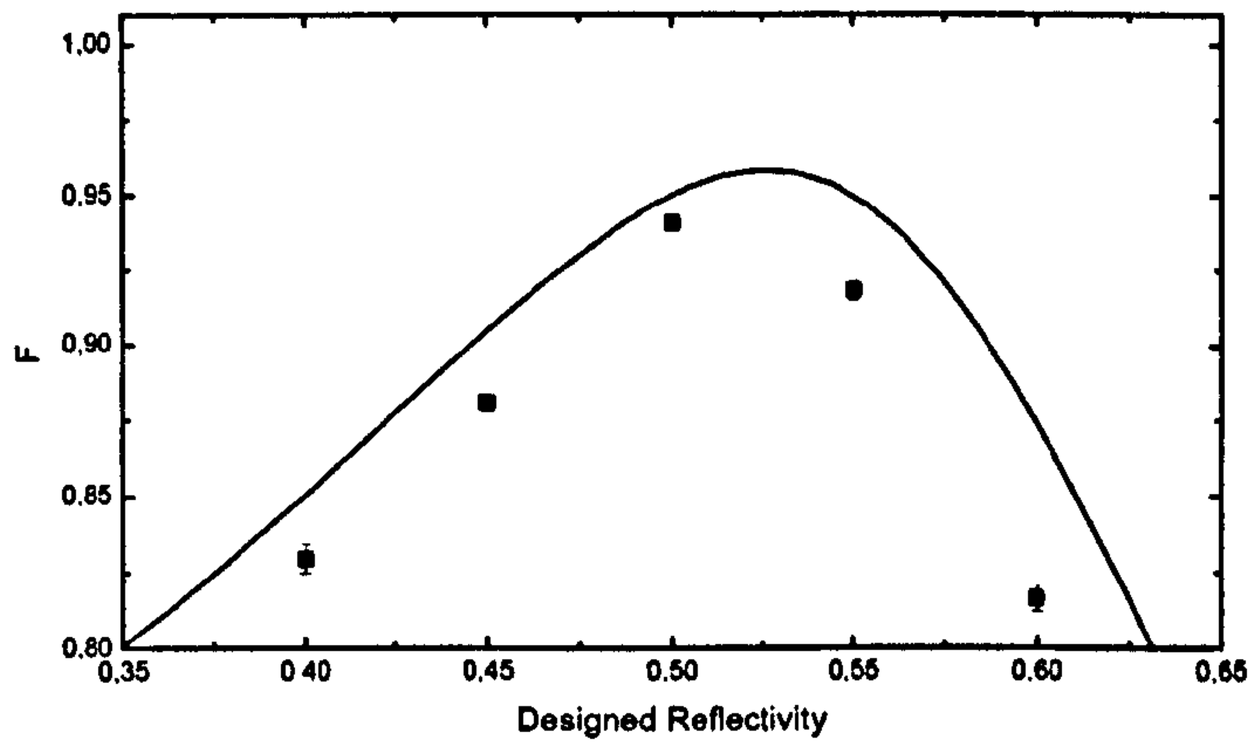

Figure 7.3: Fidelity of the CNOT gate as a function of the reflectivity of the couplers that constitute the device. The solid line represents a best fit with only the reflectivity as free parameter and perfect behavior of the target interferometer. This last assumption explains the difference with the experimental points.

scale—a key advantage arising from the monolithic nature of an integrated optics architecture. The average of the logical basis fidelities is $F = 94.3 \pm 0.2\%$.

To perform a deeper study of the integrated CNOT gate, and to prevent possible design and fabrication imperfections, a lithography tuning was made on the reflectivity of the couplers that constitute the gate. The "1/2" couplers have reflectivity in the range $\eta = 0.4 - 0.6$ in steps of 0.05. The reflectivity of the "1/3" couplers varies accordingly with the reflectivity of the "1/2" ones, in such a way that if the "1/2" has $\eta_{1/2} = 0.5$ then $\eta_{1/3} = 0.33$. For this reason, the values of $\eta_{1/3}$ are: $\{0.453, 0.392, 0.333, 0.277, 0.224\}$. Non-classical two-photon interference experiments where conducted on each of the couplers that constitute the CNOT gates, the results are reported in figure 4.6 (black points representing "1/2" couplers and red points "1/3" couplers). Each CNOT gate was then tested, reconstructing the truth tables in the computational basis. Figure 7.3 shows the fidelities for all five devices as a function of the reflectivity of the "1/2" couplers of the gates. The best fit follows well the trend of the experimental points, the discrepancy between them is attributed to the fact that the theoretical model used for the best fit does not take into account the non-perfect behavior of the target

interferometer.

Other simple quantum photonic circuits were tested to show the flexibility of the integrated approach. The devices, shown in figure 7.4A and B, consist of a CNOT gate and Hadarmard H gates each implemented with a 50:50 coupler between the C_0 and C_1 waveguides. It is possible to quantify the agreement between the experimental data and the ideal operation by using the average classical fidelity between probability distributions S [90, 91]:

$$S = \frac{1}{16}\left(\sum_{i,j=0}^{4}\sqrt{M_{ij}T_{ij}}\right)^2 \tag{7.1}$$

where M_{ij} and T_{ij} are the elements of the measured and expected truth tables respectively. For the data shown in figure 7.4A, that should produce equal superpositions of the four computation basis states $|00\rangle \pm |01\rangle \pm |10\rangle \pm |11\rangle$, the average classical fidelity with the ideal case was measured to be $S = 97.9 \pm 0.4\%$. The device that gives the results shown in figure 7.4B is an interesting device, since it should produce the four maximally entangled Bell states $\Psi^{\pm}$ and $\Phi^{\pm}$. For this device the similarity with the ideal case was measured to be $S = 91.5 \pm 0.2\%$. While the presence of the entangled state at the output cannot be confirmed directly on-chip, the above demonstrations of excellent logical basis operation of the CNOT and coherent quantum operation provide great confidence.

7.2 Coherence and entanglement in integrated CNOT gates

Performing quantum measurements on the single components of the CNOT gate, and measuring high fidelity for the operation of the gate with inputs in the computational basis ensures the correct behavior of the integrated chip. However, if we take the quantum discrimination theory point of view and look at the chip as a black box (not using any information we have about the actual components of the device), it is simple to understand that the fidelity value is not enough to

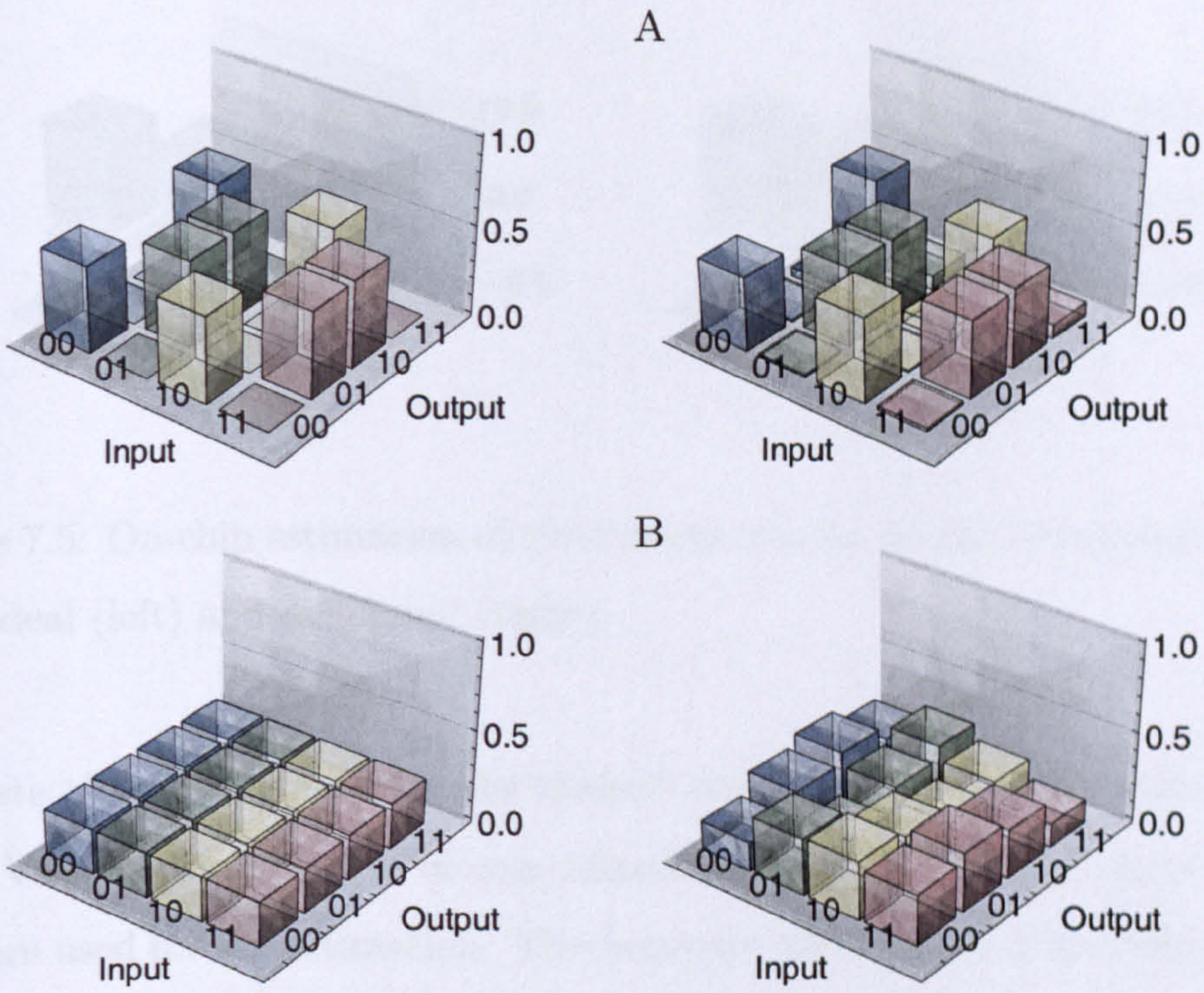

Figure 7.4: Characterization of integrated quantum photonic circuits. Ideal (left) and measured (right) truth tables for a CNOT with two additional H gates (A); and a CNOT with one additional H gate (B)

fully characterize the quantum gate. To perform such a characterization, quantum process tomography is needed. Unfortunately, at the present stage process tomography for a two qubit operation is hard to implement in path encoding, directly on the chip, since it requires many Mach-Zehnder interferometers and phase shifters to be controlled at the same time. An experimental method was conceived to confirm on-chip coherent quantum operation and entanglement, the most important properties of the CNOT gate.

Two single photons were launched into the T_0 and T_1 waveguides. The state after the first 1/2 coupler should evolve to

$$|11\rangle_{T_0T_1} \rightarrow \frac{1}{\sqrt{2}}(|20\rangle_{T_0T_1} - |02\rangle_{T_0T_1}), \tag{7.2}$$

that is, the entangled state also used in the previous section for quantum metrology. Using part of the circuit that compose the CNOT gate it is possible to

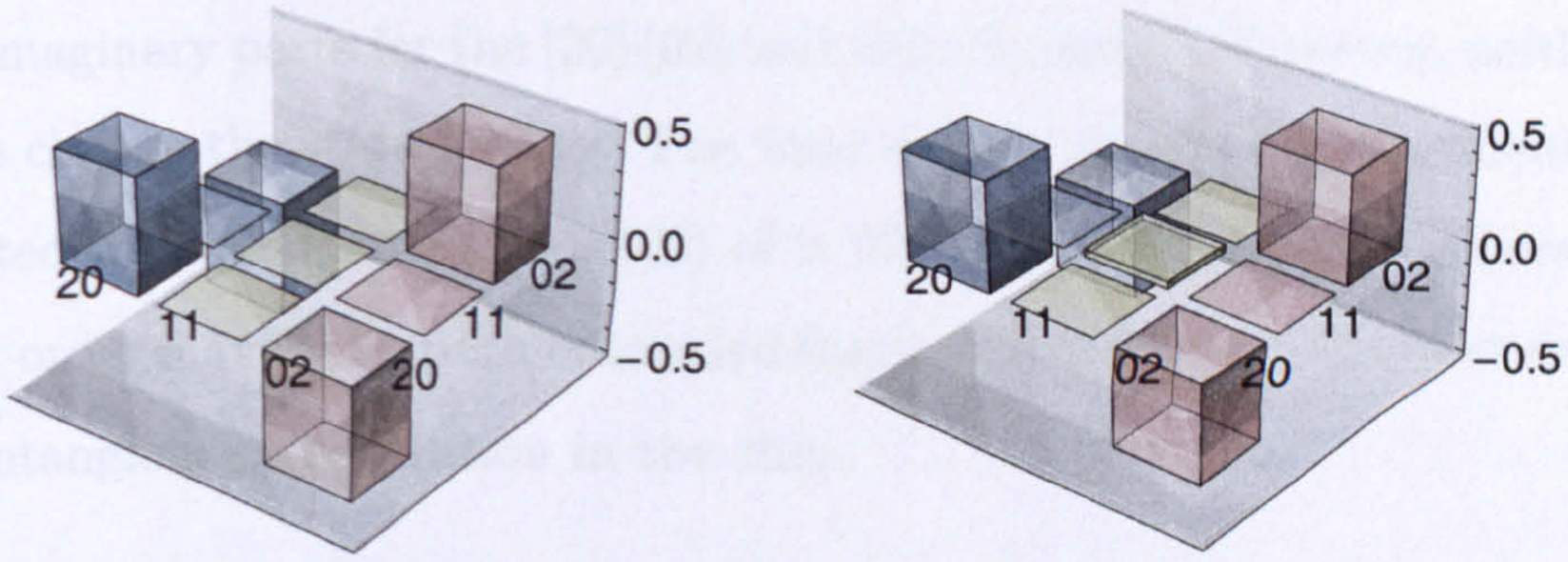

Figure 7.5: On-chip estimation of the density matrix for the entangled state $|20\rangle - |02\rangle$, ideal (left) and estimated (right).

estimate the fidelity between the desired state and the state produced into the chip. Various combinations of coincidental detections of two photons at the outputs are used for the estimation. The heuristic explanation of the argument is the following: measuring the photon rates at C_1 and V_A leads to the evaluation of the diagonal elements of the density matrix. A low rate of coincidental detections of two photons between C_1 and V_A outputs translates to a low $|11\rangle$ component in the state, meanwhile a high rate of two-photon detections in either of these output waveguides (measured using a pair of cascaded detectors) ensures that the state is predominantly composed of $|20\rangle$ and $|02\rangle$ components. These measurements, however, do not give any information about the coherence of the state. At the second 1/2 coupler between the T_0 and T_1 waveguides the reverse transformation of Eq. 7.2 should occur, provided the minus sign of the superposition exists. A high rate of detecting one photon in each of the T_0 and T_1 outputs combined with a low rate of two-photon detections in either of these outputs confirms this transformation.

The above measured count rates, and a worst case scenario for the state evolution, were used to estimate the density matrix of the state after the first 1/2 coupler directly on-chip, the results are shown in figure 7.5. It was not possible to estimate all the coherence elements of the matrix, however the amount of the unmeasured elements is limited by the small $|11\rangle\langle 11|$ population. Also, it was not possible to distinguish between non-maximal coherences and rotated coherences

with imaginary parts for the $|20\rangle\langle 02|$ and $|02\rangle\langle 20|$ terms. However, neither of these effects change the state fidelity. The final density matrix show a fidelity with the expected entangled state $|20\rangle - |02\rangle$ of $> 92\%$. This high fidelity generation of the lowest order maximally path entangled state confirms coherent quantum operation and entanglement generation in the chip.

7.3 Towards fault-tolerance optical quantum computation

As for the directional coupler in Chapter 4, it is interesting to analyze the phenomena that limit the CNOT gates to a fidelity of $F = 94.3 \pm 0.2\%$. The analysis is especially interesting in the light of the fact that the presence of errors in quantum operations is detrimental to the computation. Intuitively, quantum states are fragile, and real gates are never perfect, so errors are present during quantum operations. Nevertheless, it is possible to counteract these errors from imperfect devices using quantum error correction techniques [92], if the error per gate (EPG) is below a certain threshold. If the architecture satisfy these conditions, it is said to be fault tolerant, and arbitrary long quantum computation can be achieved [93]. Depending on the models of error used, and the way to counteract the propagation of errors, thresholds in the EPG value exist that permit to achieve quantum computing. The values of EPG lies in the range between few percent and 10^{-4} [94–97].

For photons, it is possible to divide the errors in two broad classes: locatable and unlocatable. Locatable errors are essentially qubit erasure, caused by loss or gate failures. These are easier to fix and hence have a higher threshold. Unlocatable errors correspond essentially to bit flips (or similar unwanted qubit evolution) during the computation. Since unlocatable errors propagate in the computation in an unpredictable way, they corresponds to more stringent thresholds.

In contrast to most systems, where fast coupling to the environment dominates,

the major sources of error in linear optic implementations are photon loss, including source and detector inefficiency; imperfect classical interference of photons, due to instability of optical circuits; and imperfect quantum interference, due to mode matching. Apart losses, which are locatable, the other kind of imperfections translate in non-perfect single or two-qubit operations, that are unlocatable.

In Chapter 6, I showed the results obtained with integrated optical devices that suggests the possibility of performing single-qubit operations with high performances. Fidelities as high as $F = 99.99\%$ are possible with the present technology, and with new devices and materials, higher values can be obtained. For this reason, in the case of photonic quantum information, the major limitations to reach fault tolerant operation are coming from two-qubit operations.

In Section 4.4.1 it is explained how, after the improvement of the source of down-converted photons and taking into account the effect of the window time of the counting electronics, high performance non-classical interference was reported. Since the probabilistic CNOT gate presented in this Chapter heavily relies on non-classical (and classical) interference, it is interesting to analyze how the same improvements for the coupler case translate to the two-qubit performances.

The truth table in figure 7.6C represents the measurements outcomes in the computational basis for the case of the CNOT gate with "$\eta = 0.5$" couplers. The effect of the improvement in the indistinguishability of the photons, and the correction for the accidental counts brings the fidelity to $F = 96.9 \pm 0.2\%$. This is probably the highest value for the fidelity of a two-qubit gate ever reported to date in the photonic approach for quantum information.

A theoretical model of the optical network can be useful to understand the sources of error in the measured gate. A model was developed that takes into account the imperfection in the coupling ratio of the couplers that compose the network. For this task, the reflectivity of the couplers were measured with the method presented in Section 4.2. The '1/3' coupler in the control part of the circuit was measured to be $\eta = 0 : 308 \pm 0.001$. For the model it was assumed that all the 1/3 couplers have the same value. This approximation is necessary

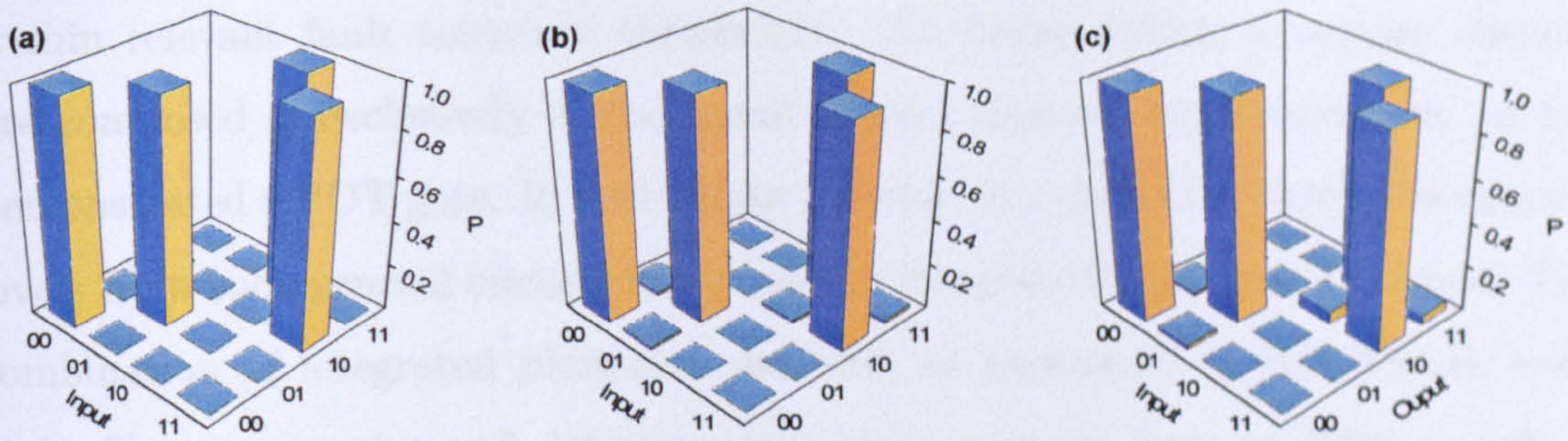

Figure 7.6: High-fidelity logic gate operation. (a) The truth table of a CNOT gate. (b) The ideal truth table four the measured device. (c) The experimentally measured truth table. The fidelity between (a) and (b) is $F = 96.9 \pm 0.2\%$.

because it is not possible to reconstruct the reflectivity of the of two lower '1/3' couplers in the target circuit, since they are embedded in an interferometer. This assumption is reasonable given the previous data on lithographic devices shown in this Thesis. Indeed the two '1/2' couplers were measured to be $\eta = 0.442 \pm 0.001$ and $\eta = 0.452 \pm 0.001$.

Figure 7.6B shows the expected outcomes of a CNOT network with the reflectivities above. To measure the agreement between the model and the data, the similarity between truth-tables was computed. The two truth-tables show a similarity of $S = 99.3 \pm 0.2\%$. This value demonstrates that the major sources of error in the present gate are coming from imperfections in the coupling ratio values. This problem can be counteract with a more precise simulation analysis of the integrated structures, combined with tighter fabrication tolerances. Otherwise, as demonstrated in the previous Chapter, phase shifters can be used in the circuit to implement couplers with well defined splitting ratios.

The importance of the results presented in this Section resides in the demonstration that photonic quantum circuits show no fundamental limitations in the achievement of high performances quantum operations. The presented gate can operate in the fault tolerant regime, since assuming operation at the lower bound of the error bars puts the devices described here in the $10^{-2} - 10^{-3}$ EPG regime,

within relevant fault tolerance thresholds. All linear optical quantum circuits are composed of exclusively of the quantum and classical interferometers, as the demonstrated CNOT gate. It is therefore possible to expect the same performance levels from such general circuits fabricated in integrated optics architecture. The combination of integrated photonics network, as presented in this Thesis, with high-efficiency sources and detectors will likely provide fault tolerant quantum circuit operation.

Chapter 8

Quantum algorithms

In this Chapter I will explain how, by using the integrated optics components described in this Thesis, it is possible to implement simple quantum algorithms on a chip. In particular, I will concentrate on the implementation of the Shor's quantum algorithm to factorize the number 15. After a short introduction about the problem and importance of factorizing large prime numbers, I will briefly explain how the quantum computation works in the general case. The complexity and the number of quantum gates required for the physical implementation of the computation make the algorithm unfeasible in the near future. For this reason, I will introduce a way to simplify the algorithm. The "compiled" version of the algorithm takes into account a number of simplifications that make the quantum computation experimentally feasible. I will, therefore, conclude by presenting the scheme and the results obtained to factorize the number 15 using a compiled version of Shor's algorithm in a photonic chip.

This Chapter is based on the results published in the following article:

A. Politi, J. C. F. Matthews, J. L. O'Brien, Shor's Quantum Factoring Algorithm on a Photonic Chip, *Science*, **325**, 1221 (2009).

8.1 Experimental details

Experimentally, the qubits were prepared generating four photons simultaneously via spontaneous parametric down conversion. Two individual pairs of 790nm photons were collected from four points of the down-conversion cone and incident onto the chip and collected from the chip with butt-coupled arrays of optical fibre. To ensure good indistinguishability for the photons, 3 different filters with a bandwidth of 2nm were used. The source scheme is shown in figure 8.1.

The first pair is collected in the left-right points of the cone and one filter is used for each point. The second pair of photons is collected in the up-down part of the cone, and for this photons a single filter is used for both the collection points. This apparently complicated scheme was chosen to obtain the best performances from the integrated optical circuit, thus working at a wavelength of 790nm. Given the difficulty in obtaining good filters at this wavelength, tilted interference filters centered at 808nm were used. The scheme adopted ensured good photon filtering for the chosen working wavelength.

The coincidental detections of single photons after the propagation through

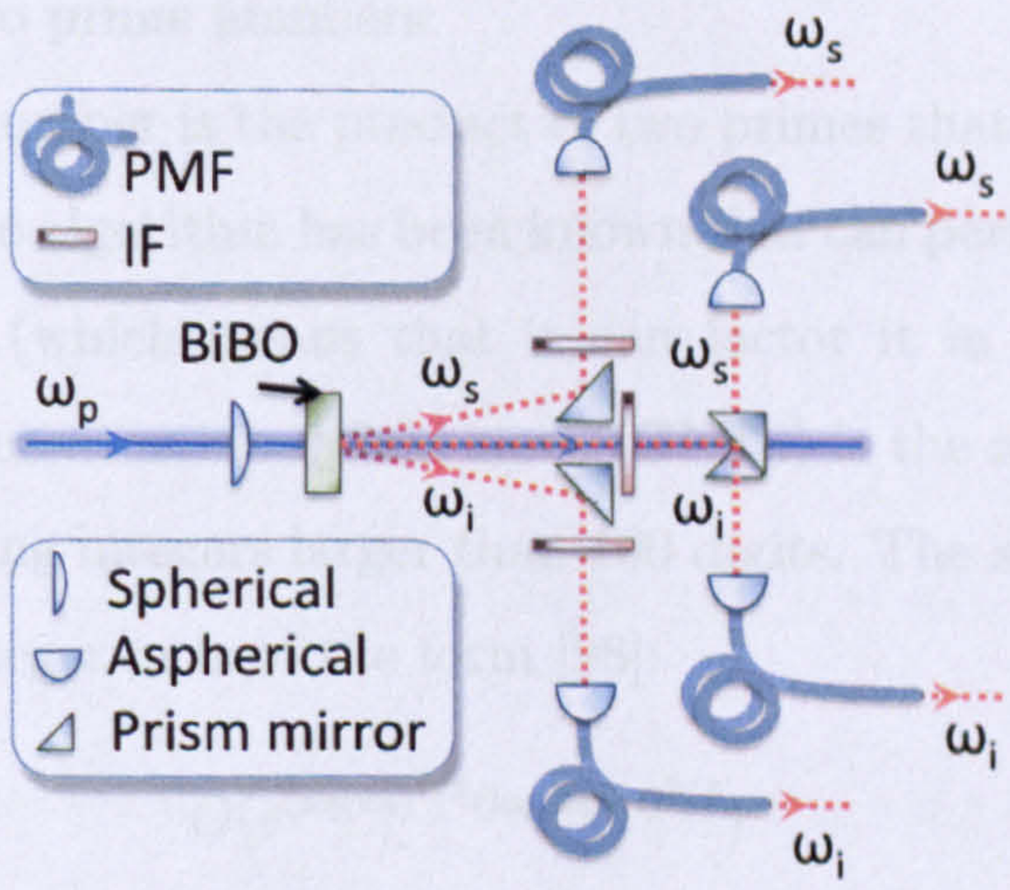

Figure 8.1: Schematic of the source of single photons obtained by parametric down-conversion used to study the integrated photonic implementation of Shor's algorithm.

the integrated chip were computed by a FPGA counting card. This card has been programmed by members of the Bristol group (in particular by Alastair Lynch under the supervision of Prof. John Rarity, and by Damien Bonneau).

8.2 Factorization of prime numbers

Given an integer number, prime factorization is the problem of finding its smaller non-trivial divisors, which when multiplied together equal the original number. By the fundamental theorem of arithmetic, every positive integer greater than one has a unique prime factorization. However, the fundamental theorem of arithmetic does not provide the procedure to obtain the factorization, but it only guarantees the existence of the prime factors.

While there exist a number of algorithms to factorize integer numbers, no efficient algorithm is known for very large numbers, in the sense that the number of operations in the algorithm to achieve the task grows exponentially with the size of the number to factorize. Also, not all numbers of a given length are equally hard to factor. The hardest task is found in the case of semiprimes, which correspond to the product of two prime numbers.

If a large m-bit number is the product of two primes that are approximately of the same size, then no algorithm has been known that can perform the computation in polynomial time (which means that it can factor it in time $O(b^k)$ for some constant k). The general number field sieve (GNFS) is the most efficient classical algorithm for factoring integers larger than 100 digits. The scaling of the required time to factor an integer m is of the form [98]:

$$O(e^{(\log m)^{1/3}(\log\log m)^{2/3}}) \tag{8.1}$$

To give an example of the complexity of the problem, in 2010 the factorization of a 232-digit number utilizing hundreds of machines over a span of 2 years was reported. The computation required more than 10^{20} operations, with the equivalent of almost 2000 years of computing on a single core 2.2GHz AMD Opteron [99].

8.2. Factorization of prime numbers

The difficulty in factorizing large numbers is widely used for cryptographic purposes. These schemes, as the RSA protocol [100], relies on the fact that the multiplication and division of two numbers is an easy task to compute, but the factorization of the number is an hard one. The RSA scheme is commonly used for secure transmission of data over the internet. However, the discovery of an efficient algorithm to factorize large numbers can turn the modern public-key cryptography insecure. This is the reason why the research on the development and possible implementation of a scheme that would change the face of cryptography is considered fundamental by a number of agencies and companies.

8.2.1 Shor's algorithm

In 1994, Peter Shor proposed a quantum algorithm capable of factorizing a number in its prime factors more efficiently that any known classical algorithm [6, 101]. In particular, it scales polynomially with the number of digits, as $O((logN)^3)$. The algorithm proposed by Shor generated much excitement in quantum computation, thanks to the possibility of breaking RSA protocols.

The algorithm to factorize the number N is based in Euler's theorem: for all coprime integers a and N, there exists a least power r known as the order of a modulo N, such that both $a^r \equiv 1 \bmod N$ and $1 \leq r < N$. Provided r is even, then it follows that $a^r - 1 = \left(a^{r/2} - 1\right)\left(a^{r/2} + 1\right) \equiv 0 \bmod N$, implying N divides the product $\left(a^{r/2} - 1\right)\left(a^{r/2} + 1\right)$. Since r is the order of a modulo N, and provided $a^{r/2} \neq -1 \bmod N$, then it follows the factors of N must each divide $\left(a^{r/2} - 1\right)$ and $\left(a^{r/2} + 1\right)$. This therefore implies the factors of N are given by the greatest common divisors of N and $\left(a^{r/2} \pm 1\right)$.

The algorithm can be decomposed in the following steps [5]:

1. if N is even return the factor 2

2. determine, with classical computation (efficient schemes are known) if $N = a^b$, it this is the case, return the factor a

3. Pick a random number $a < N - 1$

4. Compute the greatest common divisor gcd(a, N), for example with Euclid's algorithm. If gcd$(a, N) > 1$, then there is a non-trivial factor of N

5. use the period-finding subroutine to find the period r of a modulo N, that is the smallest positive integer r for which $a^x \bmod N = f(x) = f(x + r)$.

6. If r is odd, the algorithm fails and we have to restart from step 1.

7. If $(a^{r/2} = -1(\mathrm{mod}N)$, go back to step 1.

8. test if gcd$(a^{r/2} \pm 1, N)$ are a nontrivial factor of N.

The most challenging part of Shor's algorithm, requiring the power of quantum computation, is to perform step 5, finding the order r of some randomly chosen coprime a of N. This is the so-called Quantum order-finding routine, that relies upon the entanglement and superposition across two registers of qubits (the argument x_i and function f_i registers of $s = 2\log_2 N$ and $t = 2\log_2 N$ qubits) to compute the modular exponential function (MEF) $a^x \bmod N$. In detail, the first register is set to the superposition of all the n-qubit computational basis, and on the second register is applied the MEF unitary transformation, to produce the state

$$\frac{1}{\sqrt{2^s}} \sum_{x=0}^{2^s-1} |x\rangle \, |a^x \bmod N\rangle \tag{8.2}$$

This state is highly entangled as all the 2^n input value x are entangled with the corresponding value of $f(x)$ at the same time. At this stage, the quantum Fourier transformation (QFT) can be applied on the first register, to obtain

$$\frac{1}{2^s} \sum_{x=0}^{2^s-1} \sum_{y=0}^{2^s-1} e^{2i\pi xy} \, |y\rangle \, |a^x \bmod N\rangle \, . \tag{8.3}$$

In this state, the interference between the components leads to peaks in amplitude for terms argument qubits with $y = c2^s = r$ (for integer c). In this case, the period of the MEF r can be deduced with high probability.

The Quantum order-finding routine works in a runtime $O((logN)^3)$, and so the entire Shor's algorithm. As noted in the steps 5-7 of the algorithm, the computation can fail, depending on the starting number and the random choices, but the probability of success is of the order $O(1)$, so after enough iterations the computation gives the expected outcome with arbitrary high probability.

8.3 Compiled Shor's algorithm

Shors algorithm to factorize a number composed of m bits requires $72m^3$ elementary quantum gates and $5m + 1$; for example, factoring 15, requires 4608 gates operating on 21 qubits [102]. These numbers are lower bounds in the requirements, since they do not take into account any error correction scheme that has to be implemented in any real (non-perfect) quantum computers. Unfortunately, this is unfeasible in any current technology (not just photons). There is, however a method to overcome this complications if one accepts to realize a non-scalable version of the algorithm [102]. This "compiled" version of the algorithm take advantages from the properties of the number to be factored, allowing the implementation of the computation with a reduced number of resources.

A compiled version of Shor's algorithm was implemented in a liquid NMR architecture [103]. However, given the high level of mixture for the quantum state [104], neither the entanglement nor the coherent control at the core of Shors algorithm can be implemented or verified in this architecture.

Compiled versions of Shor's algorithm have been demonstrated to factorize 15 using linear optics [105, 106]. In both of these experiments, the presence of entanglement is demonstrated during the computation, thus providing a working proof of principle of the quantum algorithm.

The studied compiled version of Shor's algorithm computes the prime factor of 15 when the coprime $a = 2$ is chosen. The circuit required to implement the hard part of the computation is shown in figure 8.2. The compilation reduces the required number of function qubits (f_i) by evaluating $\log_a[a^z \bmod N]$ in place of

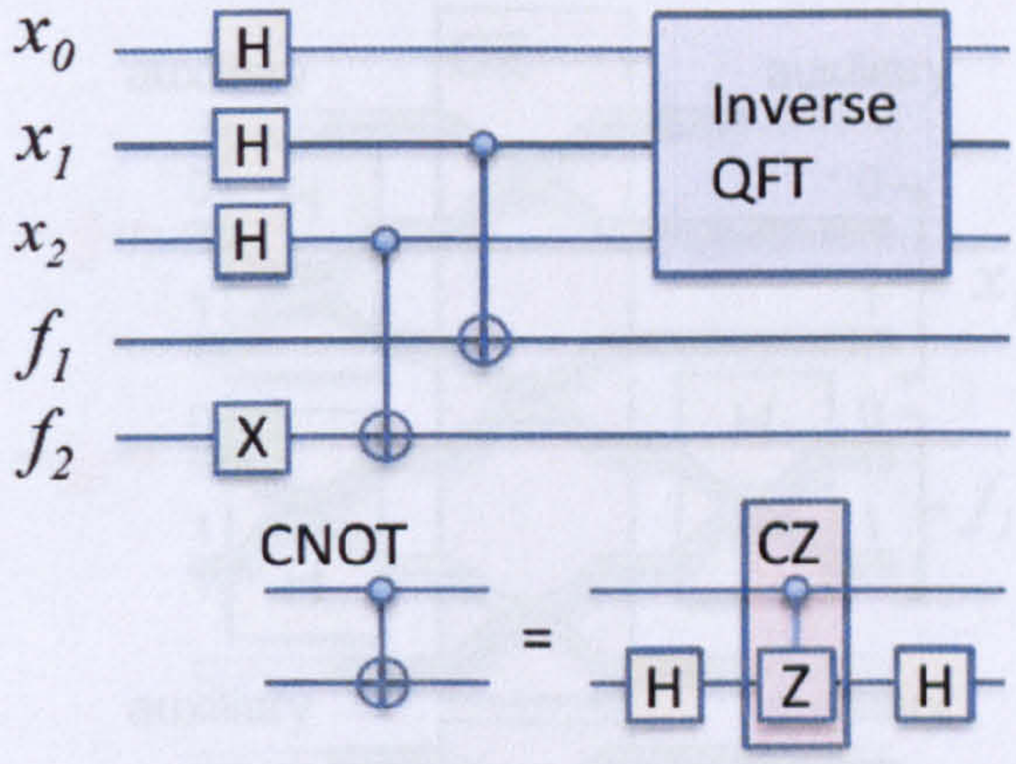

Figure 8.2: Compiled version of Shor's algorithm to factorize 15. The initial single qubit operations prepare the register in the superposition state, while the two-qubit gates perform the MEF operation.

$a^z x \bmod N$; reducing the number of function qubits from $\log_a[N]$ to $\log_2[\log_a[N]]$. Another simplification can be obtained by noting that the Inverse QFT shown in figure 8.2 does not need to be implemented in the quantum circuit for the present case (nor for any $r = 2^l, l \in \mathbb{N}$), and can be performed by classical processing.

8.4 Shors algorithm on a Photonic Chip

The circuit described in the previous Section can be translated in an integrated optical network by using the components described in this Thesis. Figure 8.3 shows the integrated circuit that implement the quantum computation required to factorize 15 when $a = 2$ is chosen.

The scheme employed within the device proceeds with the input states initialized in the "0" state, apart from the lower photon in figure 8.3 that is initiated in the state "1" (this implements the X-gate present on that qubit). This algorithm used five qubits, one of which is a redundant qubit that remains in the "0" state throughout. The two control qubits of each gate (x_2 and x_2) form the argument register of the algorithm while the target qubits (f_1 and $f2$) form the function register of the algorithm. The Hadamard operations, performed by the first beam

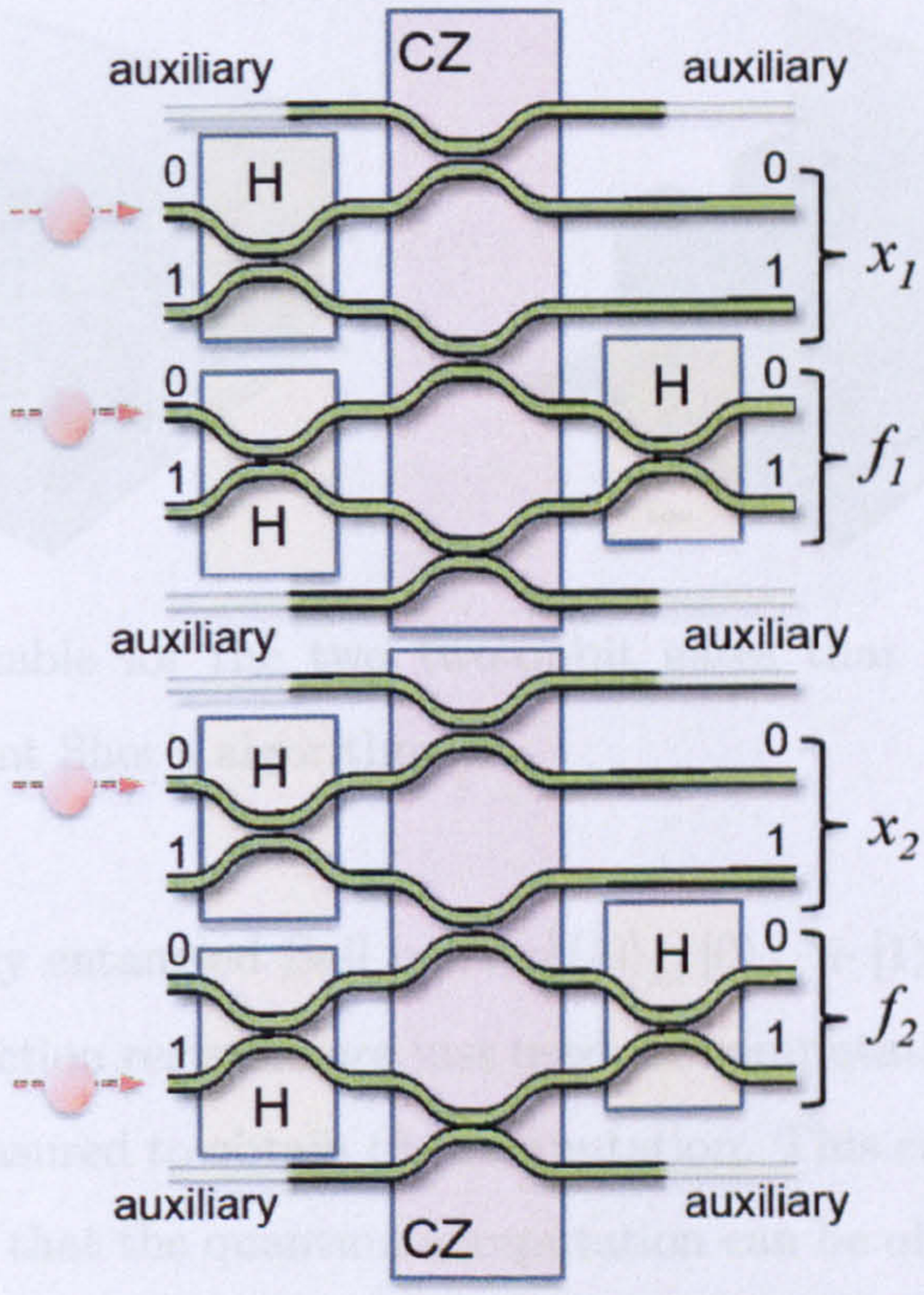

Figure 8.3: Schematic of the layout of the integrated photonic device that perform the quantum Shor's algorithm.

splitters in each control mode, prepare the control qubits in equal superposition of the "0" and "1" states. The action of the C-NOT gate is to entangle the control and target qubits. Tracing out the two target qubits therefore yields the maximally mixed state across the control qubits.

The optical circuit required to implement Shor's algorithm is composed by two independent CNOT gate and single qubit operations. For each these two-qubit gates similarities of S= 88 ± 1% and S= 89 ± 1% were measured to characterize the integrated network (see figure 8.4). The above values are not as high as in the case of the measurements reported in the previous Chapter. This has to be ascribed to the non-optimal spectral properties of the photons injected in the circuit. The realization of Shor's algorithm was studied by inputting the state $|\psi_{in}\rangle = |0\rangle_{x1} |0\rangle_{x2} |0\rangle_{f1} |1\rangle_{f2}$. In this case, the circuit is designed to produce a prod-

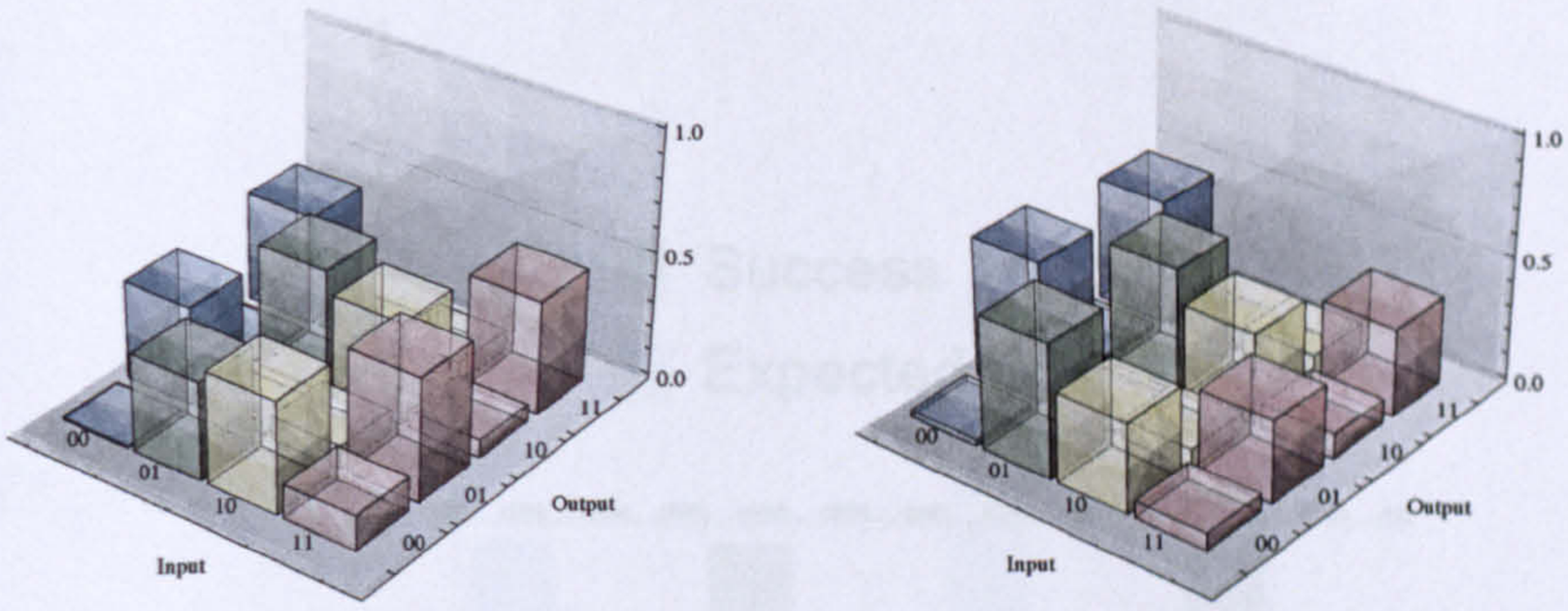

Figure 8.4: Truth-table for the two two-qubit gates that compose the optical network to implement Shor's algorithm.

uct of two maximally entangled Bell pairs: $\frac{1}{2}(|0\rangle_{x1}|0\rangle_{f1} + |1\rangle_{x1}|1\rangle_{f1})(|0\rangle_{x1}|1\rangle_{f1} + |1\rangle_{x1}|0\rangle_{f1})$. The function registers are just used for computation purpose, and are, in principle, not measured to obtain the computation. This corresponds to tracing out the f_i qubits, so that the quantum computation can be obtained by measuring the x_i qubits in the computational basis. Since the CNOT gates used to implement the computation work in a probabilistic way, the presence of one photon in the control (function register) waveguides have to be monitored. The tracing out of the function register is obtained discarding the information about the outcome for those qubits. The experimental output statistics form the algorithm is given in figure 8.5.

On combining the two bit output of this quantum process with the fifth redundant qubit in the zero state, The classical outputs of the measurement in the logical basis consists of the outcomes "000", "010", "100" and "110". These 3-bit numbers correspond to the values $0, 2, 4$ and 6, respectively. The first number is an expected failure inherent to Shor's algorithm, while the third yields the trivial factors 1 and 15. The second and fourth outcomes allow the calculation of the order $r = 4$, which via Euclid's classical algorithm efficiently yields the correct prime factors 3 and 5. This routine by itself has a success rate of $1/2$; on repeating n times it yields an overall success rate of $1 - (1/2)^n$.

The measured state has a similarity of $99 \pm 1\%$ with the ideal distribution,

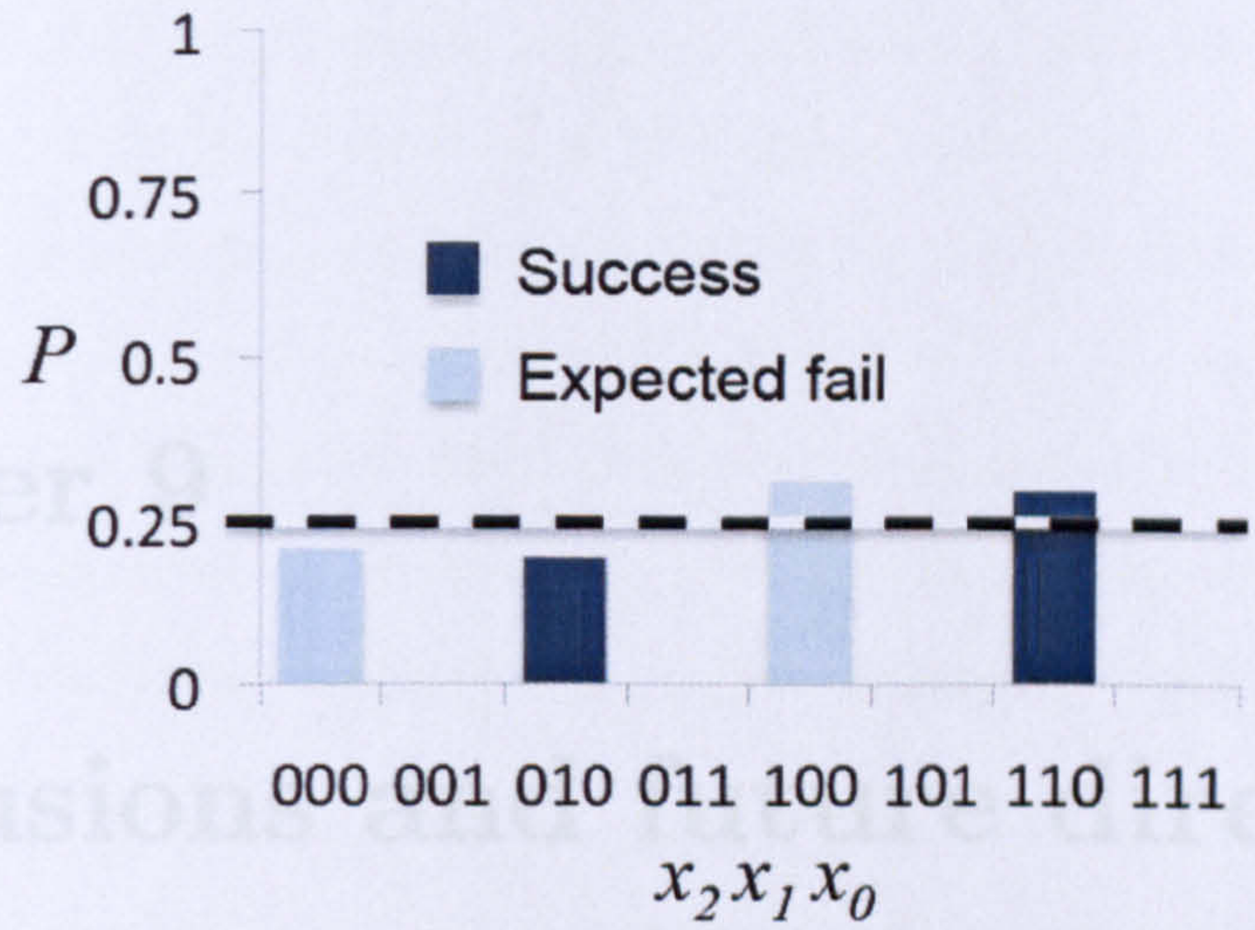

Figure 8.5: Measured outcomes in the computational basis for the integrated optics implementation on the compiled Shor's algorithm. The dashed line corresponds to the expected value for the four experimental peaks "000", "010", "100" and "110"; the expected values for the other outcomes corresponds to zero.

consisting of four equal peaks for the "000", "010", "100" and "110" outcomes. As explained in reference [106], it is interesting to note that the fidelity between the measured and the expected state is close to unity even if the experimental scheme relies of imperfect components. This behavior can be partially explained considering the fact that the fidelity between states contains partial information about the gates, so, in some non-rigorous sense, it is forgiving some error in the gates implementation.

Chapter 9

Conclusions and future directions

9.1 Achievements and results

As outlined in this Thesis, during the period of my PhD I worked to develop the components needed for Quantum Information processing in photonic structures. With my colleagues in Bristol University, we developed and tested the optical platform in silica-on-silicon technology. The results of this work can be summarized in the points below:

1. Simulations and design of all the waveguide components required for quantum optics applications in silica-on-silicon. I studied: guiding properties, bends, directional couplers, multi-mode interference couplers, phase controllers. The polarization control in the integrated device was analyzed, but, given the properties of the material, no polarization diversity devices were designed in silica-on-silicon waveguides.

2. Test of non-classical properties of the fabricated devices. Two-photon HOM dip experiments were performed on the directional couplers, obtaining near-unity visibility and good reproducibility of the results. Non-classical interference was measured also in MMI couplers, obtaining high visibility. The guiding properties of the MMI caused a reduction of non-classical interference given by the multi-mode structure of the samples.

3. Control of the optical phase of quantum states inside the integrated chip using resistive heater controllers. The phase control was tested to give high performance with single qubits, thus allowing the architecture to implement arbitrary single qubit operations with high fidelity. The same phase control can be used to manipulate multi-photon entangled states useful for quantum metrology applications. In general, the integrated components can be used to build an arbitrary multi-photon, multi-channel circuit for quantum optic applications.

4. Characterization of two-qubit entangling gates needed for quantum information. Probabilistic CNOT gates were fabricated and tested, providing high fidelity operation. The quality of the gates promises an operation quality in the range required to obtain fault tolerant operations for quantum information.

5. Realization of a simple quantum algorithm by integrating the above components on a photonic chip. A compiled version of Shor's algorithm was realized to factorize the number 15. The results obtained from this circuit demonstrate that the integrated optics architecture is very promising to obtain future quantum information devices.

Moreover, with the collaborators of MacQuarie University we developed integrated quantum circuits with directly-written waveguides in glass. We tested the fabricated devices, showing very promising results, particularly considering the capability of the direct-write technology of producing 3D optical circuits.

All the results presented in this Thesis encourage the research in quantum photonic. This approach promises to be the basis for the development of quantum optics platforms for future quantum information science demonstrations with photons [107].

9.2 Outlook

The results presented in this Thesis are the first demonstrations of quantum information science experiments using an integrated waveguide platform. The majority of the devices investigated were fabricated using well established processing techniques of Silica-on silicon. This was originally developed for the mass fabrication of components for telecommunication purposes. Although the silica-on-silicon material system is an excellent choice for the first integrated devices, future integrated quantum photonic circuits will take advantage of the wide range of material systems currently available for the fabrication of classical photonic devices.

The first goal for the next generation of quantum photonic devices will be to increase the component density on a single chip. A further challenge will be to add functionality and integrating both active and passive elements onto a single device. The goal is to achieve a fully integrated quantum photonic circuit; a single device that comprises single photon emitters, quantum logic processing circuits and single photon detectors all integrated onto a single chip.

Circuits with a high component density are crucial for the realization of quantum circuits with complex functionalities. For this purpose, material systems that allow the fabrication of waveguides with high refractive index contrasts (such as InP, GaAs or silicon allow) will likely be a sensible choice. The higher confinement given by the refractive index contrast in these materials imply low losses even in case of very small bend radius, thus removing a bottleneck to achieve ultra-compact circuits. A further increase of the density of photonic components can be achieved using photonic crystal structures. These represent are the ultimate approach to reduce the device size, since the propagation of the light is controlled thanks to features of the dimensions of the wavelength [108, 109].

Photolithographic technologies used to fabricate photonic devices are normally restricted to waveguide structures in two dimensions (planar structures). One of the possible approaches to increase the complexity of photonic circuits is to move to schemes where also the third dimension is used. Direct-write laser waveguide tech-

nologies give the opportunity to fabricate such 3D structures, simply by changing the focal depth of the laser in the writing process. Moreover, the direct-write technique can be used in conjunction with a wide range of material systems, allowing rapid fabrication of complex 3D waveguide networks with different characteristics. In Chapter 5, I presented the first results regarding direct-write waveguides for quantum information applications. Additional results obtained from quantum experiments in planar directly-written waveguides have been recently demonstrated [110]. The implementation of more complicated circuits, in 3D structures and maybe in different materials from glass, will probably play an important role in future quantum optics demonstrations.

The possibility of accurately control phases directly on-chip, and of reconfiguring the circuit is a key requirements for the implementation of versatile quantum photonic devices. In this thesis it was demonstrated phase controlling using thermo-optical effect in silica. This approach can be useful when slow reconfigurations are needed, but different materials have to be used to offer fast, low-power switches. A promising alternative to silica is Lithium Niobate ($LiNbO_3$), since it offers low loss waveguide structures and exhibits an electro-optic effect, which allows for fast control over the refractive index (over 10's GHz) [111]. Moreover $LiNbO_3$ offer the possibility to control polarization within waveguide structures [112]. Such fast nonlinearity will be required applications demanding fast switching, such as adaptive circuits for quantum control and feedforward, as in cluster-state quantum computation [46]. In addition, periodically-poled $LiNbO_3$ can be used for efficient single photon generation through parametric down conversion, poled waveguides are therefore an ideal source of single photons for integration with waveguide circuits [113].

The full potential of the integration approach for quantum information will be available when it will be possible to integrate all the elements needed on a single chip: waveguides, active elements, sources, detectors (and possibly systems for light-matter interactions [114, 115]). Integrated single photon sources could be realized through non-linear phenomena in waveguides, such as spontaneous para-

metric down conversion [113], and true single photon sources, like quantum dots [116] and color center sources [117]. Photon number resolving detectors could be implemented through integrated avalanche photodiodes [118] or integrated superconducting detectors [119]. A device that incorporates all of these components will enable new scientific developments in the field of quantum optics, as well as the development of advanced quantum systems for the purposes of quantum metrology, quantum communications and quantum computation.

Bibliography

[1] International Technology Roadmap for Microelectronics (ITRS), http://www.itrs.net/.

[2] N. Kim, T. Austin, D. Baauw, T. Mudge, K. Flautner, J. Hu, M. Irwin, M. Kandemir, and V. Narayanan, "Leakage current: Moore's law meets static power," *Computer*, vol. 36, no. 12, pp. 68–75, Dec. 2003.

[3] C. K. Hong, Z. Y. Ou, and L. Mandel, "Measurement of subpicosecond time intervals between two photons by interference," *Phys. Rev. Lett.*, vol. 59, pp. 2044–2046, 1987.

[4] G. E. Moore, "Cramming more components onto integrated circuits," *Electronics*, vol. 38, no. 8, p. 4, Apr. 1965.

[5] M. A. Nielsen and I. L. Chuang, *Quantum Computation and Quantum Information.* Cambridge University Press, 2000.

[6] P. W. Shor, *Proc. 35th Annu. Symp. Foundations of Computer Science and IEEE Computer Society and Los Alamitos and CA*, pp. 124–134, 1994, ed. S. Goldwasser.

[7] D. P. DiVincenzo and D. Loss, "Quantum information is physical," *Superlatt. Micro.*, vol. 23, pp. 419–432, 1998.

[8] J. L. O'Brien, "Optical Quantum Computing," *Science*, vol. 318, no. 5856, pp. 1567–1570, 2007.

[9] P. Kok, W. J. Munro, K. Nemoto, T. C. Ralph, J. P. Dowling, and G. J. Milburn, "Linear optical quantum computing with photonic qubits," *Reviews of Modern Physics*, vol. 79, no. 1, p. 135, 2007.

[10] P. G. Kwiat, K. Mattle, H. Weinfurter, A. Zeilinger, A. V. Sergienko, and Y. Shih, "New high-intensity source of polarization-entangled photon pairs," *Phys. Rev. Lett.*, vol. 75, no. 24, pp. 4337–4341, Dec 1995.

[11] J. Brendel, N. Gisin, W. Tittel, and H. Zbinden, "Pulsed energy-time entangled twin-photon source for quantum communication," *Phys. Rev. Lett.*, vol. 82, no. 12, pp. 2594–2597, Mar 1999.

[12] A. Mair, A. Vaziri, G. Weihs, and A. Zeilinger, "Entanglement of the orbital angular momentum states of photons," *Nature*, vol. 412, no. 6844, pp. 313–316, JUL 19 2001.

[13] E. Knill, R. Laflamme, and G. J. Milburn, "A scheme for efficient quantum computation with linear optics," *Nature*, vol. 409, pp. 46–52, 2001.

[14] C. H. Bennett, G. Brassard, C. Crépeau, R. Jozsa, A. Peres, and W. K. Wootters, "Teleporting an unknown quantum state via dual classical and einstein-podolsky-rosen channels," *Phys. Rev. Lett.*, vol. 70, no. 13, pp. 1895–1899, Mar 1993.

[15] D. Boschi, S. Branca, F. De Martini, L. Hardy, and S. Popescu, "Experimental realization of teleporting an unknown pure quantum state via dual classical and einstein-podolsky-rosen channels," *Phys. Rev. Lett.*, vol. 80, no. 6, pp. 1121–1125, Feb 1998.

[16] D. Bouwmeester, J.-W. Pan, K. Mattle, M. Eibl, H. Weinfurter, and A. Zeilinger, "Experimental quantum teleportation," *Nature*, vol. 390, pp. 575–579, 1997.

[17] J. L. O'Brien, G. J. Pryde, A. G. White, T. C. Ralph, and D. Branning,

"Demonstration of an all-optical quantum controlled-NOT gate," *Nature*, vol. 426, no. 6964, pp. 264–267, 2003.

[18] J. L. O'Brien, G. J. Pryde, A. Gilchrist, D. F. V. James, N. K. Langford, T. C. Ralph, and A. G. White, "Quantum process tomography of a controlled-NOT gate," *Phys. Rev. Lett.*, vol. 93, no. 8, p. 080502, 2004.

[19] N. K. Langford, T. J. Weinhold, R. Prevedel, K. J. Resch, A. Gilchrist, J. L. O'Brien, G. J. Pryde, and A. G. White, "Demonstration of a simple entangling optical gate and its use in bell-state analysis," *Phys. Rev. Lett.*, vol. 95, no. 21, p. 210504, 2005.

[20] N. Kiesel, C. Schmid, U. Weber, R. Ursin, and H. Weinfurter, "Linear optics controlled-phase gate made simple," *Phys. Rev. Lett.*, vol. 95, no. 21, p. 210505, 2005.

[21] R. Okamoto, H. F. Hofmann, S. Takeuchi, and K. Sasaki, "Demonstration of an optical quantum controlled-not gate without path interference," *Phys. Rev. Lett.*, vol. 95, no. 21, p. 210506, 2005.

[22] K. Kieling, T. Rudolph, and J. Eisert, "Percolation, renormalization, and quantum computing with nondeterministic gates," *Physical Review Letters*, vol. 99, no. 13, p. 130501, 2007.

[23] R. Raussendorf and H. J. Briegel, "A one-way quantum computer," *Phys. Rev. Lett.*, vol. 86, p. 5188, 2001.

[24] D. E. Browne and T. Rudolph, "Resource-efficient linear optical quantum computation," *Phys. Rev. Lett.*, vol. 95, no. 1, p. 010501, 2005.

[25] M. A. Nielsen, "Optical quantum computation using cluster states," *Phys. Rev. Lett.*, vol. 93, no. 4, p. 040503, 2004.

[26] P. Walther, K. J. Resch, T. Rudolph, E. Schenck, H. Weinfurter, V. Vedral,

M. Aspelmeyer, and A. Zeilinger, "Experimental one-way quantum computing," *Nature*, vol. 434, no. 7030, pp. 169–176, 2005.

[27] M. O. Scully and M. S. Zubairy, *Quantum Optics*. Cambridge University Press, 1997.

[28] V. Giovannetti, S. Lloyd, and L. Maccone, "Quantum metrology," *Phys. Rev. Lett.*, vol. 96, no. 1, p. 010401, 2006.

[29] ——, "Quantum-enhanced measurements: Beating the standard quantum limit," *Science*, vol. 306, p. 1330, 2004.

[30] K. Banaszek, R. Demkowicz-Dobrzanski, and I. A. Walmsley, "Quantum states made to measure," *Nature Photonics*, vol. 3, no. 12, pp. 673-676, DEC 2009.

[31] H. Lee, P. Kok, and J. Dowling, "A quantum rosetta stone for interferometry," *J. Mod. Opt.*, vol. 49, no. 14-15, pp. 2325–2338, 2002.

[32] M. Born and E. Wolf, *Principles of Optics: Electromagnetic Theory of Propagation, Interference and Diffraction of Light*, 7th ed. Cambridge University Press, 1999.

[33] J. D. Jackson, *Classical Electrodynamics*, 3rd ed. Wiley, 1998.

[34] G. Lifante, *Integrated Photonics: Fundamentals*. Wiley, 2003.

[35] K. Kato, M. Ishii, and Y. Inoue, "Packaging of large-scale planar lightwave circuits," *Components, Packaging, and Manufacturing Technology, Part B: Advanced Packaging, IEEE Transactions on*, vol. 21, no. 2, pp. 121–129, May 1998.

[36] M. Kawachi, "Silica waveguides on silicon and their application to integrated-optic components," *Optical and Quantum Electronics*, vol. 22, no. 5, pp. 391–416, SEP 1990.

[37] T. Honjo, K. Inoue, and H. Takahashi, "Differential-phase-shift quantum key distribution experiment with aplanar light-wave circuit mach-zehnder interferometer," *Opt. Lett.*, vol. 29, no. 23, pp. 2797–2799, 2004.

[38] H. Takesue and K. Inoue, "Generation of $1.5-\mu m$ band time-bin entanglement using spontaneous fiber four-wave mixing and planar light-wave circuit interferometers," *Phys. Rev. A*, vol. 72, no. 4, p. 041804, Oct 2005.

[39] D. Marcuse, "Bend loss of slab and fiber modes computed with diffraction theory," *Quantum Electronics, IEEE Journal of*, vol. 29, no. 12, pp. 2957–2961, Dec 1993.

[40] D. H. Naghski, J. T. Boyd, H. E. Jackson, and A. J. Steckl, "Potential for size reduction of algaas optical channel waveguide structures fabricated by focused ion beam implantation and oxidation," *Optics Communications*, vol. 150, no. 1-6, pp. 97 – 100, 1998.

[41] O. Bryngdahl, "Image formation using self-imaging techniques," *J. Opt. Soc. Am.*, vol. 63, no. 4, pp. 416–419, 1973.

[42] L. Soldano and E. Pennings, "Optical multi-mode interference devices based on self-imaging: principles and applications," *Lightwave Technology, Journal of*, vol. 13, no. 4, pp. 615–627, Apr 1995.

[43] R. Ulrich, "Light-propagation and imaging in planar optical waveguides," *Nouvelle Revue d'Optique*, vol. 6, no. 5, p. 253, 1975.

[44] M. Bachmann, P. A. Besse, and H. Melchior, "General self-imaging properties in n × n multimode interference couplers including phase relations," *Appl. Opt.*, vol. 33, no. 18, pp. 3905–3911, 1994.

[45] T. Grzegorczyk, X. Leijtens, C. Vreeburg, F. Groen, I. Moerman, E. Metaal, and M. Smit, "Compact mmi-based power dividers with unequal splitting ratio realised on inp/ingaasp," *Proceedings of ECIO '97 : 8th European Conference on Integrated Optics - Stockholm*, pp. 150–153, 1997.

[46] R. Prevedel, P. Walther, F. Tiefenbacher, P. Bohi, R. Kaltenback, T. Jennewein, and A. Zeilinger, "High-speed linear optics quantum computing using active feed-forward," *Nature*, vol. 445, no. 7123, pp. 65–69, 2007.

[47] I. Kenichi and Y. Kokubun, *Encyclopedic Handbook of Integrated Optics*. CRC Press, 2006.

[48] I. Kiyat, A. Aydinli, and N. Dagli, "A compact silicon-on-insulator polarization splitter," *Photonics Technology Letters, IEEE*, vol. 17, no. 1, pp. 100–102, Jan. 2005.

[49] M. R. Watts, H. A. Haus, and E. P. Ippen, "Integrated mode-evolution-based polarization splitter," *Opt. Lett.*, vol. 30, no. 9, pp. 967–969, 2005.

[50] J. V. der Tol, J. Pedersen, E. Metaal, J.-W. V. Gaalen, Y. Oei, and F. Groen, "A short polarization splitter without metal overlays on ingaasp-inp," *Photonics Technology Letters, IEEE*, vol. 9, no. 2, pp. 209–211, Feb. 1997.

[51] L. M. Augustin, J. J. G. M. van der Tol, R. Hanfoug, W. J. M. de Laat, M. J. E. van de Moosdijk, P. W. L. van Dijk, Y.-S. Oei, and M. K. Smit, "A single etch-step fabrication-tolerant polarization splitter," *J. Lightwave Technol.*, vol. 25, no. 3, pp. 740–746, 2007.

[52] P. Albrecht, M. Hamacher, H. Heidrich, D. Hoffmann, H. Nolting, and C. Weinert, "Te/tm mode splitters on ingaasp/inp," *Photonics Technology Letters, IEEE*, vol. 2, no. 2, pp. 114–115, Feb 1990.

[53] P. P. Rohde, G. J. Pryde, J. L. O'Brien, and T. C. Ralph, "Quantum-gate characterization in an extended hilbert space," *Phys. Rev. A*, vol. 72, no. 3, p. 032306, 2005.

[54] K. Mattle, M. Michler, H. Weinfurter, A. Zeilinger, and M. Zukowski, "Nonclassical statistics at multiport beam splitter," *Applied Physics B: Lasers and Optics*, vol. 60, no. 2-3, Suppl. S, p. S111, 1995.

[55] G. Weihs, M. Reck, H. Weinfurter, and A. Zeilinger, "Two-photon interference in optical fiber multiports," *Phys. Rev. A*, vol. 54, no. 1, pp. 893–897, Jul 1996.

[56] ——, "All-fiber three-path mach—zehnder interferometer," *Opt. Lett.*, vol. 21, no. 4, pp. 302–304, 1996.

[57] R. R. Gattass and E. Mazur, "Femtosecond laser micromachining in transparent materials," *Nature Photon.*, vol. 2, no. 4, pp. 219–225, 2008.

[58] W. Yang, P. G. Kazansky, and Y. P. Svirko, "Non-reciprocal ultrafast laser writing," *Nature Photon.*, vol. 2, no. 2, pp. 99–104, 2008.

[59] K. M. Davis, K. Miura, N. Sugimoto, and K. Hirao, "Writing waveguides in glass with a femtosecond laser," *Opt. Lett.*, vol. 21, no. 21, p. 1729, 1996.

[60] R. Osellame, V. Maselli, R. M. Vazquez, R. Ramponi, and G. Cerullo, "Integration of optical waveguides and microfluidic channels both fabricated by femtosecond laser irradiation," *Appl. Phys. Lett.*, vol. 90, no. 23, p. 231118, 2007.

[61] G. D. Marshall, M. Ams, and M. J. Withford, "Direct laser written waveguide-bragg gratings in bulk fused silica," *Opt. Lett.*, vol. 31, no. 18, pp. 2690–2691, 2006.

[62] G. D. Marshall, P. Dekker, M. Ams, J. A. Piper, and M. J. Withford, "Directly written monolithic waveguide laser incorporating a distributed feedback waveguide-bragg grating," *Opt. Lett.*, vol. 33, no. 9, pp. 956–958, 2008.

[63] J. W. Chan, T. R. Huser, S. H. Risbud, and D. M. Krol, "Modification of the fused silica glass network associated with waveguide fabrication using femtosecond laser pulses," *Appl. Phys. A*, vol. 76, no. 3, pp. 367–372, 2003.

[64] D. J. Little, M. Ams, P. Dekker, G. D. Marshall, J. M. Dawes, and M. J. Withford, "Femtosecond laser modification of fused silica: the effect of writ-

ing polarization on si-o ring structure," *Opt. Express*, vol. 16, no. 24, pp. 20 029–20 037, 2008.

[65] M. Ams, G. D. Marshall, D. J. Spence, and M. J. Withford, "Slit beam shaping method for femtosecond laser direct-write fabrication of symmetric waveguides in bulk glasses," *Optics Express*, vol. 13, no. 15, pp. 5676–5681, 2005.

[66] M. Ams, G. D. Marshall, and M. J. Withford, "Study of the influence of femtosecond laser polarisation on direct writing of waveguides," *Optics Express*, vol. 14, no. 26, pp. 13 158–13 163, 2006.

[67] K. Sanaka, T. Jennewein, J.-W. Pan, K. Resch, and A. Zeilinger, "Experimental nonlinear sign shift for linear optics quantum computation," *Phys. Rev. Lett.*, vol. 92, no. 1, p. 017902, Jan 2004.

[68] B. H. Liu, F. W. Sun, Y. X. Gong, Y. F. Huang, Z. Y. Ou, and G. C. Guo, "Demonstration of the three-photon de broglie wavelength by projection measurement," *Phys. Rev. A*, vol. 77, no. 2, p. 023815, 2008.

[69] K. Sanaka, K. J. Resch, and A. Zeilinger, "Filtering out photonic fock states," *Phys. Rev. Lett.*, vol. 96, no. 8, p. 083601, 2006.

[70] K. J. Resch, J. L. O'Brien, T. J. Weinhold, K. Sanaka, B. P. Lanyon, N. K. Langford, and A. G. White, "Entanglement generation by fock-state filtration," *Phys. Rev. Lett.*, vol. 98, no. 20, p. 203602, 2007.

[71] H. F. Hofmann and S. Takeuchi, "Quantum filter for nonlocal polarization properties of photonic qubits," *Phys. Rev. Lett.*, vol. 88, no. 14, p. 147901, Mar 2002.

[72] R. Okamoto, J. L. O'Brien, H. F. Hofmann, T. Nagata, K. Sasaki, and S. Takeuchi, "An Entanglement Filter," *Science*, vol. 323, no. 5913, pp. 483–485, 2009.

[73] B. P. Lanyon, T. J. Weinhold, N. K. Langford, J. L. O'Brien, K. J. Resch, A. Gilchrist, and A. G. White, "Manipulating biphotonic qutrits," *Phys. Rev. Lett.*, vol. 100, no. 6, p. 060504, 2008.

[74] M. A. Nielsen and I. L. Chuang, *Quantum Computation and Quantum Information*. Cambridge University Press, October 2000.

[75] M. Reck, A. Zeilinger, H. J. Bernstein, and P. Bertani, "Experimental realization of any discrete unitary operator," *Phys. Rev. Lett.*, vol. 73, no. 1, pp. 58–61, Jul 1994.

[76] M. W. Mitchell, J. S. Lundeen, and A. M. Steinberg, "Super-resolving phase measurements with a multiphoton entangled state," *Nature*, vol. 429, no. 6988, pp. 161–164, 2004.

[77] T. Nagata, R. Okamoto, J. L. O'Brien, K. Sasaki, and S. Takeuchi, "Beating the standard quantum limit with four-entangled photons," *Science*, vol. 316, no. 5825, pp. 726–729, 2007.

[78] P. Walther, J.-W. Pan, M. Aspelmeyer, R. Ursin, S. Gasparoni, and A. Zeilinger, "De broglie wavelength of a non-local four-photon state," *Nature*, vol. 429, no. 6988, pp. 158–161, 2004.

[79] Z. Y. Ou, X. Y. Zou, L. J. Wang, and L. Mandel, "Experiment on nonclassical fourth-order interference," *Phys. Rev. A*, vol. 42, no. 5, pp. 2957–2965, Sep 1990.

[80] J. G. Rarity, P. R. Tapster, E. Jakeman, T. Larchuk, R. A. Campos, M. C. Teich, and B. E. A. Saleh, "Two-photon interference in a mach-zehnder interferometer," *Phys. Rev. Lett.*, vol. 65, no. 11, pp. 1348–1351, Sep 1990.

[81] A. Kuzmich and L. Mandel, "Sub-shot-noise interferometric measurements with two-photon states," *Quant. Semiclass. Opt.*, vol. 10, p. 493, 1998.

[82] E. J. S. Fonseca, C. H. Monken, and S. Pádua, "Measurement of the de broglie wavelength of a multiphoton wave packet," *Phys. Rev. Lett.*, vol. 82, no. 14, pp. 2868–2871, Apr 1999.

[83] K. Edamatsu, R. Shimizu, and T. Itoh, "Measurement of the photonic de broglie wavelength of entangled photon pairs generated by spontaneous parametric down-conversion," *Phys. Rev. Lett.*, vol. 89, no. 21, p. 213601, Nov 2002.

[84] H. S. Eisenberg, J. F. Hodelin, G. Khoury, and D. Bouwmeester, "Multiphoton path entanglement by nonlocal bunching," *Phys. Rev. Lett.*, vol. 94, no. 9, p. 090502, 2005.

[85] K. J. Resch, K. L. Pregnell, R. Prevedel, A. Gilchrist, G. J. Pryde, J. L. O'Brien, and A. G. White, "Time-reversal and super-resolving phase measurements," *Phys. Rev. Lett.*, vol. 98, no. 22, p. 223601, 2007.

[86] R. Okamoto, H. F. Hofmann, T. Nagata, J. L. O'Brien, K. Sasaki, and S. Takeuchi, "Beating the standard quantum limit: phase super-sensitivity of n-photon interferometers," *New J. Phys.*, vol. 10, no. 7, p. 073033, 2008.

[87] O. Steuernagel, "de broglie wavelength reduction for a multiphoton wave packet," *Phys. Rev. A*, vol. 65, no. 3, p. 033820, Feb 2002.

[88] T. C. Ralph, N. K. Langford, T. B. Bell, and A. G. White, "Linear optical controlled-NOT gate in the coincidence basis," *Phys. Rev. A*, vol. 65, p. 062324, 2001.

[89] H. F. Hofmann and S. Takeuchi, "Quantum phase gate for photonic qubits using only beam splitters and postselection," *Phys. Rev. A*, vol. 66, p. 024308, 2001.

[90] G. J. Pryde, J. L. O'Brien, A. G. White, S. D. Bartlett, and T. C. Ralph, "Measuring a photonic qubit without destroying it," *Phys. Rev. Lett.*, vol. 92, p. 190402, 2004.

[91] T. C. Ralph, S. D. Bartlett, J. L. O'Brien, G. J. Pryde, and H. M. Wiseman, "Quantum nondemolition measurements for quantum information," *Phys. Rev. A*, vol. 73, no. 1, p. 012113, 2006.

[92] A. M. Steane, "Error correcting codes in quantum theory," *Phys. Rev. Lett.*, vol. 77, p. 793, 1996.

[93] E. Knill, R. Laflamme, and W. H. Zurek, "Resilient quantum computation: error models and thresholds," *Proc. R. Soc. London A*, vol. 454, p. 365, 1998.

[94] E. Knill, "Quantum computing with realistically noisy devices," *Nature*, vol. 434, no. 7029, pp. 39–44, 2005.

[95] C. M. Dawson, H. L. Haselgrove, and M. A. Nielsen, "Noise thresholds for optical quantum computers," *Phys. Rev. Lett.*, vol. 96, no. 2, p. 020501, Jan 2006.

[96] R. Raussendorf and J. Harrington, "Fault-tolerant quantum computation with high threshold in two dimensions," *Phys. Rev. Lett.*, vol. 98, no. 19, p. 190504, May 2007.

[97] C. M. Dawson, H. L. Haselgrove, and M. A. Nielsen, "Noise thresholds for optical cluster-state quantum computation," *Phys. Rev. A*, vol. 73, no. 5, p. 052306, 2006.

[98] A. Ekert and R. Jozsa, "Quantum computation and shor's factoring algorithm," *Rev. Mod. Phys.*, vol. 68, no. 3, pp. 733–753, Jul 1996.

[99] T. Kleinjung, K. Aoki, J. Franke, A. Lenstra, E. Thom, J. Bos, P. Gaudry, A. Kruppa, P. Montgomery, D. A. Osvik, H. te Riele, A. Timofeev, and P. Zimmermann, "Factorization of a 768-bit rsa modulus," Cryptology ePrint Archive, Report 2010/006, 2010.

[100] R. L. Rivest, A. Shamir, and L. M. Adleman, 1983.

[101] P. W. Shor, "Polynomial-time algorithms for prime factorization and discrete logarithms on a quantum computer," *SIAM J. Comput.*, vol. 26, no. 5, pp. 1484–1509, 1997.

[102] D. Beckman, A. N. Chari, S. Devabhaktuni, and J. Preskill, "Efficient networks for quantum factoring," *Phys. Rev. A*, vol. 54, no. 2, pp. 1034–1063, Aug 1996.

[103] L. M. K. Vandersypen, M. Steffen, G. Breyta, C. S. Yannoni, M. H. Sherwood, and I. L. Chuang, "Experimental realization of shor's quantum factoring algorithm using nuclear magnetic resonance," *Nature*, vol. 414, pp. 883–887, 2001.

[104] S. L. Braunstein, C. M. Caves, R. Jozsa, N. Linden, S. Popescu, and R. Schack, "Separability of very noisy mixed states and implications for nmr quantum computing," *Phys. Rev. Lett.*, vol. 83, no. 5, pp. 1054–1057, Aug 1999.

[105] C.-Y. Lu, D. E. Browne, T. Yang, and J. W. Pan, "Demonstration of a cimpiled version of shor's quantum factoring algorithm using photonic qubits," *Phys. Rev. Lett*, vol. 99, p. 250504, 2007.

[106] B. P. Lanyon, T. J. Weinhold, N. K. Langford, M. Barbieri, D. F. V. James, A. Gilchrist, and A. G. White, "Experimental demonstration of a compiled version of shor's algorithm with quantum entanglement," *Phys. Rev. Lett.*, vol. 99, p. 250505, 2007.

[107] J. L. O'Brien, A. Furusawa, and J. Vuckovic, "Photonic quantum technologies," *Nature Photonics*, vol. 3, no. 12, pp. 687–695, DEC 2009.

[108] T. F. Krauss and R. M. D. L. Rue, "Photonic crystals in the optical regime – past, present and future," *Progress in Quantum Electronics*, vol. 23, no. 2, pp. 51 – 96, 1999.

[109] S. Noda, M. Fujita, and T. Asano, "Spontaneous-emission control by photonic crystals and nanocavities," *Nature Photonics*, vol. 1, no. 8, pp. 449–458, AUG 2007.

[110] B. J. Smith, D. Kundys, N. Thomas-Peter, P. G. R. Smith, and I. A. Walmsley, "Phase-controlled integrated photonic quantum circuits," *Opt. Express*, vol. 17, no. 16, pp. 13 516–13 525, 2009.

[111] E. Wooten, K. Kissa, A. Yi-Yan, E. Murphy, D. Lafaw, P. Hallemeier, D. Maack, D. Attanasio, D. Fritz, G. McBrien, and D. Bossi, "A review of lithium niobate modulators for fiber-optic communications systems," *Selected Topics in Quantum Electronics, IEEE Journal of*, vol. 6, no. 1, pp. 69–82, 2000.

[112] N. Walker and G. Walker, "Polarization control for coherent communications," *Lightwave Technology, Journal of*, vol. 8, no. 3, pp. 438 –458, Mar. 1990.

[113] S. Tanzilli, W. Tittel, H. De Riedmatten, H. Zbinden, P. Baldi, M. De Micheli, D. Ostrowsky, and N. Gisin, "PPLN waveguide for quantum communication," *European Physical Journal D*, vol. 18, no. 2, pp. 155–160, FEB 2002.

[114] Q. A. Turchette, C. J. Hood, W. Lange, H. Mabuchi, and H. J. Kimble, "Measurement of conditional phase shifts for quantum logic," *Phys. Rev. Lett.*, vol. 75, pp. 4710–4713, 1995.

[115] S. J. Devitt, A. D. Greentree, R. Ionicioiu, J. L. O'Brien, W. J. Munro, and L. C. L. Hollenberg, "Photonic module: An on-demand resource for photonic entanglement," *Physical Review A (Atomic, Molecular, and Optical Physics)*, vol. 76, no. 5, p. 052312, 2007.

[116] P. Michler, A. Kiraz, C. Becher, W. V. Schoenfeld, P. M. Petroff, L. Zhang,

E. Hu, and A. Imamoglu, "A Quantum Dot Single-Photon Turnstile Device," *Science*, vol. 290, no. 5500, pp. 2282–2285, 2000.

[117] C. Kurtsiefer, Mayer, Sonja, Zarda, Patrick, Weinfurter, and Harald, "Stable solid-state source of single photons," *Phys. Rev. Lett.*, vol. 85, no. 2, pp. 290–293, Jul 2000.

[118] K. Tsujino, M. Akiba, and M. Sasaki, "Ultralow-noise readout circuit with an avalanche photodiode: toward a photon-number-resolving detector," *Appl. Opt.*, vol. 46, no. 7, pp. 1009–1014, 2007.

[119] A. Divochiy, F. Marsili, D. Bitauld, A. Gaggero, R. Leoni, F. Mattioli, A. Korneev, V. Seleznev, N. Kaurova, O. Minaeva, G. Gol'tsman, K. G. Lagoudakis, M. Benkhaoul, F. Levy, and A. Fiore, "Superconducting nanowire photon-number-resolving detector at telecommunication wavelengths," *Nature Photon.*, vol. 2, no. 5, pp. 302–306, 2008.